Title
Tuning 2D materials for photonics, electronics and fluidics

Author
Xia, Yang

Publication Date
2019

Peer reviewed|Thesis/dissertation

Tuning 2D materials for photonics, electronics and fluidics

By

Yang Xia

A dissertation submitted in partial satisfaction of the
requirements for the degree of
Doctor of Philosophy
in
Applied Science and Technology
in the
Graduate Division
of the
University of California, Berkeley

Committee in charge:

Prof. Xiang Zhang, Chair
Prof. Ming C. Wu
Prof. Jie Yao
Prof. Chris Dames

Summer 2019

Tuning 2D materials for photonics, electronics and fluidics

Abstract

Tuning 2D materials for photonics, electronics and fluidics

by

Yang Xia

Doctor of Philosophy in Applied Science & Technology

University of California, Berkeley

Professor Xiang Zhang, Chair

Tunable properties are essential for a broad range of applications. In photonics systems, modulation of medium and light source plays a fundamental role for transmitting and processing information. For electronics industry, the manipulation of electron spin and magnetization leads to spintronics, currently a major driving force for high density data storage. And the gated ion transport is a critical component for the neuron systems. Often, it is much easier to manipulate a surface than a volume. Thus, two dimensional (2D) materials and systems, such as monolayer or few-layer crystals of van der Waals (vdW) materials and epitaxial-grown quantum wells, are intrinsically advantageous in pursuing tunability. This dissertation presents my work in engineering the tunable optic, electric, magnetic and mechanic properties of 2D materials and systems for various applications.

The first part of the dissertation presents our progress in building high performance optical modulators based on the broadband optical absorption of graphene tunable by carrier density. We achieved a record-high operation speed of 35 GHz with novel optoelectronic design enabled by amorphous silicon waveguide. The device performance is further boosted by a graphene-centered modulator structure. The waveguide mode features a large overlap with graphene corresponding to an absorption coefficient ~ 0.4 dB/μm from numerical simulation. Experimentally, we achieved a modulation depth of ~ 5 dB in a 30 μm – long device, which is more than twice increased from the previous designs. Our result brings new possibilities for the realization of compact ultrafast wide-band optical modulators. While the carrier density changes the light matter interaction through the Pauli exclusion principle, an external electric field directly modify the electronic levels through Stark effect. In the next part of the dissertation, I report a giant Stark shift of more than 30 meV on the single photons emitted from color centers in hexagonal boron nitride, a vdW layered wide bandgap insulator. We achieved well-shaped nanoscale electrode precisely aligned to the color centers, which allows unprecedented in-plane electric field on the order of 0.1 V/nm to be applied to the single photon emitter, critical for the observation of the giant shift. Furthermore, by controlling the orientation of the electric field, we observed an angle-resolved Stark effect, which shines light on broken inversion symmetry in the color center emitter. The giant room temperature Stark shift and the crucial information on the structural symmetry of the color center may represent an important step towards scalable room-temperature quantum communication and computation system based on vdW materials and their heterostructures. To manipulate the topological property of band structure, magnetic field can be introduced to modify the Hamiltonian of the system. The third part of the dissertation describes a high-frequency kink magnetoplasmons (KMPs) resonating

along a topological edge in a 2D electron gas (2DEG) hosted in an AlGaAs/GaAs heterojunction. A magnetic field with a flip of the orientation was applied to a 2DEG to generate a spatial change in the topology of band structure. The experimentally measured field- and electron-concentration-dependent resonant frequency perfectly matches theoretical prediction, which indicates strong potential of using magnetic domain boundaries to develop reconfigurable integrated topological circuits. In the fourth part of the dissertation, I describe the realization of such a magnetic domain boundary in a vdW layered ferromagnetic metal Fe_2GeTe_3 using its thickness dependent magnetic coercivity. From magneto-transport measurement, we discovered an antisymmetric magnetoresistance and kink Hall resistance as the evidence of the formation of magnetic domain boundary. The theoretical calculation based on our experimental measurement unveiled a perturbation current circulating around thickness step and mediating the electric potential change. Furthermore, such a circulating current is reverted at elevated temperature, which is consistent with the cross-over of magnetic coercivity on samples of different thicknesses. Those findings may lead to novel spintronics and topological electronics devices from vdW materials and their heterostructures. The last part of the dissertation extends the tunability of 2D materials into mechanics and presents the experimental study on tunable ion transport through the interlayer spacing in reduced graphene oxide (rGO) nanoflakes. With a gate voltage applied between the solution and the rGO flake, the ion permeation was considerably modulated, which can be explained by changes of the dehydration process and ion density inside the channel. Strikingly, we found an ultrafast ion diffusion at large gate voltages, with an effective diffusion coefficient orders higher than the value in bulk water. Our results demonstrate the interlayer spacing in rGO as an appealing platform for study the solid-ion and ion-ion interactions, as well as new material phase and chemical reaction in a tightly confined 2D space.

To my loving family

TABLE OF CONTENTS

TABLE OF CONTENTS ii
List of Figures iv
Acknowledgment vi
Chapter 1 Introduction 1
1.1. Tuning material properties 2
1.1.1. Tunability related to carrier-density 2
1.1.2. Stark effect: tuning by the electric field 5
1.1.3. Modifying 2DEG by magnetic field 5
1.1.4. Thickness dependent properties for quasi-2D materials 6
1.2. Major challenges in applying 2D materials 7
1.2.1. Volume mismatch 7
1.2.2. Surface passivation and protection 7
1.2.3. Growth and transfer 2D vdW materials 8
Chapter 2 Modulate light with tunable absorption in graphene 9
2.1. Background 9
2.2. Graphene modulator with amorphous silicon waveguide 12
2.2.1. Device structure 12
2.2.2. Numerical simulation 12
2.2.3. Device fabrication 13
2.2.4. Modulation measurement 15
2.3. Graphene-centered optical modulator 19
2.3.1. Device design 19
2.3.2. Numerical simulation 20
2.3.3. Device fabrication 22
2.3.4. Modulation measurement 24
2.4. Conclusion 25
Chapter 3 Control quantum emitter in a van der Waals insulator by Stark effect 26
3.1. Background 26
3.2. Device structure 27
3.3. Device fabrication 27
3.4. Giant Stark shift at room temperature 29

3.5. Angle-resolved Stark effect 30
3.6. Conclusion 33
Chapter 4 Manipulate electromagnetic response of 2D electron gas by magnetic field and electron concentration 34
4.1. Background 34
4.2. Device design 37
4.3. Chip design and fabrication 38
4.4. Experiment results 40
4.5. Conclusion 45
Chapter 5 Create and control magnetic domain wall in a few-layer van der Waals ferromagnetic metal 46
5.1. Background 46
5.2. Probing the orientation of magnetization by anomalous Hall effect 46
5.3. Device fabrication 47
5.4. Magneto transport measurement and results 49
5.5. Simulation using measurement results from uniform samples 52
5.6. Conclusion 56
Chapter 6 Control ion transport through sub-nanometer 2D channels 57
6.1. Background 57
6.2. Modulation principle 57
6.3. Device structure and fabrication 58
6.4. Ion transport measurement and results 60
6.5. Conclusion 64
Chapter 7 Summary and outlook 65
Bibliography 68

List of Figures

Figure 1.1| Interband transition modulated by Pauli blocking.. 3
Figure 1.2 | Electrostatically tuning carrier density using parallel capacitor structure. 4
Figure 2.1 | Principle of intensity modulator. 9
Figure 2.2 | Cross-section of amorphous silicon graphene optical modulator with waveguide-on-graphene structure 12
Figure 2.3 | Mode profile of the modulator region 13
Figure 2.4 | Fabrication of aSi graphene modulator. 14
Figure 2.5 | SEM image of the fabricated modulator device.. 15
Figure 2.6 | Optical setup for modulator measurement. 15
Figure 2.7 | Voltage controlled transmission in aSi graphene modulator. 16
Figure 2.8 | Wavelength-independent modulation depth. 17
Figure 2.9 | Schematic for RF measurement. 17
Figure 2.10 | RF response of the aSi graphene modulator 18
Figure 2.11 | RF response of the aSi graphene modulator under different temperatures.. 18
Figure 2.12 | Schematic of the graphene-centered optical modulator (cross section). 19
Figure 2.13 | Optimized mode profile and geometric structure of the graphene-centered optical modulator. 20
Figure 2.14 | Voltage dependent transmission for graphene-centered optical modulator. 21
Figure 2.15 | Layout of the graphene-centered modulator. 21
Figure 2.16 | Cross section SEM image of the stacked silicon waveguide. 22
Figure 2.17 | Fabrication procedure of the graphene-centered modulator. 23
Figure 2.18 | Microscope image of a fabricated graphene-centered modulator. 24
Figure 2.19 | Fiber-coupled modulator measurement setup. 24
Figure 2.20 | Voltage controlled transmission of graphene-centered modulator. 25
Figure 3.1 | Device to control the single photon energy of hBN color center SPE.. 27
Figure 3.2 | Fabrication of electrically tunable *h*BN single photon emitter. 28
Figure 3.3 | Room-temperature optical characterization of the SPE without voltage applied. 29
Figure 3.4 | Giant room-temperature Stark shift in *h*BN color center. 30
Figure 3.5 | Front panel of the LabView program to control the voltages on two electrodes according to specific field amplitude and direction. 31
Figure 3.6 | Angle-resolved Stark effect of *h*BN SPE and the discovered symmetry breaking. 32
Figure 4.1 | The dispersion and model profile of topological kink magnetoplasmons (KMPs). 36
Figure 4.2 | Realizing kink magnetoplasmons using patterned magnetic field. 38
Figure 4.3 | Chip design schematic. 39
Figure 4.4 | Fabrication steps for the electrical connection to the 2DEG chip. 40
Figure 4.5 | Quantum Hall effect in 2DEG sample. 41
Figure 4.6 | Magnetic-field-dependent microwave transmission spectra. 42
Figure 4.7 | Comparison between the experimental and theoretical magnetic-field-dependent edge mode frequency. 42
Figure 4.8 | Gate voltage-dependent microwave transmission spectra. 43

Figure 4.9 | Comparison between the experimental and theoretical electron-concentration-dependent mode frequency. 44
Figure 4.10 | Unidirectional character of the KMPs demonstrated by nonreciprocal microwave coupling..... 44
Figure 5.1 | Thickness-step-induced magnetic domain wall formation and its effect on transport properties..... 47
Figure 5.2 | Fabrication procedure for bottom-contact FGT device for Hall effect measurement. 48
Figure 5.3 | Device for domain wall manipulation 49
Figure 5.4 | Magnetotransport measurement configuration. 49
Figure 5.5 | Magneto-transport measurement result.. 50
Figure 5.6 | Magneto-transport measurement on a uniform sample with thickness of 8 nm.. 51
Figure 5.7 | Magneto-transport measurement on a uniform sample with thickness of 15 nm.52
Figure 5.8 | Calculated transverse voltage, magnetization orientation and perturbation current. 53
Figure 5.9 | Hall resistance and magneto resistance calculated from experimentally measured resistivities of uniform samples with similar thickness. 54
Figure 5.10 | Temperature dependence of the magneto resistance change. 55
Figure 5.11 | Temperature dependence of coercivities on the 8 nm and 15 nm uniform flakes. 56
Figure 6.1 | Schematic of the electrically tunable nanoscale 2D ion channel in reduced graphene oxide..... 58
Figure 6.2 | Fabrication procedure of the tunable ion channel device. 59
Figure 6.3 | Microscope images of a fabricated device..... 60
Figure 6.4 | Schematic of the ion transport measurement setup. 61
Figure 6.5 | Ion permeation at various gate voltages. 62
Figure 6.6 | Voltage dependent permeation rate. 62
Figure 6.7 | Repeatable voltage control of ion transport. 63
Figure 6.8 | Comparison of permeation rates of different ions at various voltages. 64

Acknowledgment

It's a great honor for me to have this opportunity to express my gratitude to my mentors, colleagues and friends who help me a lot during my study in UC Berkeley. Scientific research is challenging, but your advices, encouragement and support allow me to go through it.

First, I would like to thank Prof. Xiang Zhang for entrusting me in the research as well as his strong support and valuable guidance. From him I learnt the bravery to embrace challenges, persistence towards difficulties and being open-minded to novel and bold ideas. I appreciate his great leadership and effort to organize a group of researchers with such diverse backgrounds, which allows solving grand problems with inter-discipline expertise, as well as developing skills to communicate and collaborate with people in different fields. My sincere gratitude also goes to Prof. David Attwood, Prof. Ming Wu, Prof. Jie Yao and Prof. Chris Dames for serving in my prelim, qualifying and/or dissertation committees.

I thank Dr. Yuan Wang and Dr. Sui Yang for their mentorship and help throughout my PhD career. I appreciate the sound and kind advices from Dr. Yu Ye, Dr. Cheng Gong, Dr. Wei Bao, Dr. Xiaoze Liu and Dr. Hanyu Zhu. No less important are Dr. Hamed Dalir, Dr. Mervin Zhao, Dr. Dafei Jin, Mr. Quanwei Li, Mr. Siqi Wang and Dr. Yahui Xue, whom I closely worked with. I thank Dr. Ziliang Ye, Dr. Zi Jing Wong, Dr. Jeongmin Kim, Dr. Jun Xiao, Dr. Ying Wang, Dr. Haokun Li, Dr. Xuexin Ren, Dr. King Yan Fong, Dr. Shoufeng Lan, Mr. Renjie Tao, Mr. Zhaoyu Nie, Mr. Zhen Guo, Mr. Chengzhe Wang for the joyful time we spent together. I also appreciate the friendship and collaboration from all members and alumni of Prof. Zhang's group.

Finally, I would like to specially thank my parents and my wife who offer me endless love and unconditional support.

Chapter 1 Introduction

The dimensionality of a material has significant impact on its physical properties. Fundamentally, the dimensionality of the lattice structure determines the structure of equal-energy surface in momentum space and subsequently the density of energy state (DOS). Practically, the planar structure facilitates external manipulation. Thus, numerous material systems with two-dimensional (2D) structure has been explored, which have profoundly changed human life and society.

Traditionally, epitaxial growth with atomic precision has been used to achieve a 2D structure, quantum well, which is a major driven force in electronics and optoelectronics [1–3]. The 2D quantum confinement tunable by thickness reshapes DOS and enables manipulating effective mass and carrier distribution, which considerably improves the efficiency [4]. Combining with modulation doping, 2D electron gas (2DEG) with exceptional mobility can be realized, which is an essential part of the high electron mobility transistor (HEMT), widely used in high frequency devices [2,5].

In the past 15 years, van der Waals (vdW) layered materials have received considerable attention. The rapid progress started with graphene, a monolayer of carbon atoms arranged in a honey comb lattice. Such a monolayer was first isolated in 2004 and built into a transistor [6–8]. Since then, people have been excited by its outstanding properties, such as ultrahigh electron mobility [9–12], electrostatically tunable carrier density and Fermi level, impressive mechanical strength [13,14] and air stability. It has been used to demonstrate a broad range of applications, such as transparent electrode [15–18], radio frequency receiver [19–21], optical modulator [22–25], photodetector [26–29] and molecule sensor [30], etc. The exploration of its applications is further boosted by the rapid progress in graphene growth and transfer technology. Currently, wafer-scale graphene sheet is commercially available, and wafer-scale single crystal growth and transfer have also been reported [31].

The impressive success of graphene inspires the exploration on other 2D vdW materials. Hexagonal boron nitride (*h*BN) was subsequently exfoliated to monolayer and became popular as an atomic thin and flat insulator [9]. Comparing with conventional thin layer dielectric films, such as SiO_2 from thermal oxidation and Al_2O_3 by atomic layer deposition, hBN flakes enables dangling-bond-free interface, which is critical to the preserve the intrinsic high performance of monolayer and few-layer vdW metals and semiconductors [9,11].

Though the ultrahigh mobility of graphene is promising for high frequency operation, its gapless nature place severe limitation for logic devices and light emitters. To solve this problem, transition metal dichalcogenide (TMDC) [32,33] and black phosphorene (BP) [34,35] have been investigated for their sizable bandgap. Those materials also feature considerable change of physical properties when the thickness is reduced. For example, MoS_2 shows an indirect bandgap from bulk to 2 layers. But when it is exfoliated to monolayer, a direct bandgap appears with drastically increased photoluminescence (PL) intensity [36]. And the bandgap of BP is tunable from 0.3 eV (bulk) to 2 eV (monolayer) [34,37].

The reduced dimensionality also opens new opportunity for spintronics. While the Mermin-Wagner theorem predicts the strong suppression of long-range magnetic order in 2D systems, the

magnetic anisotropy and surface effect introduce energy barriers for the rotation of the magnetizations. Consequently, several 2D vdW magnets have been discovered, including $CrGeTe_3$ [38], CrI_3 [39] and Fe_2GeTe_3 [40–42]. The magnetic-field-induced anisotropy, antiferromagnetic interlayer coupling, and carrier-density dependent magnetism discovered in those materials may enable novel device designs and functionalities.

1.1. Tuning material properties

1.1.1. Tunability related to carrier-density

The free electrons and holes carry charge and heat in solid and have strong interaction through both Pauli repulsion and electrostatic force. Thus, the density of free electron and holes (carrier density) has profound effect on the material properties. As charge carriers, the electrical conductivity of solid is directly determined by the charge carrier density as

$$\sigma = e\mu N \tag{1}$$

where e, μ and N are the absolute value of electron charge, mobility and carrier density, respectively. Furthermore, in materials where electron (and/or holes) are the major heat carriers, as indicated by the Wiedemann–Franz law, the thermal conductivity is also proportional to the carrier density

$$\kappa = LT\sigma = LTe\mu N \tag{2}$$

Thus, tuning the carrier density can effectively change those two transport properties.

From the optical perspective, electron/hole density plays an important role through the intraband and interband transitions. The intraband transition can be well approximated by Drude model in noble metals and doped semiconductors for certain range of frequency. It predicts a dielectric function [43]

$$\varepsilon(\omega) = \varepsilon_\infty - \frac{Ne^2}{\varepsilon_0 m\omega^2} \tag{3}$$

In this formula, ε_∞ corresponds to the permittivity at infinite high frequency (usually set to 1). m is the (effective) mass of electron, which usually take some effective value due to band structure. The Drude model is widely used in nanophotonics based on plasmonic effect.

To account for the interband transition, the Fermi's golden rule predicts the net transition rate from the initial state i to final state f as

$$R = \frac{2}{V}\sum_{k_i}\sum_{k_f}\frac{2\pi}{\hbar}\left|H'_{fi}\right|^2 \delta\left(E_f - E_i - \hbar\omega\right)\left(f_i - f_f\right) \tag{4}$$

The occupation probabilities for the initial state f_i and final state f_f obeys Fermi distribution, which is parameterized by the Fermi level E_F (or quasi Fermi levels E_{FC} and E_{FV} for the electrons and holes, respectively, under pumping condition). On the other hand, the Fermi level and carrier density are linked through the DOS ρ_e

$$N = \frac{2}{V}\int f(E)\rho_e dE \tag{5}$$

Thus, by controlling the carrier density, the Fermi level can be shifted, which may affect light absorption and emission. When the Fermi level is below all the initial states or above all the final states participating a specific optical transition, the optical absorption will be suppressed, which is called as Pauli blocking and can be used to build electroabsorption modulators.

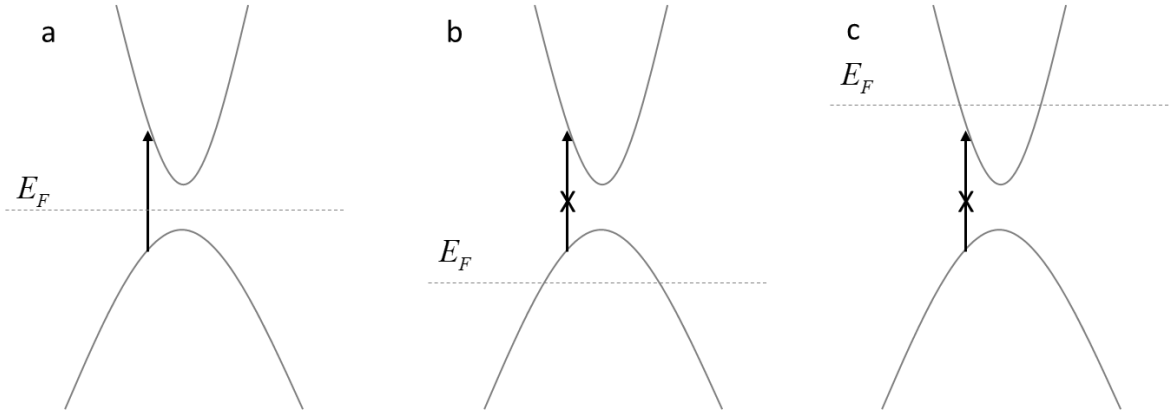

Figure 1.1| Interband transition modulated by Pauli blocking. An optical transition connecting a ground state in the valence band and an excited state in the conduction band is indicated by the vertical arrow. (a) The Fermi level is between the ground state and the excited state, corresponding to an occupied ground state and an un-occupied excited state. Thus, the optical transition is allowed, and the material is absorptive. (b) (and (c)) The Fermi level is below (above) the ground (excited) state, corresponding to an empty (occupied) ground (excited) state. In such cases, the optical transition is not allowed between those two states, and the material show low absorption for such photon energy.

In addition, through the interaction with crystal bond and lattice, the carrier density enables tuning of another wide range of material properties. It can modify the electron-photon scattering, which enables using Raman spectroscopy as a nondestructive yet effective way to probe the doping level in materials [44–47]. It can be used to control various phase transition phenomena, such as the formation of charge density wave [48,49], superconducting state [50], ferromagnetic domains [38–40,42] and lattice change [51]. As the phase transitions usually come with drastic change in physical properties, it is expected that wide range of applications could be developed through those mechanisms.

The carrier density is usually manipulated by either electrostatic gating and/or ionization of dopants. The former enables faster dynamic control but can only change the carrier density near the surface and the induced carrier density change is limited by the breakdown of gate dielectric material. The latter, on the contrary, can change the carrier density for a wide range in bulk volume, yet is only done during material growth or by diffusion and slow. For practical applications, those two methods are usually used together if possible.

The electrostatic gating has been the central mechanism for the operation of field effect transistor (FET). Following Gauss's law, the carriers induced on a charged parallel plate capacitor is characterized by a surface density:

$$\rho_{free}^{2D} = \frac{\varepsilon_0 \varepsilon_r E}{e} \tag{6}$$

where ε_0, ε_r, E and e are the permittivity of vacuum, relative permittivity of the dielectric material, the electric field in it and the absolute value of electron charge. A large carrier density can be induced by using a dielectric material with higher ε_r and increase the applied electric field, which is ultimately limited by the dielectric material. For example, in SiO_2, ε_r = 3.9 and the breakdown voltage for a ~300 nm thickness is ~ 100 V, the maximum carrier density is ~ 7×10^{12} cm^{-2}. Other common dielectric materials also show similar performance. To achieve even larger carrier density by electrostatic gating, ionic liquid can be used. In that case, the gate voltage is effectively applied to an electronic double layer (EDL) on the surface of the conductor which features a nanoscale thickness and can sustain ultrahigh electric field on the order of 10 MV cm^{-1}, resulting a giant carrier density on the order of 10^{14} cm^{-2}, critical for manipulating optical response of graphene in visible range and phase transitions [52].

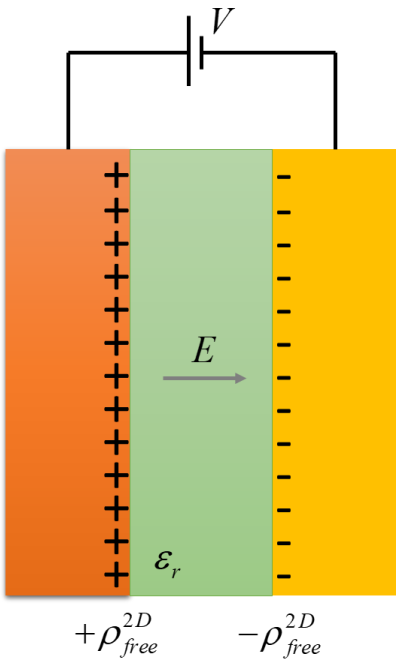

Figure 1.2 | Electrostatically tuning carrier density using parallel capacitor structure. A voltage is applied across a capacitor structure. It introduces an electric field across the dielectric material and generate surface charges on the conductors near the interface to the dielectric material.

The free carrier density is also affected by dopants and their electronic structure. To form PN junctions in silicon, boron, phosphorus and arsenic are commonly used dopants. And the carriers in the HEMT 2DEG come from ionization of silicon doped in the AlGaAs layer. Various dopants have been studied for 2D vdW materials. The graphene can be doped by substitution carbon with other atoms such as nitrogen and oxygen [53]. Adsorption of molecules including NO_2, F4-TCNQ, $AuCl_3$ have also been used to control the carrier type and density in graphene and other 2D vdW materials [53,54]. And water and oxygen in air can also serve as unintentionally dopants by similar when adsorbed to the surface. Such doping process also introduces charged impurities and

compromises carrier mobility. Nevertheless, for applications where mobility is not a major concern, the chemical doping has been proved as a very efficient way to realize high conductivity [18].

1.1.2. Stark effect: tuning by the electric field

The Stark effect is the tuning of electronic energy levels by an external electric field [55]. It is observed in a wide range of systems, such as atom, molecule, color center, quantum dot, quantum well as well as bulk semiconductor. Generally, a uniform electric field modifies the original Hamiltonian H_0 to H as

$$\begin{aligned} H &= H_0 + V' \\ V' &= e\mathbf{F}\cdot\mathbf{r} \end{aligned} \tag{7}$$

where e, F and r are the electron charge (absolute value), applied field and position. Following the time-independent perturbation theory in quantum mechanics, the energy shift of each state $|n\rangle$ can be calculated as

$$\begin{aligned} \Delta_n &\equiv E_n - E_n^{(0)} = V'_{nn} + \sum_{k\neq n} \frac{\left|V_{nk}\right|^2}{E_n^{(0)} - E_k^{(0)}} + \cdots \\ V'_{nk} &\equiv \left\langle n^{(0)} \middle| V' \middle| k^{(0)} \right\rangle \end{aligned} \tag{8}$$

for non-degenerated unperturbed states $\{|n\rangle\}$. Similar result is obtained for degenerate states with if choosing the eigenstates that can diagonalize V' and excluding the degenerated states from the summation for the second order [55]. Practically, it is convenient to introduce the permanent electric dipole moment $\boldsymbol{\mu}$ and polarizability tensor $\boldsymbol{\alpha}$, corresponding to the linear and quadratic terms from (8), to describe the electron wavefunction distribution and its distortion due to the applied field. For molecule and color center, they provide good length and volume estimation. The energy shift can then be written as

$$\Delta E_n = -\boldsymbol{\mu}\cdot\mathbf{F} - \frac{1}{2}\mathbf{F}\cdot\boldsymbol{\alpha}\cdot\mathbf{F} \tag{9}$$

Besides energy shift, the applied electric field may also change the absorption and emission by modifying the wavefunction and coupling strength of electronic states and bands [1]. Such electrical tuning has been applied to the generation of indistinguishable photons and electroabsorption modulators.

1.1.3. Modifying 2DEG by magnetic field

Moving electrons experience Lorentzian force from magnetic field

$$f = -e\mathbf{v}\times\mathbf{B} \tag{10}$$

where **v** and **B** are the electron velocity and magnetic field, respectively. The electron movement corresponds to electric current density. Consider a 2DEG system confined in x-y plane, with a time-invariant magnetic field applied in z direction, the electric current **j** and carrier density variation ρ follow the frequency-domain governing equation below [56]

$$
\begin{aligned}
-\mathrm{i}\omega\rho(\mathbf{r},\omega) &= -\nabla_r \cdot \mathbf{j}(\mathbf{r},\omega) \\
-\mathrm{i}\omega\mathbf{j} &= \alpha(\mathbf{r})\mathbf{E}(\mathbf{r},\omega) - \omega_c(\mathbf{r})\,\mathbf{j}\times\mathbf{e_z}
\end{aligned}
\tag{11}
$$

where α and ω_c describes the 2D local longitudinal conductivity and cyclotron frequency due to the magnetic field

$$
\begin{aligned}
\alpha(\mathbf{r}) &= -\mathrm{i}\omega\sigma(\mathbf{r},\omega) \\
\omega_c(\mathbf{r}) &= \frac{eB_0(\mathbf{r})}{m_* c}
\end{aligned}
\tag{12}
$$

E is the electric field at the z = 0 plane and in the nonretarded limit is determined by the current density **j** as [56]

$$
\begin{pmatrix} E_x(\mathbf{q},\omega) \\ E_y(\mathbf{q},\omega) \end{pmatrix} = \frac{2\pi}{i\omega q\xi(q)} \begin{pmatrix} q_x^2 & q_x q_y \\ q_x q_y & {q_y}^2 \end{pmatrix} \begin{pmatrix} j_x(\mathbf{q},\omega) \\ j_y(\mathbf{q},\omega) \end{pmatrix}
\tag{13}
$$

Without magnetic field, a gap-less dispersion is obtained [56]

$$
\begin{aligned}
\omega_p(q) &= \sqrt{\frac{2\pi\alpha q}{\xi(q)}} \xrightarrow{q\to 0} v_p q \\
v_p &= \sqrt{\frac{4\pi\alpha}{\epsilon_{eff}}}
\end{aligned}
\tag{14}
$$

where ξ and ε_{eff} are a q-dependent screening function and the effective permittivity at the 2DEG location, respectively.

The magnetic field results in a band opening in dispersion [56]

$$
\omega_{\pm}(q) = \pm\sqrt{\omega_c^2 + \omega_p^2(q)}
\tag{15}
$$

For a system with an edge next to vacuum, a one-way edge mode forms with dispersion at long wavelength limit [56]

$$
\omega_{edge}^{(1)}(q_y) = v_p q_y, \qquad (q_y \geq 0).
\tag{16}
$$

Moreover, even when the 2DEG has a uniform electron density throughout the whole space, an edge separating two regions with magnetic fields of opposite signs also support a one-way propagating mode with similar dispersion (first topological edge state). In addition, a second mode appears with frequency close to ω_p. Despite a negative wavevector, the group velocity is positive, which proves it is also one-way mode with the same direction as the first topological state [56].

1.1.4. Thickness dependent properties for quasi-2D materials

While a monolayer of vdW 2D materials exhibits many attractive properties drastically different from their bulk counterpart, the transition during the thickness reduction also provides an effective tuning knob. Although the interlayer atoms don't form chemical bond, their electronic

and magnetic coupling is not negligible, which serves as a major tuning mechanism. One striking example is the indirect-to-direct bandgap transition in MoS_2 [36]. The conduction band minimum and valence band maximum of bulk MoS_2 is between K and Γ points in momentum space, resulting in an indirect band gap with low luminescence emission efficiency. As the thickness reduces, such an indirect bandgap increases, faster than the gap at K point, due to smaller effective mass. Finally, at monolayer, the energy gap at K point becomes new band gap, which enables high emission efficiency and is critical for lighting applications. In addition, black phosphor also shows similar tuning effect, which features a tunable bandgap from 0.35 eV in bulk to 1.73 eV at monolayer [37].

Strong thickness dependence also exhibits in the 2D vdW magnets. The Curie temperature in $CrGeTe_3$, for example, increases with thickness, due to the significant contribution of interlayer coupling in establishing the ferromagnetic order [38]. Such interlayer coupling reduces the DOS per spin for the magnon modes near the excitation gap, thus a higher temperature is required for a thicker sample to excite enough population of excitations to suppress the long-range magnetic order. Similar trend is also observed in Fe_2GeTe_3(FGT), which however, features a soft-to-hard magnetism transition as thickness decreases below 200 nm [40]. Interestingly, as discovered in CrI_3, the interlayer coupling can be antiferromagnetic, which results in drastically different magnetizing behavior of bilayer sample comparing with monolayer and tri-layer [39].

1.2. Major challenges in applying 2D materials

While appealing properties have been found in 2D material systems, significant challenges need to be overcome before their practical applications.

1.2.1. Volume mismatch

One major challenge for optical application is the large volume mismatch with respect to the optical wavelength. For light to be effectively absorbed or emission, a good confinement factor and long enough propagation distance are needed, which is not readily available for 2D material due to the atomic thickness. Even though graphene has an impressive 2.3% absorption per layer for normal incidence, making it among the darkest materials, such absorption is far from practical requirement (modulation depth > 50% considering power efficiency and signal to noise ratio). Multiple layers can stack together, yet since modulation only happen at the first few layers next to the capacitor dielectric, such approach is not applicable to dynamic applications. Similar problem also occurs for lighting applications using the 2D semiconductors such as TMDCs. Despite the appealingly strong light matter interaction in the monolayer limit, their coupling with cavity is weak, making it difficult to build lasers from them.

1.2.2. Surface passivation and protection

Due to the ultrathin nature, the impurities on the surface effectively couple to the whole depth of the material, drastically modifies the carrier transport (impurity scattering), optical response (Fermi level shift) and magnetic coercivity (domain wall pinning). Those impurities may come from contamination, such as dangling bond of near-by dielectric materials and adsorption of atoms and molecules, as well as surface damage during fabrication process, such as reaction with oxygen, organic solution and radicals in lithography, deposition and etching processes. Thus, the protection of surface is a major consideration during the design and manufacturing of devices based on 2D materials, which is usually achieved by appropriate choice of a passivation layer.

*h*BN is an excellent candidate to maintain the intrinsic properties of the materials it clads [9]. It is free of dangling bonds and able to sustain high electric field (on the order of 0.1 V/nm). Furthermore, it features a self-clean mechanism of contaminations at the vdW interface. In graphene, it enables the observation of room temperature mobility up to 140,000 cm^2/Vs and low-temperature ballistic transport over distances beyond 15 micrometers [11]. It is also used to protect BP, CrI_3 and FGT from degradation in air. Besides, atomic layer deposition is widely used in nanofabrication due to its capability to deposit ultrathin dielectric films with high quality (low leaking current and high breakdown electric field). Especially for gate dielectric deposition, it has been intensively investigated for a better scalability [57]. Yet the surface condition becomes very complex due to the interaction between the graphene, dangling bond of dielectric material and (most likely) a seeding/functionalization layer (to overcome the hydrophilicity of graphene).

1.2.3. Growth and transfer 2D vdW materials

The growth of 2D materials requires high temperature/pressure and are generally not compatible with other components on the device substrate. Consequently, appropriate transfer techniques are required for device fabrication. Multiple transfer methods have been developed for different applications, depending on the required scalability, alignment precision and cleanliness. For chip and wafer scale fabrication, wet transfer is widely adopted, especially for CVD graphene on Cu foil, which is commercially available in wafer scale. But that method can't be applied to substrate with water sensitive component. Although various dry transfer methods for CVD graphene grown on Cu foil have been reported, they are still difficult to repeat with high yield. On the other hand, dry transfer of 2D vdW flakes exfoliated on SiO_2 substrate is the choice when precise alignment and oxygen and water free process is needed. The best practice is using polymer to pick up a *h*BN flake, then use the *h*BN flake to pick up other materials, layer-by-layer if necessary, then land the full stack onto a target substrate or prepatterned electrode with a *h*BN under cladding if possible. Apparently, such a procedure prevents the material from contacting any solvent and could be conducted in glove box where oxygen and water is also avoided. Yet that cleanness comes with a cost of complexity and poor scalability.

Towards large scale transfer high quality material, several important milestones have been achieved. The wafer scale single-crystal graphene grown on Ge substrate was reported in 2014, including a wafer scale dry transfer taking the advantage of weak bonding between the graphene and the substrate [31]. The obtained mobility ~7,000 cm^2/Vs is comparable to the metal-catalyzed single-domain graphene at that time. One year later, mobilities > 300,000 cm^2/Vs at 1.6 K and > 50,000 cm^2/Vs at room temperature are obtained from CVD single crystal graphene grown on Cu foil and transferred by *h*BN pickup method [58]. Those progress makes the application of graphene in industrial level promising.

Chapter 2 Modulate light with tunable absorption in graphene

2.1. Background

The rapid development of Internet, the popularity and easy accessibility of high definition images and videos, as well as the rise of big data technologies result in the fast growth of data traffic. Optical modulator is a key device for high speed optical communication. While directly modulating the light source, which is usually a laser diode (LD), involves complex electron-hole dynamics and undesired chirp [1], using an external modulator generally provides better stability and faster operation speed. Without the limitation on the light generation efficiency, the wider choices of materials and easier design enables closer integration with other electronics systems. Thus, the innovation and development on the optical modulators have been a key approach to improve the network bandwidth to enable the continuous growth of data traffic.

An optical modulator is a device that transfers the data from electric signal to optical signal. It requires a continuous wave (CW) light beam and a time-varying electronic signal as input. Its optical transmission varies according to the electric signal. As a result, the output light beam becomes loaded with the information previously conveyed by the electric signal. Such information can be encoded to the intensity or (and) phase of light. Figure 2.1 shows a schematic for an intensity modulator.

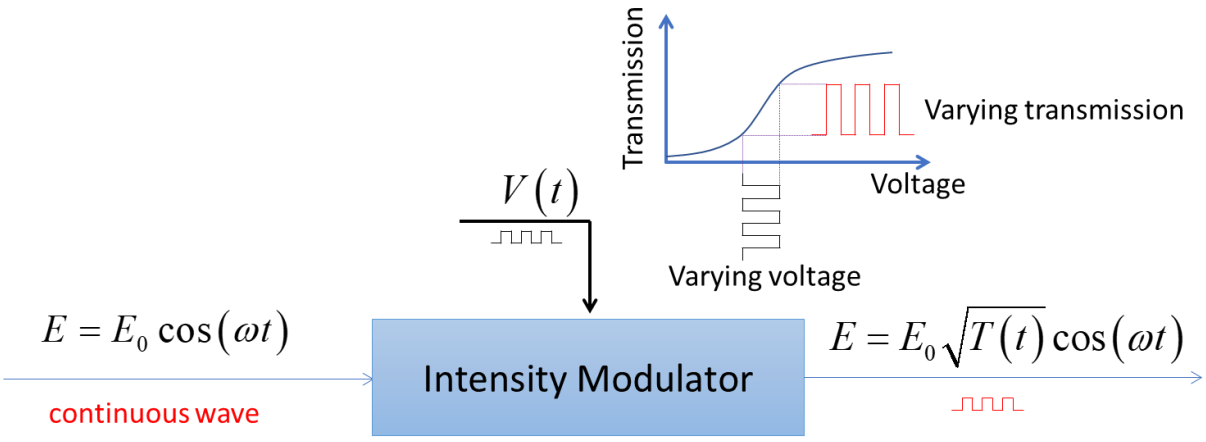

Figure 2.1 | Principle of intensity modulator. The modulator has optical transmission as a function of voltage. With a continuous wave (CW) light input, the output light beam will follow the voltage signal according to the voltage-dependent transmission.

The change of transmission is implemented by modifying the (complex) refractive index of the propagating channel. In the case of electro-refractive modulator, the real part of refractive index is modified, resulted in a phase change of the light beam. In materials with inversion symmetry breaking, the second order nonlinearity can be exploited to generate real refractive index change

by applying electric field, known as the Pockels effect, as in the widely-used $LiNbO_3$ modulator, which, however, is expensive due to the high material cost. Silicon features mature fabrication technology and low material cost and its refractive index can be tuned using free carrier dispersion (Drude model) thus has been intensively studied for optical modulation [59–62]. But the weak tuning results in large insertion loss for non-resonant device and undesired temperature sensitivity for resonant ones.

Another approach is changing the imaginary part of refractive index, or the absorption. Traditionally, Franz–Keldysh effect and quantum confined Stark effect (QCSE) have been utilized in bulk and quantum well semiconductors [63–65]. The applied electric field enables absorption of photons with energy smaller than the original bandgap due to the modulation of wavefunctions and excitonic effect. Alternatively, Pauli blocking principle, in which the occupation of ground and excited states is modified by carrier injection. But both methods limited to wavelength near bandgap in traditional material systems.

Graphene is a monolayer of carbon atoms arranged in a honeycomb lattice. Its ultrahigh electron mobility is promising for high speed operation. Near the Fermi level the band structure features a gapless linear dispersion, which results in wideband absorption [66,67]

$$E(q) = \pm \hbar v_F |q| \tag{17}$$

where the Fermi velocity $v_F \approx 1\times10^6$ m/s and q is distance from K or K' point in k-space at the Fermi level. The plus minus sign accounts for two bands. Considering the 2D density of state, the Fermi level E_F (away from charge neutral point) is determined by the carrier density N as [68]

$$E_F = \pm \hbar v_F \sqrt{\pi |N|} \tag{18}$$

As shown in Chapter 1, with parallel capacitor structure, the Fermi level can be tuned by a voltage

$$E_F = \pm \hbar v_F \sqrt{\pi \frac{\varepsilon_0 \varepsilon_r}{te} |V - V_0|} \tag{19}$$

On the other hand, the absorption of graphene can be characterized by its optical conductivity σ comprising of the contributions from intraband transition σ_{intra} and interband transition σ_{inter}

$$\sigma = \sigma_{intra} + \sigma_{inter} \tag{20}$$

From Kubo formula, those contributions can be calculated as [69–74]

$$\begin{aligned}
\sigma_{intra}(\omega,\tau,E_F,T) &= \frac{ie^2}{\pi\hbar^2(\omega + i\tau^{-1})}\int_0^\infty \left(\frac{\partial f(E-E_F)}{\partial E} - \frac{\partial f(-E-E_F)}{\partial E}\right) E dE \\
&= \frac{i4\sigma_0}{\pi\hbar(\omega + i\tau^{-1})} 2k_B T \ln\left(2\cosh\left(\frac{E_F}{2k_B T}\right)\right) \\
&= \frac{i4\sigma_0 |E_F|}{\pi\hbar(\omega + i\tau^{-1})} \qquad (|E_F| \gg k_B T)
\end{aligned} \tag{21}$$

and

$$\sigma_{inter}\left(\omega,\Gamma,E_F,T\right)=\frac{ie^2\omega}{\pi}\int_0^\infty\frac{f\left(-E-E_F\right)-f\left(E-E_F\right)}{\left(\hbar\omega+i\tau^{-1}\right)^2-\left(2E\right)^2}dE$$

$$=\sigma_0\frac{i4\hbar\omega}{\pi}\int_0^\infty\frac{f\left(-E-E_F\right)-f\left(E-E_F\right)}{\left(\hbar\omega+i\tau^{-1}\right)^2-\left(2E\right)^2}dE \tag{22}$$

$$\approx\sigma_0\left\{1+\frac{1}{\pi}\left[\tan^{-1}\left(\frac{\hbar\omega-2\left|E_f\right|}{\Gamma}\right)-\tan^{-1}\left(\frac{\hbar\omega+2\left|E_f\right|}{\Gamma}\right)\right]-\frac{i}{2\pi}\log\left(\frac{\left(\hbar\omega+2\left|E_f\right|\right)^2+\Gamma^2}{\left(\hbar\omega-2\left|E_f\right|\right)^2+\Gamma^2}\right)\right\}$$

Here an 2D conductivity

$$\sigma_0=\frac{e^2}{4\hbar}=6.09\times10^{-5}\ \text{S} \tag{23}$$

is introduced, which only contains natural constants and corresponds to the universal absorption in undoped graphene. ω, E_F and are the optical frequency and graphene Fermi level (reference to the undoped value). τ, Γ denote the scattering time, and interband transition broadening factor. To obtain the dispersion $\tau \sim 40$ fs [71] is widely used. While the integral form in (22) contains both temperature and relaxation broadening [69], there are multiple approximations but the difference is not significant for practical modeling, if the broadening factor is appropriately chosen. For the interband transition, the major broadening is from temperature ~ $4k_BT$, thus the approximation with $\Gamma \sim 110$ meV in (22) or [75] gives similar result.

For electromagnetic field simulation, the conductivity contributes to the in-plane component of the anisotropic relative complex permittivity as

$$\varepsilon_{\|}=\varepsilon_\infty+\frac{i\sigma}{\varepsilon_0\omega t_g} \tag{24}$$

where $\varepsilon_\infty = 2.5$ based on the dielectric constant of graphite. The thickness of graphene $t_g = 0.5$ nm can be used [72]. The corresponding refractive index can be calculated as

$$n_{\|}=\sqrt{\frac{\left|\varepsilon_{\|}\right|+\mathrm{Re}\left\{\varepsilon_{\|}\right\}}{2}}+\mathrm{i}\sqrt{\frac{\left|\varepsilon_{\|}\right|-\mathrm{Re}\left\{\varepsilon_{\|}\right\}}{2}} \tag{25}$$

Here positive real and imaginary part of the refractive index is assumed to reflect the lossy nature of graphene. For the out-of-plane direction, the permittivity and refractive index for graphite can be directly applied.

This chapter presents our work in developing high performance optical modulator by integrating graphene with amorphous silicon (aSi) waveguide. Most of the content has been presented in a previous publication [76].

2.2. Graphene modulator with amorphous silicon waveguide

2.2.1. Device structure

To improve the quality of graphene transfer and facilitate the high-speed and broadband operation, a planar structure is developed placing the waveguide above the graphene structure (Figure 2.2). The hydrogenated amorphous silicon (aSi) exhibits low loss with refractive index close to the crystalline silicon [77,78], which is ideal to fabricate highly confined waveguide on top of the graphene double layer structure. Moreover, such structure provides better flexibility in tuning the gate dielectric thickness to achieve high speed or low voltage operation, depends on the application requirement.

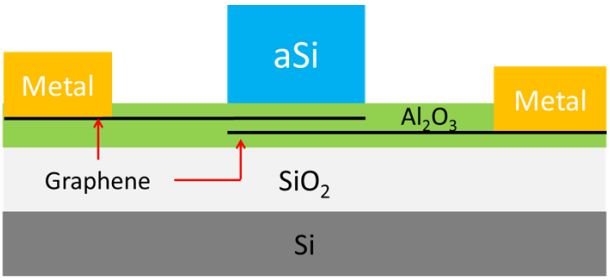

Figure 2.2 | Cross-section of amorphous silicon graphene optical modulator with waveguide-on-graphene structure.

2.2.2. Numerical simulation

For numerical simulation, the graphene is modeled as an effective medium with anisotropic dielectric constant by (20) - (25). With a two-dimensional finite element method (FEM) simulation carried out using COMSOL Multiphysics, the effective refractive index n_{eff} of each propagation mode can be obtained, which can be converted to mode loss as [1]

$$\alpha = \frac{4\pi}{\lambda} \operatorname{Im}\{n_{eff}\}. \tag{26}$$

The calculation results indicate that the absorption of the TM mode (0.1 dB/μm) is greater than the transverse electric (TE) mode due to its better overlap with graphene. Thus, a 3-dB absorption could be achieved with only 30 μm modulator length.

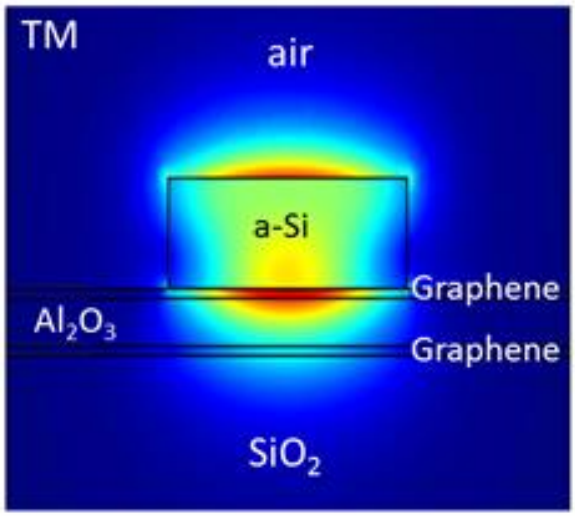

Figure 2.3 | Mode profile of the modulator region

2.2.3. Device fabrication

To fabricate the double-layer graphene optical modulator, wet thermal oxidation and atomic layer deposition (ALD) are used to realize a 1 μm silica and a 20 nm thick Al_2O_3, respectively, which form the under cladding for the waveguide mode. Next, chip-sized graphene grown on copper was transferred to the goal substrate with the wet transfer method [79]. Electrode and a contact pad for the bottom graphene layer were defined by E-beam and UV lithography, respectively followed by E-beam evaporation of Cr/Pd/Au with a thickness of 2/10/90 nm. A rapid thermal annealing process can be used to improve the contact. The pattern on graphene is defined by E-beam lithography with PMMA as resist and etched with oxygen plasma.

It is noted that a pristine graphene with the hydrophobic nature of the basal plane encounters the difficulty in the at direct deposition of high dielectric constant material through the ALD method. Therefore, a seeding layer of 2 nm-thick of Al_2O_3, is deposited onto the bottom graphene by E-beam evaporation [80]. The planar design of graphene layers lets us form an interlayer of 120 nm-thick Al_2O_3 with ALD for ultra-fast optoelectrical uses. The top graphene layer is then transferred, forming a capacitor structure. Similar procedures as the bottom graphene layer are performed to allow the active tuning of graphene layers. A layer of 270 nm thick-amorphous silicon (a-Si) is deposited by PECVD at 150 °C. Eventually a silicon waveguide with width of 400 - 600 nm, with both ends connected to a pair of grating couplers (period = 870 nm, optimized for transverse magnetic (TM) mode with λ =1550 nm) is fabricated via E-beam lithography and transformer coupled plasma (TCP) etching. The major fabrication steps are shown in Figure 2.4.

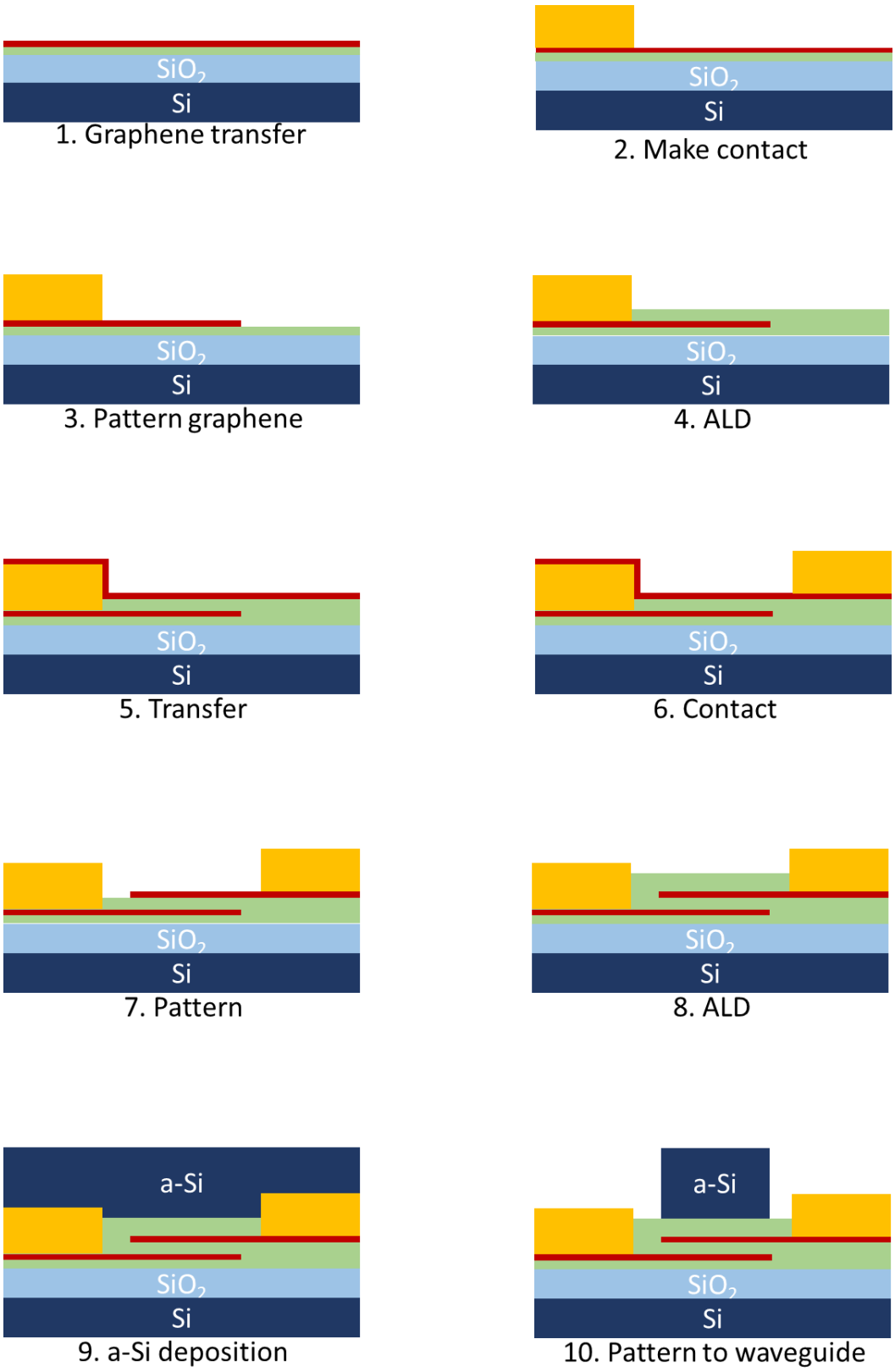

Figure 2.4 | Fabrication of aSi graphene modulator.

The fabricated device is characterized with scanning electron microscopy (SEM) as shown in Figure 2.5.

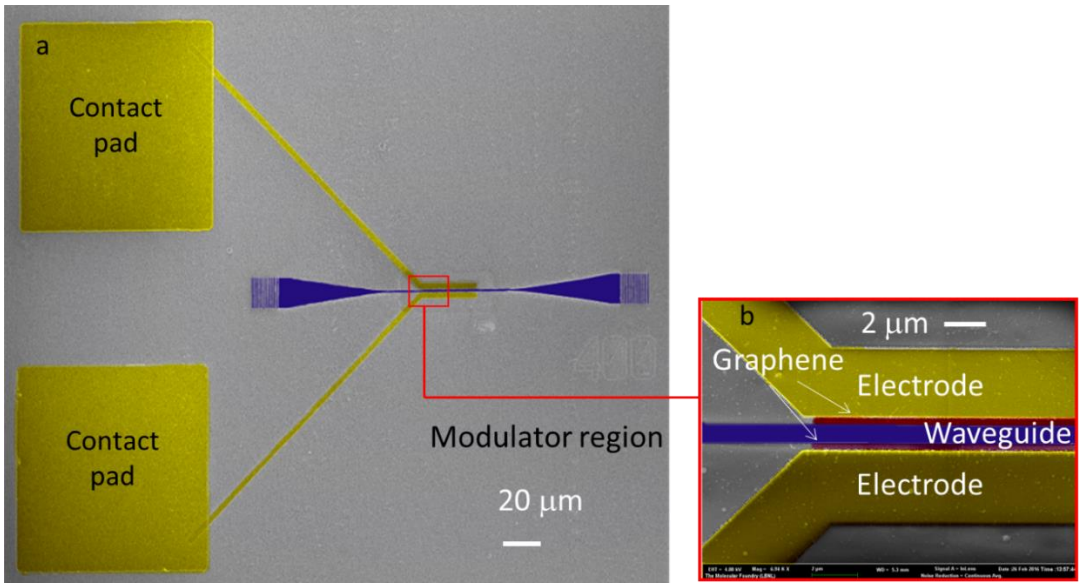

Figure 2.5 | SEM image of the fabricated modulator device. Top and bottom graphene layers (red colors) overlap well with the modulator waveguide.

2.2.4. Modulation measurement

Both DC and RF measurement are conducted for the fabricated modulator. The light from a laser diode is coupled into the modulator using free space optics. To control the angle and position, a 4f system is constructed so that the position and angle of the light beam incident on the objective is manipulated by the angle and position of the mirror in front of the 4f system. The output light is collected by the same objective and coupled into a mode fiber connected to a photoreceiver.

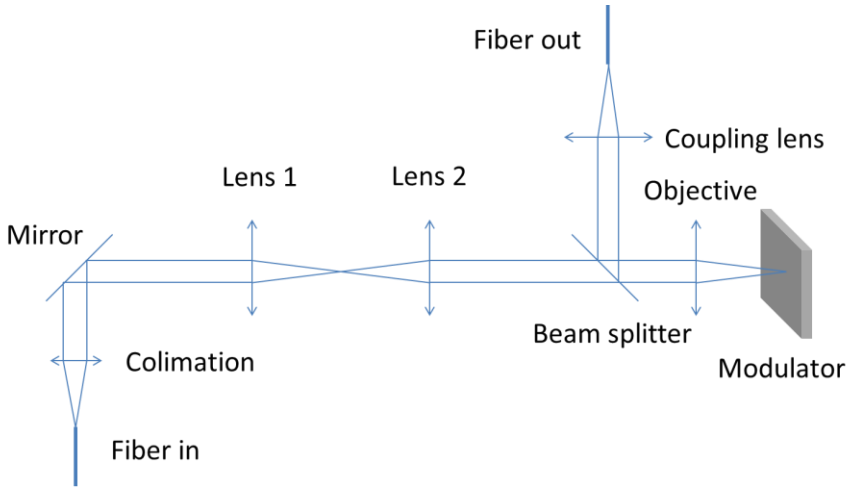

Figure 2.6 | Optical setup for modulator measurement.

To characterize the static behavior of the modulator, a DC voltage is applied to the modulator while the output light power is monitored. A modulation ~ 1.8 dB is obtained by changing voltage as shown in Figure 2.7. The insertion loss due to grating coupler ~ 13.5 dB has been subtracted. In our device, when positive voltage is applied to the top layer (bottom layer is effectively negatively biased), less positive voltage is needed to suppress the absorption comparing with negative voltage case. This is because the absorption is mainly from the top layer graphene which is closer to the waveguide mode and that layer is initially p-doped.

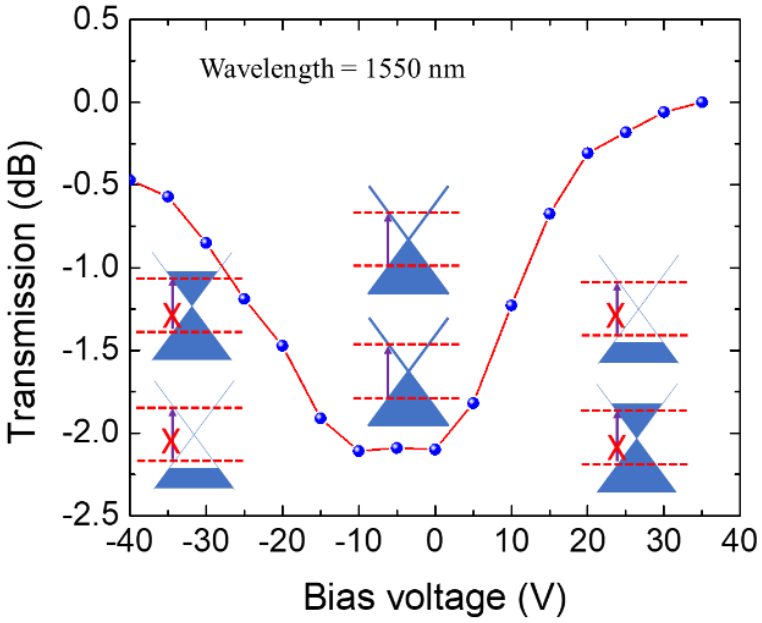

Figure 2.7 | Voltage controlled transmission in aSi graphene modulator.

One major advantage of graphene modulator is the broadband optical band operation, i.e. the modulator can work with wide range of wavelength. We examined the optical bandwidth of our double-layer graphene device in a large range of optical communication wavelengths. A uniform modulation depth under different optical wavelengths (1500~1640 nm) is observed with a constant swing voltage (Figure 2.8). Such a broadband functionality makes it a promising candidate for high-capacity optical short-reach interconnect technologies.

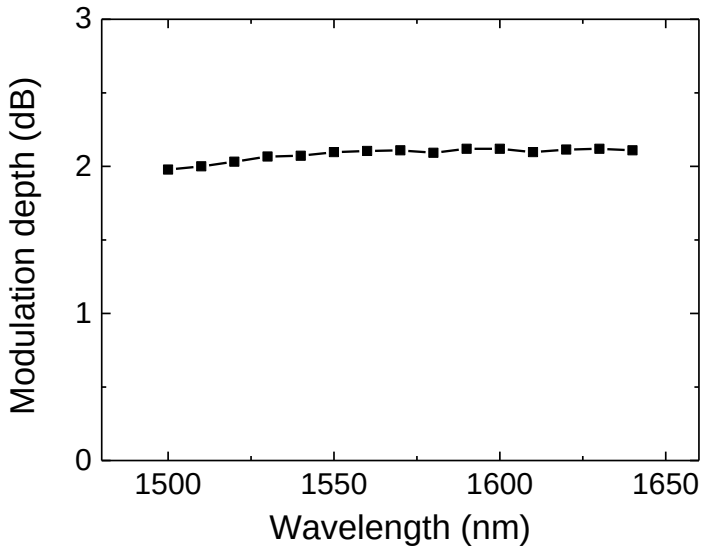

Figure 2.8 | Wavelength-independent modulation depth.

Next, we characterize the high-speed operation of the aSi graphene modulator by RF measurement. RF signal with -7 dBm power is generated from a calibrated Anritsu 37397D vector network analyzer (VNA) and combined with a bias DC voltage of 25 V through a SHF BT-110 bias-tee. The combined signal is applied between the bottom and top layers of graphene via a GGB model 40A-GS microwave probe. Losses from the cabling, bias-tee and probe are subtracted. For the RF measurement, a BPDV3120R u^{2}t photodiode cascaded with a UA1L65VM broadband post-amplifier is used to convert the modulated optical signal back to RF signal to be analyzed with the VNA.

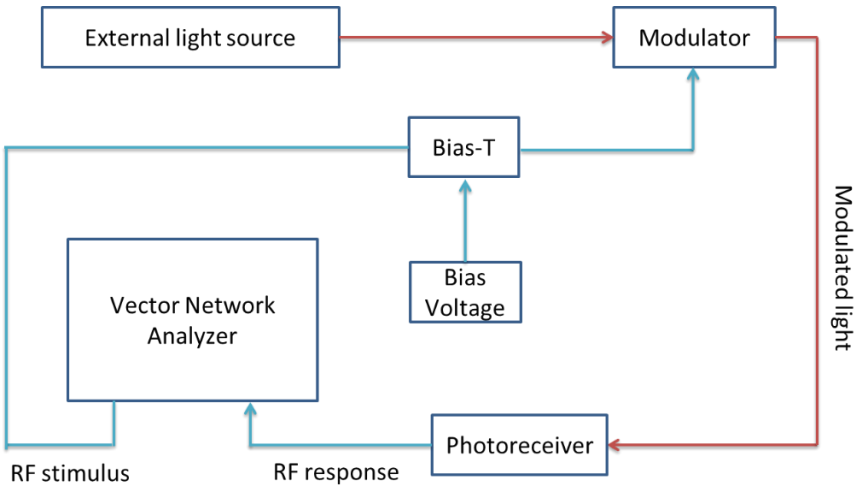

Figure 2.9 | Schematic for RF measurement. Only major components are shown in the figure.

We measured small-signal radiofrequency (RF) (S_{21}: ratio between the optical amplitude modulation and the RF signal). Figure 2.10 illustrates the S_{21} results, while a bandwidth of 35 GHz limited by the RC time constant of our fabricated modulator is obtained. The RC is restricted by

the dimension of the capacitor, graphene sheet resistance and contact resistance. An estimation of the measured device's geometric capacitance is 9 fF, while our measurement revealed that the high series resistance (~500 Ω) mainly comes from the contact resistance between the graphene layer and palladium electrode, which is the key issue for the current speed limitation. Using the state-of-the-art process, the series resistance of the device can be considerably reduced to below 50 Ohm [25,81] can significantly increase the speed of the modulator.

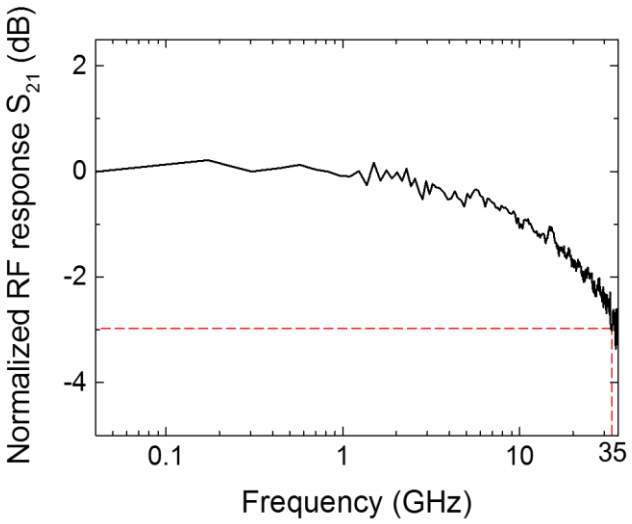

Figure 2.10 | RF response of the aSi graphene modulator

We further demonstrate a temperature-insensitive operation. We measure the RF response (S_{21}) at 1550 nm at different temperatures. As shown in Figure 2.11, the normalized RF response shows negligible change as temperature rises. In addition, a 1.9 dB modulation depth at an elevated temperature with the same swing voltage is obtained. The robust athermal operation in modulators is critical to optical interconnection and communication systems for ultra-fast efficient modulation.

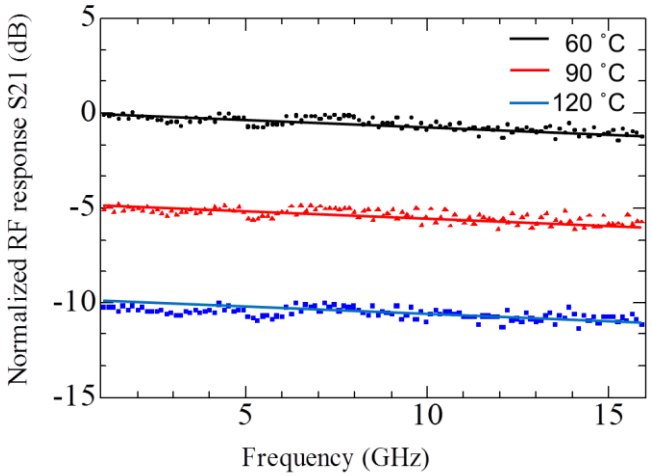

Figure 2.11 | RF response of the aSi graphene modulator under different temperatures. The obtained S_{21} is shifted with step of 5 dB for better comparison among different temperatures. The slope is virtually constant while the temperature raises from 60 to 120 ˚C.

2.3. Graphene-centered optical modulator

The modulation depth per unit length is an important specification for the design of modulator. Given a required modulation depth, it determines the length of the modulator. On the other hand, the energy per bit W and RC-bandwidth are determined by the length of the modulator as

$$W = \frac{1}{4} C_g V_{pp}^2 L$$
$$f_{RC} = \frac{1}{2\pi C_g \left(R_0 L + R_g \right)} \tag{27}$$

Here C_g and R_g is the capacitance and resistance per unit length of the modulator. V_{pp} is the peak-to-peak driving voltage and R_0 is the source impedance (50 Ω and 25 Ω for unterminated and terminated case, respectively). As a result, it is highly desired to increase modulation depth per unit length in order to reduce the energy consumption, increase operation speed and minimize the footprint.

2.3.1. Device design

In the previous design, the graphene sheets are not overlapped with the center of the waveguide mode, which weakens their coupling to the light field. As a result, mode loss from the graphene sheets is limited to ~ 0.1 dB/μm. To boost the performance of the modulator, we theoretically design and experimentally investigate the graphene-centered optical modulator. The cross section is shown in Figure 2.12. Instead of placing the waveguide on top of the graphene capacitor, we split the waveguide into two halves and insert the graphene capacitor structure between them. Because the gap between the two silicon strips is small, their optical modes could couple together, resulted in a strong light field propagating along the graphene capacitor. Considerable modulation depth enhancement is observed from numerical simulation and experimentally fabricated devices.

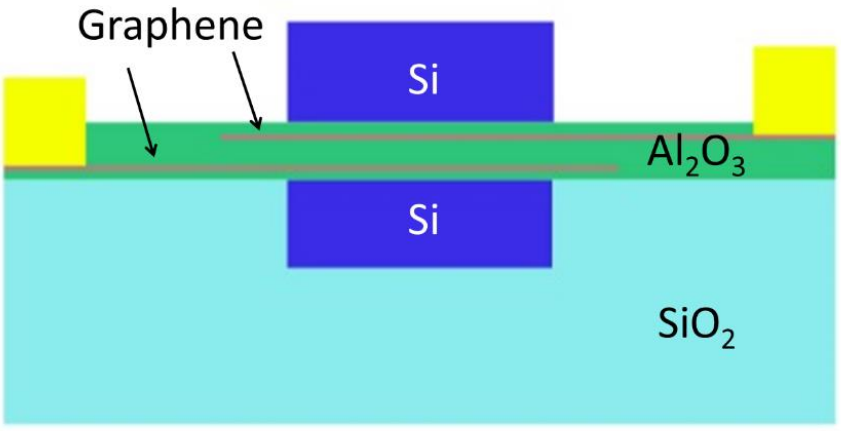

Figure 2.12 | Schematic of the graphene-centered optical modulator (cross section).

2.3.2. Numerical simulation

Using COMOSL, we calculate the mode profile and effective refractive index n_{eff} corresponding to undoped graphene. Generally, a smaller cross section area of the silicon strips gives a larger imaginary part of n_{eff}, to which the modulation depth per unit length is proportional. That is because as the silicon cross section area decreases, a larger portion of light field is squeezed out of the silicon, which may increase its overlap with graphene. However, the real part of n_{eff} also decreases due to the same reason. To ensure a confined mode, the real part of n_{eff} should be larger than $n_{SiO2} = 1.45$ (for 1550 nm wavelength).

We find a practically reasonable optimized structure shown in Figure 2.13. The width of silicon strips is 400 nm. The thickness of the bottom and top silicon strip is 80 and 100 nm, respectively. We choose an Al_2O_3 thickness of 70 nm and a distance of 60 nm between the graphene sheets so that high speed operation is possible based on the experimental values for the graphene contact and sheet resistances. The graphene overlap region is set at 600 nm to modulate the light field slightly spreaded out from the silicon region. It also helps to improve the tolerance on the misalignment during the fabrication process. The calculation indicates $n_{eff} = 1.8027+0.0107i$, corresponding to a mode loss ~ 0.4 dB/μm.

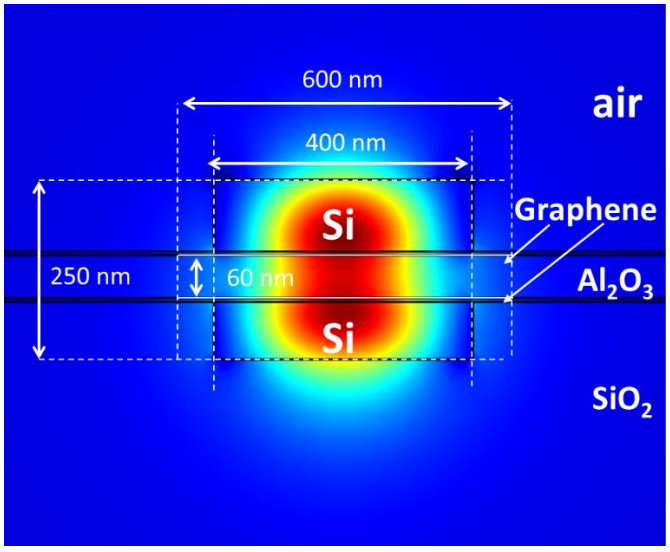

Figure 2.13 | Optimized mode profile and geometric structure of the graphene-centered optical modulator.

The voltage dependent transmission is calculated by incorporating the voltage-dependent optical conductivity of graphene (Figure 2.14). We assume the at zero bias voltage, the Fermi levels of both graphene sheets are at the charge neutral point, thus the same optical conductivity are assigned to them for each voltage. Considering the low frequency permittivity of ALD Al_2O_3 $\varepsilon_{ox} = 6.8$ [25,82,83], modulation depth of 6 dB is obtained for a 30 μm-long modulator with only 7.5 V, with a RC-limited bandwidth > 70 GHz, great for high speed applications.

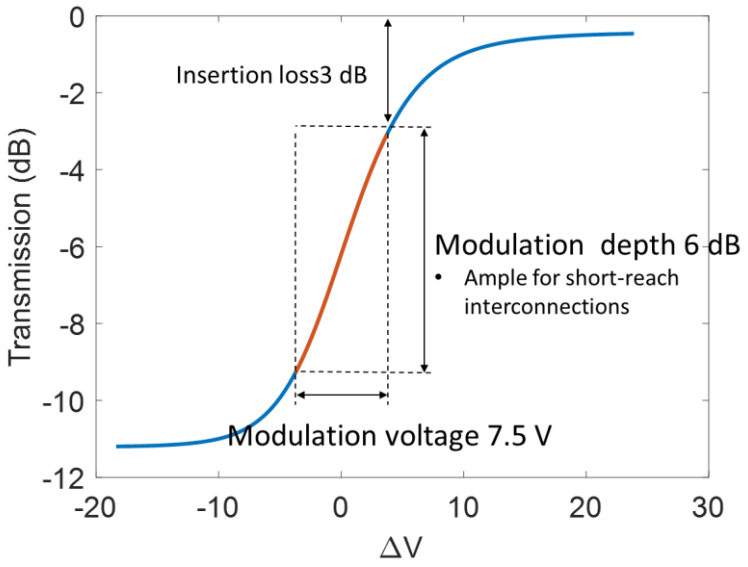

Figure 2.14 | Voltage dependent transmission for graphene-centered optical modulator.

The full the modulator device comprises the modulation region, contact pads, and grating couplers to couple the light in and out (Figure 2.15). We set the modulation region between the RF contact pad to minimize their distance and reduce the parasite effect on the electric connection. The center-to-center distance between the probe contact pads are assigned with the pitch of our RF probe. Two grating couplers are arranged with an offset to suppress their cross-talk due to scattering. We leave a large spacing between the grating couplers to incorporate optical fiber to approach them with the RF probe is contact with the device.

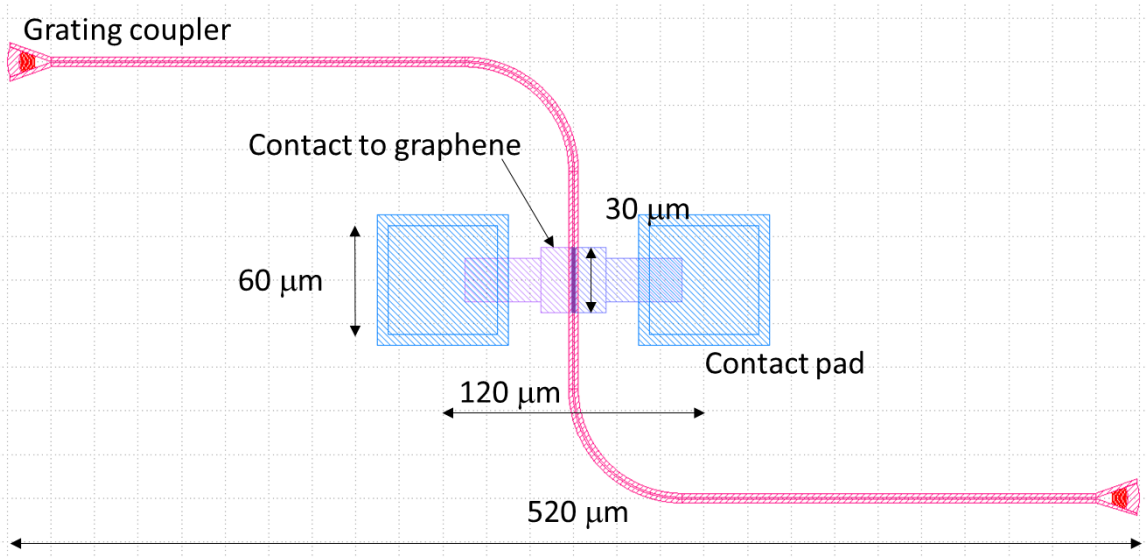

Figure 2.15 | Layout of the graphene-centered modulator.

2.3.3. Device fabrication

First, the bottom waveguide is fabricated by PECVD deposition, e-beam lithography and dry etch. The fabrication starts with a silicon wafer with 10 μm thermal SiO_2 on top, which provides good optical and electrical isolation from the substrate. To form the bottom layer waveguide, amorphous silicon is deposited by PECVD at 150 °C. The deposition rate is ~ 0.53 nm/s. Because the coupling efficiency of the grating coupler is sensitive to the thickness of the silicon, we carefully calibrate the deposition rate using a dummy sample before running the real substrate. To avoid the inhomogeneity due to edge effect for our chip size 15×15 mm^2, a special pocket holder is used, which matches the size and thickness of the chip and avoid any gap or thickness step along its edges. Afterwards we use e-beam lithography to define the bottom layer waveguide pattern. We choose PMMA as the resist for e-beam lithography for this project due to its easier removal unless otherwise stated. With the patterned PMMA as etch mask, we etch the silicon layer with a TCP etcher. The etched region is then filled with SiO_x by e-beam lithography [35]. Again, the deposition rate is calibrated by a dummy run on a silicon chip each time before running the real sample. Finally, the chip is liftoff in acetone with sonication, and rinse with IPA and water. A 5 nm-thick ALD Al_2O_3 is grown on the chip to fill gaps and smooth the surface for better graphene transfer yield.

Second, the bottom layer graphene is transferred, contacted, and patterned. CVD-grown graphene on Cu foil is wet transferred to the substrate. We use 0.1 M $(NH_4)_2S_2O_8$ aqueous solution to etch Cu at room temperature, which gives less metal residue contamination comparing with $FeCl_3$. Next, graphene contact comprising 20 nm Pd and 60 nm Au is fabricated using e-beam lithography, e-beam evaporation and liftoff. Afterwards, the graphene is pattern by e-beam lithography etched with oxygen plasma.

Third, we grow ALD Al_2O_3 as the gate dielectric layer. We deposit ~ 2nm Al by thermal evaporation at ~ 6×10^{-6} torr. Based on our experiment, such a seeding layer provides lower graphene resistance, possibly due to lower defect density. Then the Al_2O_3 is grown at 200 C using $Al(CH_3)_3$ and water as precursors. Afterwards we transfer, contact, and pattern the top layer graphene using similar procedures as the bottom layer. Then another ALD Al_2O_3 is deposited on the top graphene layer, serving as a protection layer for further process.

Afterwards, the top layer waveguide is fabricated with PECVD, e-beam lithography and dry etch. A cross section SEM without graphene structure is shown in Figure 2.16. A thin layer of Pd/Au is sputtered onto the fabricated sample

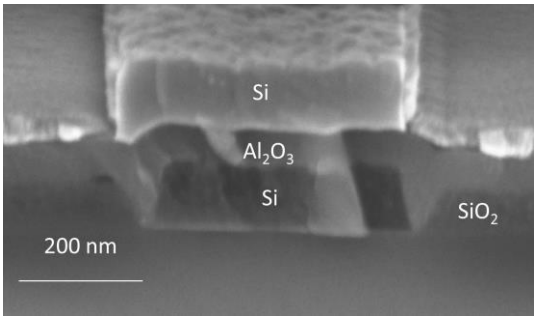

Figure 2.16 | Cross section SEM image of the stacked silicon waveguide.

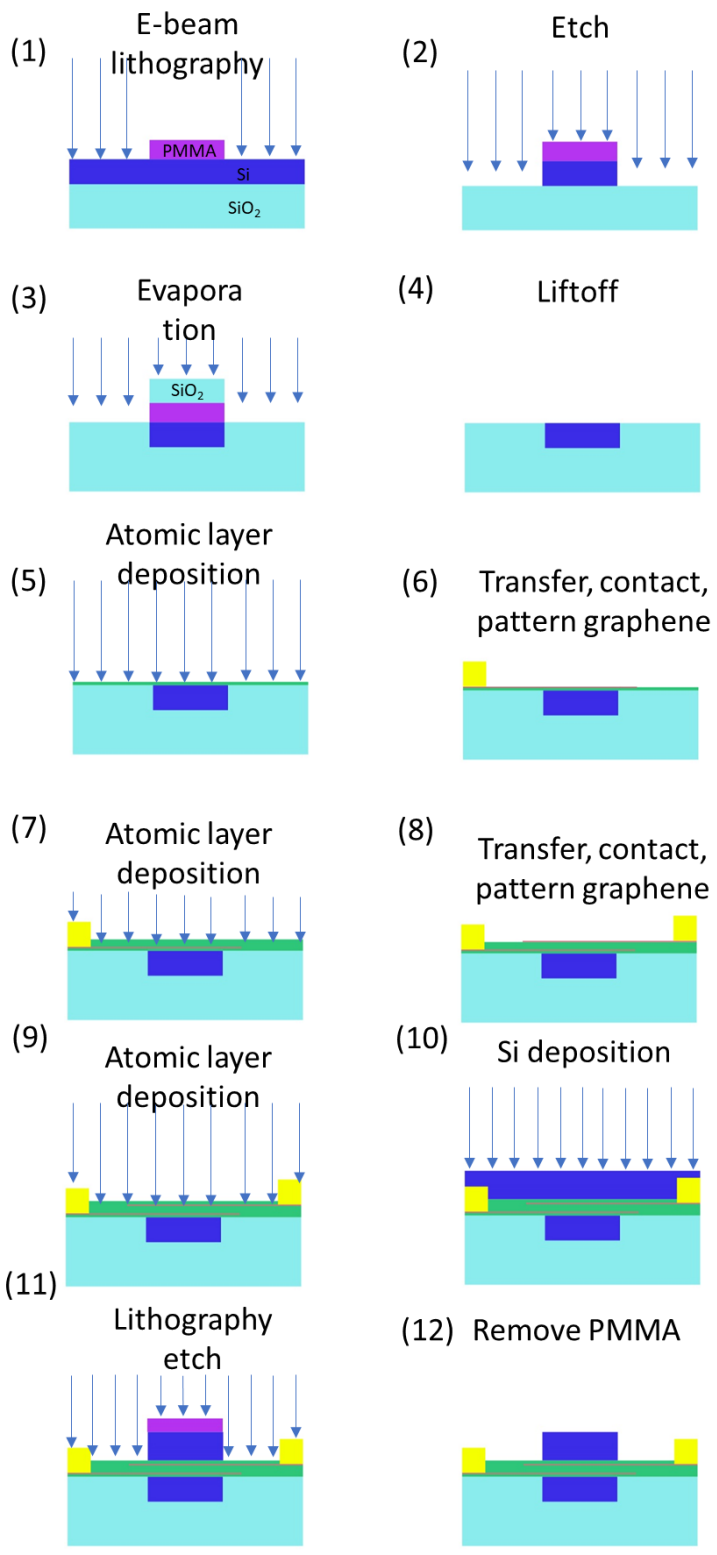

Figure 2.17 | Fabrication procedure of the graphene-centered modulator.

Finally, the probe contacts are fabricated. Since the graphene contact has been covered by the oxide and aSi layer, we need vias to access the contact electrodes, indicated by the larger blue square at the probe contact location in Figure 2.15. The pattern is defined by UV lithography, and the aSi and oxide layers are etched by reactive ion etch and diluted buffered hydrofluoric acid. At last, probe contact made of 5 nm Ti/ 200 nm Au is fabricated using UV lithography, e-beam evaporation and liftoff.

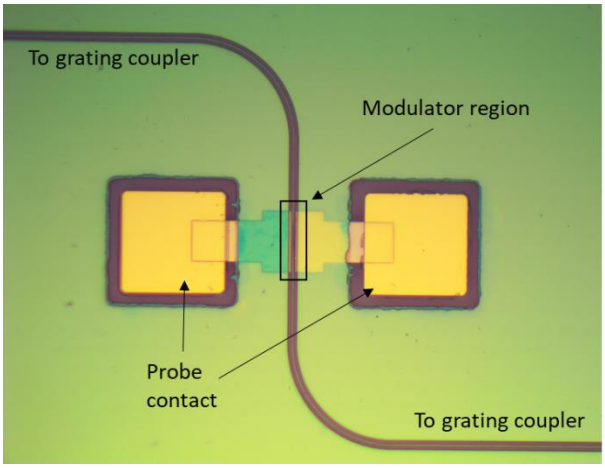

Figure 2.18 | Microscope image of a fabricated graphene-centered modulator.

2.3.4. Modulation measurement

We measure the static modulation response using a fiber-coupled measurement setup (Figure 2.19). Each single mode fiber is fixed on one aluminum beam, on which a 10-degree slot is cut to precisely set the angle of the fiber. The fibers and RF probe are mounted on 3D translational stages and aligned to the device under a home-built microscope. The device is placed on a 2D translational stage to facilitate changing the device under test.

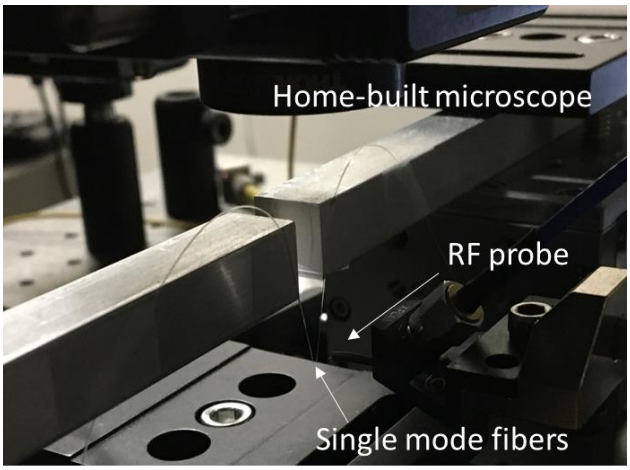

Figure 2.19 | Fiber-coupled modulator measurement setup.

We obtain voltage dependent transmitted optical power as shown in Figure 2.20. The incident light is generated from a fiber coupled DFB laser diode emitting at 1548.5 nm. The voltage is scanned from -20 V to + 20 V. The maximum modulation depth is 5 dB, which is more than twice comparing with the previous design. The discrepancy from the numerical estimation may due to undesired waveguide shape distortion and defects on graphene which suppresses the Fermi level modification, which could be improved by optimizing the fabrication parameters. The required modulation voltage is also decreased to ~ 14 V due to a thinner gate oxide layer. The asymmetric response might due to different defect types and densities on the bottom and top oxide-graphene interface.

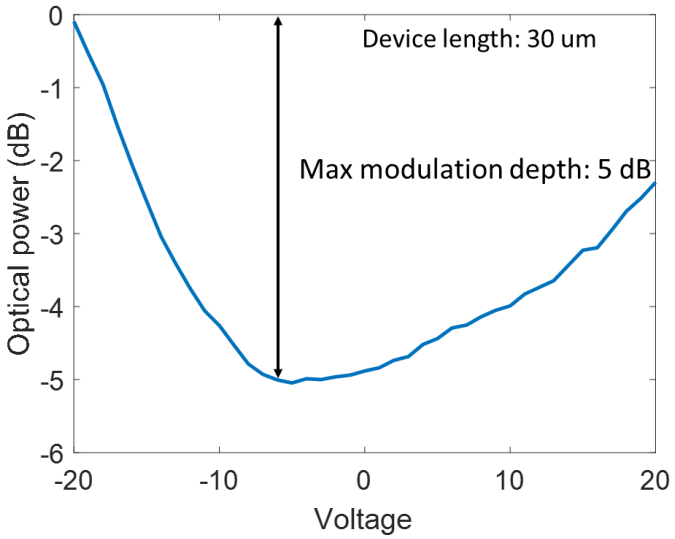

Figure 2.20 | Voltage controlled transmission of graphene-centered modulator.

2.4. Conclusion

We thoroughly study the design, fabrication and test of graphene-based optical modulator. We obtained an ultrafast operation up to 35 GHz in a planar double-layer graphene modulator. A uniform modulation depth of ~2 dB was demonstrated for the entire optical communication wavelengths (1500 − 1640 nm) with a miniature design of 30 μm length. With the graphene-centered modulator structure, a modulation depth of 5 dB was achieved with same device length, which could be further improved by optimizing the fabrication procedure.

With the clear understanding of the fundamentals of the graphene optical modulator, the next step is would be scalable fabrication of high-quality devices. Large scale transfer technologies should be incorporated to realized wafer-scale device fabrication. The defects introduced by resist residue and ALD deposition and their impact for the device performance should be systematically studied. The *h*BN is a promising dielectric material as a protection of graphene from the undesired damage and contamination during the fabrication, which is to be applied for scalable fabrication. And the implemented waveguide structure can be applied to integrate a wide range of 2D materials into planar photonic circuits.

Chapter 3 Control quantum emitter in a van der Waals insulator by Stark effect

Aside from the carrier density, 2D systems can also be manipulated by an electric field. While changing carrier density requires electric contact, fields can be applied across insulators, which provides better flexibility. This chapter presents the manipulation of single photon emitters (SPEs) in *h*BN with promising performance and features for various applications.

3.1. Background

Quantum information systems provide unprecedented computation capability and communication security [84]. In classical information systems, operations are generally in sequential. By multiplication of computation hardware, parallel computing is possible, but only linear with the amount of hardware. In contrary, by utilizing the quantum coherence and hybrid states, some NP problems, such as factorization, can be solved in polynomial time, which corresponds to an exponentially speed-up [85]. Moreover, a quantum state may change upon measurement. As a result, information-theoretic-security can be realized through encoding information into quantum carriers [86]. Due to the light-speed transmission and low-noise properties, photons are important quantum information carriers [87].

In order to be used in quantum information systems, streams of photons need to be generated with controllable quantum correlations, which can be achieved by single photon emitters [88]. Solid-state single photon emitters are promising for their scalability [87,89]. However, they also suffer from inhomogeneous broadening due to inhomogeneity of the solid-state environment. Such variation breaks the indistinguishability of single photons from multiple emitters and blocks the realization of large-scale quantum computation. The variation in emission wavelength also places great challenge for integration with photonic circuit, where resonant components are widely used to boost information capacity by wavelength division multiplex and enhance light matter interaction with multi-pass light path.

To resolve such a problem intrinsic to the nature of solid-state platform, various tuning methods have been adopted. Thermal tuning has been used to tune quantum dot (QD) SPEs into resonance with a microcavity to achieve strong coupling, based on the temperature-dependent bandgap, which results in a typical tuning rate of -0.04 meV/K [90]. Strain can also be used to tune SPEs, as is demonstrated in [91], where the emission spectrum of one QD SPE is tuned by a PZT crystal to overlap with another to realize the quantum interference.

Aside from the temperature and strain, electric field can also be used to tune the SPEs, through the Stark effect [55]. While it is generally challenging to independently address multiple emitters on one substrate in a scalable way, electric field can be tightly confined in electrodes, which can be readily integrated on the substrate hosting the SPEs. It has been used to tune the emission energy of quantum dots, single photon emitters in layered WSe_2, atomic emitters such as NV centers and SiV centers in diamond and organic dye molecules [92–99]. But large tuning range of single photons at room temperature is still challenging, due to the intrinsic limit of those SPEs.

Since discovered in 2016, color centers in *h*BN have received considerable attention due to its outstanding properties [100–107]. They are capable to work at room temperature, stably and

without significant phonon side band (PSB). They exhibit high internal quantum efficiency and among the brightest SPEs. The emitted photons are linearly polarized, facilitate the photonic design and application. From such a layered material, nanoscale structures can be achieved with high quality, which enables high-efficiency photon extraction. Even without additional photon extraction structures, millions of photons can be easily detected per second. Moreover, their facile integration with photonic and electrical components is highly preferred for integrated on-chip quantum information systems. For the future application of hBN SPEs in quantum information systems, controlling the single photon wavelength is critical. We address such a problem by using the Stark effect. The major result of this chapter will appear in a subsequent publication [108].

3.2. Device structure

We design a nano-scale four-electrode device to achieve large Stark shifts and a fully characterization of the dependence of the energy shift on the amplitude and orientation of the local electric fields (Figure 3.1). Given their much better optical performance compared to those in monolayers, we realize the device with SPEs in multi-layer *h*BN nano-flakes. In order to control not only the amplitude but also the direction of the electric field, we carefully design multiple electrodes to surround the SPEs. The gaps between the adjacent and diagonal electrodes are as small as 200 nm and 400 nm, respectively. Such a device can achieve unprecedented large electric field of ~ 0.1 V/nm, orders of magnitudes higher than previous reports.

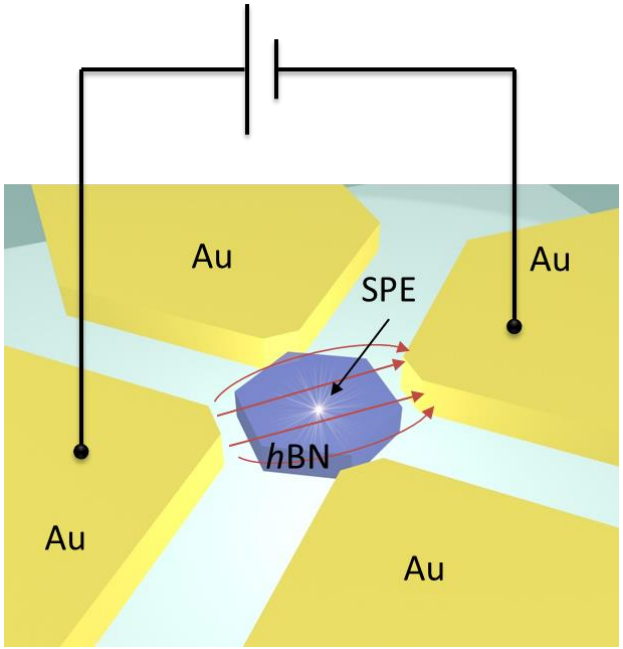

Figure 3.1 | Device to control the single photon energy of hBN color center SPE. The voltage can be applied to any combination of electrodes to control the direction and magnitude of the applied electric field.

3.3. Device fabrication

The hBN nanoflakes dispersed in ethanol/water solution are purchased from Graphene Supermarket and drop casted on silicon substrate with ~280 nm thermal silicon dioxide grown on

top. To activate the color centers and improve the crystal quality, the samples are annealed at 1000 °C for 30 min in Ar/H_2 atmosphere followed by naturally cool down. Single photon emitters are located by photoluminescence (PL) mapping and characterized by the emission spectrum.

The electrode patterns are defined the around the located single photon emitters by e-beam lithography. Afterwards, 5 nm Ti/100 nm Au are deposited by e-beam evaporation and lifted off to form the electrode. To precisely align electrode with nano-scale gaps to the emitters, we carefully record the position of the SPEs and align markers by taking SEM images in the e-beam lithography system and record the positions, based on which the electrode pattern with alignment coordinates are designed. The alignment markers are also fabricated by similar e-beam lithography, e-beam evaporation and liftoff to achieve high resolution after the promising SPEs are located by optical method. The SEM picture of a fabricated device is shown in Figure 3.2.

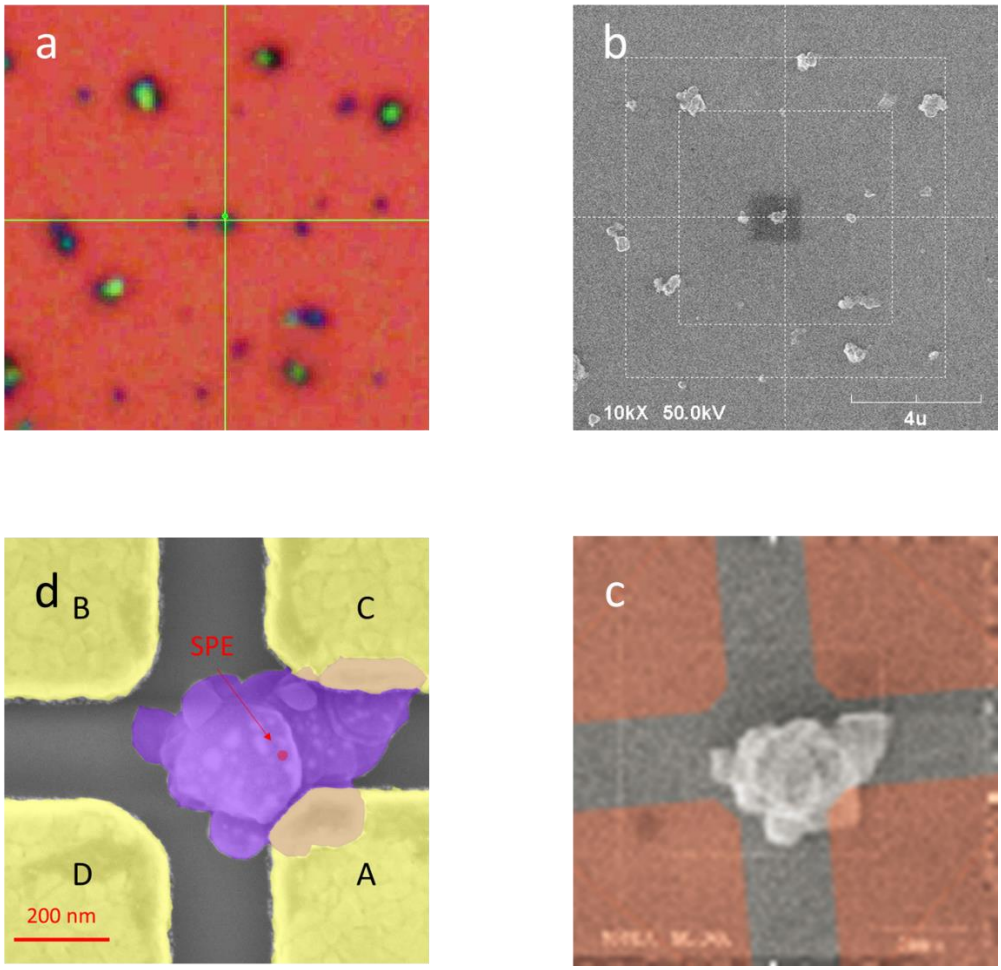

Figure 3.2 | Fabrication of electrically tunable *h*BN single photon emitter. a Optical microscope image showing the emitter position. The overlapped green color shows the emission intensity mapping. The nanocrystals with strong emission usually correspond to multiple emitters which are not appropriate for our experiment. The cross marks a single emitter whose emission spectra shows a strong single peak, which is used for device fabrication. b Wide field of view SEM image for electrode design. The target crystal is recognized by the distribution and sizes of the surrounding crystals. c Zoom-in SEM image overlapped by electrode design (red color). d SEM image of the

fabricated device. Good alignment is achieved between the electrode and the SPE. Pseudo colors are used to indicate the electrodes (yellow) and hBN crystal (purple). The red dot marks the position of color center located by localization image analysis.

3.4. Giant Stark shift at room temperature

We first check the optical emission after device fabrication to ensure the device quality. The emission spectrum obtained at room temperature without applying voltage is shown in Figure 3.3. A sharp and intense zero-phonon line (ZPL) is observed at 2.088 eV. The single-photon nature is verified by the second-order coherence function ($g^{(2)}$) ~ 0.45 at zero time delay (Figure 3.3 inset). The narrow FWHM ~ 7 meV is promising for characterizing Stark shift and future quantum information applications at room temperature.

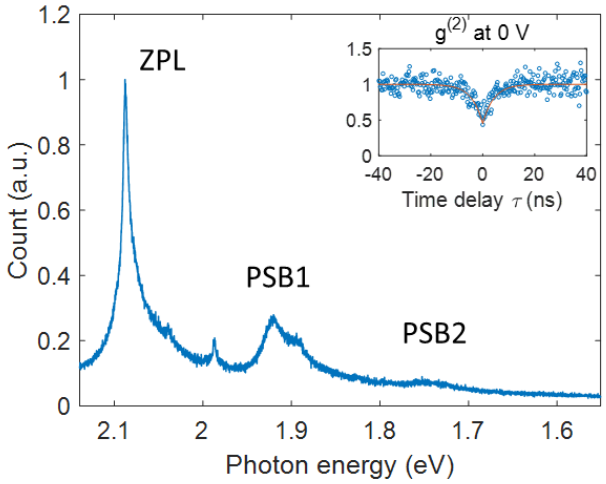

Figure 3.3 | Room-temperature optical characterization of the SPE without voltage applied. The narrow (FWHM ~ 7 meV) and intense ZPL at 2.088 eV demonstrates the high-quality single photon emission. Two small PSBs are observed at 1.921 eV (PSB1) and 1.753 eV (PSB2), with the frequency difference of ~1370 cm^{-1} which are identified as the E_{2g} phonon of *h*BN [109]. Inset shows second-order coherence function ($g^{(2)}$) after device fabrication using a Hanbury Brown and Twiss (HBT) setup, from which single photon emission is confirmed by a raw anti-bunching dip of $g^{(2)}(0) = 0.45$.

To achieve giant Stark shift, we apply voltages up to ±100 V between the electrodes A and B (Figure 3.4a inset) while collect PL emission spectra at each voltage. We use two Keithley 2400 sourcemeters to apply the voltage to the device. The zero-phonon line (ZPL) PL intensity map as a function of photon energy and applied voltage are shown in Figure 3.4a. A huge Stark shift of 31 meV is clearly observed. Comparing with its room-temperature linewidth (~ 7 meV), such a shift is 4-fold larger. To further analyze the effect, we extract the ZPL peak position, linewidth and intensity as a function of applied voltage in Figure 3.4 b, c and d, respectively. The Stark shift is approximately linear to the applied voltage with a tuning efficiency of 137 μeV/V. The reversal of the Stark shift at opposite electric field suggests a non-zero electric permanent dipole moment at the color center [96]. We notice a slight deviation from linearity, which is possibly due to the light induced ionization in nearby non-emitting defects [96]. The linewidth of the emission doesn't

strongly depend on the applied electric field, which is consistent with previous reports on color center SPEs [95,96,110]. The ZPL intensity gradually decreases when voltage changes from -100 V to 100 V, which is possibly due to the change of coupling to dark state as reported previously in diamond NV center [95,96]. The repeatability and stability of such room-temperature giant Stark effect are further confirmed in multiple emitters.

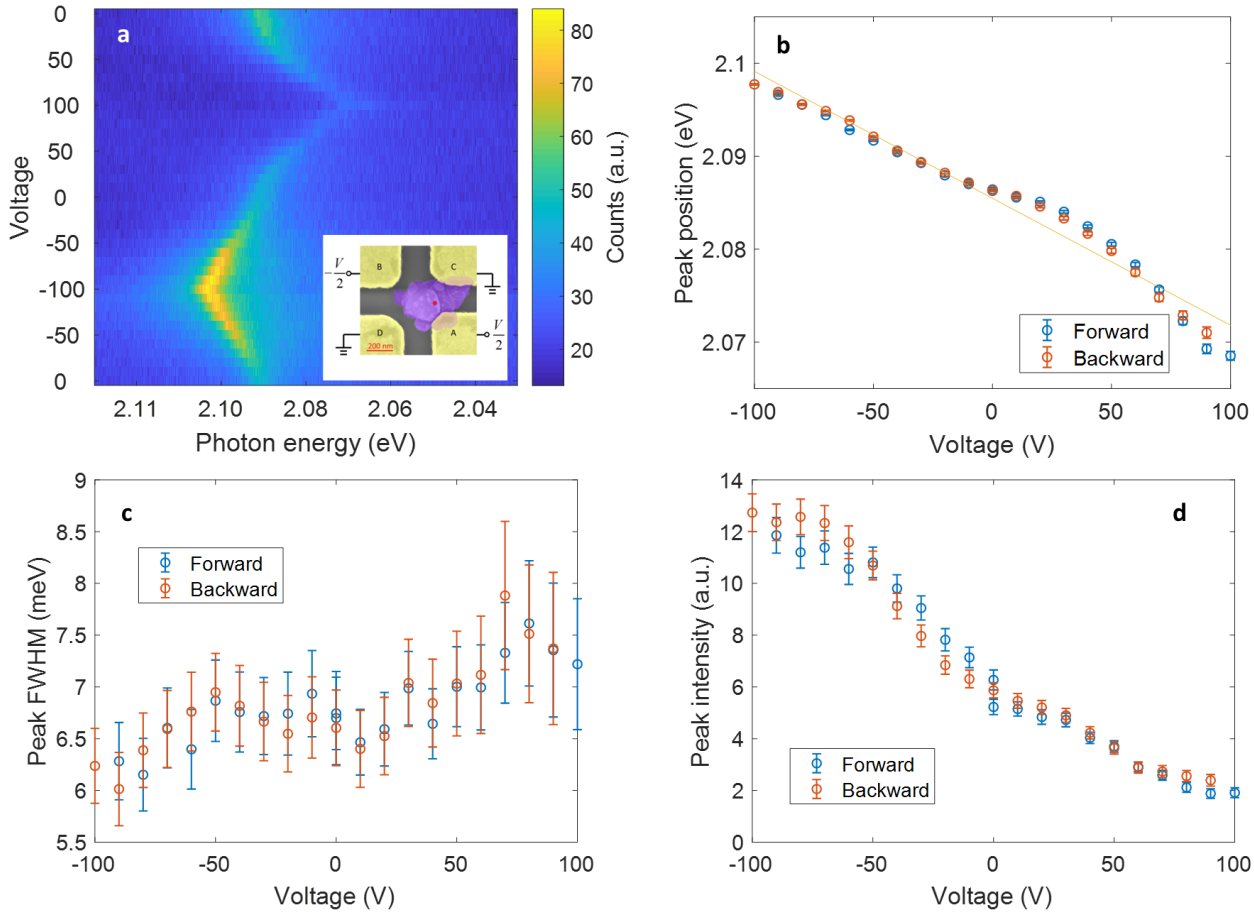

Figure 3.4 | Giant room-temperature Stark shift in *h*BN color center.

3.5. Angle-resolved Stark effect

To fully control the magnitude and orientation of the applied electric field, we apply two independently controlled voltage signals to electrodes A and C, while the other two electrodes and substrate are grounded. Because the total external field can be considered as linear combination of the fields generated by individual electrodes, we have the equation below:

$$\begin{bmatrix} E_x \\ E_y \end{bmatrix} = \mathbf{K} \begin{bmatrix} V_A \\ V_C \end{bmatrix} \tag{28}$$

where E_x and E_y are the x and y components of external electric field at the single photon emitter location, **K** is a 2-by-2 matrix, and V_A and V_C are the voltages applied to electrodes A and C respectively. Matrix **K** is obtained from 3D FEM simulation (COMSOL) using a geometry

extracted from the real device. The first column of **K** can be obtained by calculating E_x and E_y when assign V_A = 1 V and ground electrodes B, C, D. And the second column can be calculated similarly.

The amplitude F_0 and direction θ of the generated local electric field is linked to the applied field E_x, E_y by the following equation:

$$\begin{bmatrix} E_x \\ E_y \end{bmatrix} = \frac{F_0}{L} \begin{bmatrix} \cos(\theta) \\ \sin(\theta) \end{bmatrix} \tag{29}$$

in which Lorentz approximation is used to calculate the local field from the external field following previous works with $L = (\varepsilon_r+2)/3$ as the Lorentz factor. The relative permittivity ε_r is taken from a reference. Combining (28)(29) gives

$$\begin{bmatrix} V_A \\ V_C \end{bmatrix} = \frac{F_0}{L} \mathbf{K}^{-1} \begin{bmatrix} \cos(\theta) \\ \sin(\theta) \end{bmatrix} \tag{30}$$

which is used to calculate the voltages to A and C to generate a local electric field with desired amplitude and direction.

To facilitate the control of the voltage, we develop a LabVIEW program to calculate the voltages from the specified field direction and amplitude based on (30) and set the sourcemeters. To prevent damage the device due to sharp change of voltage, slow ramp is executed when a voltage change is commanded and before turning off the output.

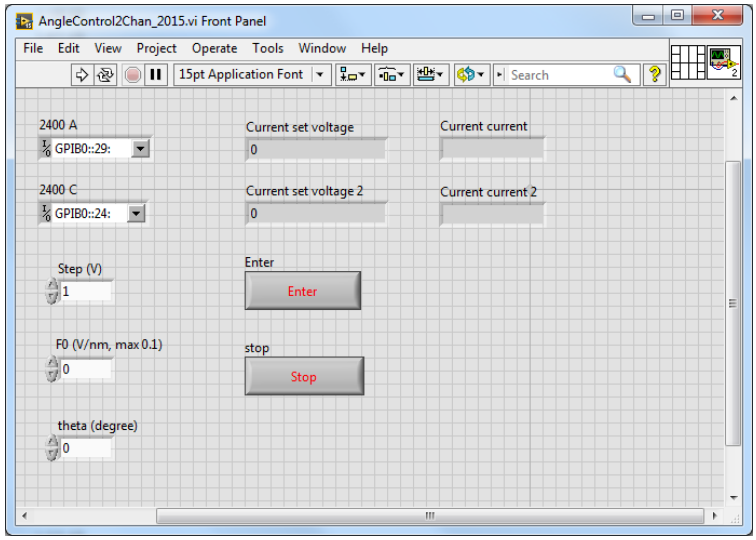

Figure 3.5 | Front panel of the LabView program to control the voltages on two electrodes according to specific field amplitude and direction. The Step is used to limit the magnitude of change per adjustment to prevent device damage.

With a fixed local electric field magnitude of 0.08 V/nm, we observe a 1.13 meV red shift of ZPL when the applied field pointing to 140°, while a 1.32 meV blue is obtained with electric field along 320°. The shift with the electric field along 230°, on the other hand, is negligible (Figure

3.6a). Based on perturbation theory to the first order the Stark shift $h\Delta\nu$ depends on the angle θ of the local field F as

$$h\Delta\nu = -\Delta\boldsymbol{\mu}\cdot\mathbf{F} = -\left|\Delta\boldsymbol{\mu}\right|\left|\mathbf{F}\right|\cos\left(\phi-\theta\right) \tag{31}$$

where $\Delta\boldsymbol{\mu}$ and ϕ denote the dipole moment responsible for the Stark effect and its orientation angle, respectively. We find our data can be well fit by (31), which further justifies that the Stark effect is dominated by an electric permanent dipolar term (Figure 3.6b). Such a fitting gives an estimation of the magnitude of the dipole as $|\Delta\boldsymbol{\mu}|$ = 0.65 ± 0.04 D where 1 D = 3.33e-30 Cm, which is on the same order as the NV center in diamond, consistent with its nature as an atomic defect.

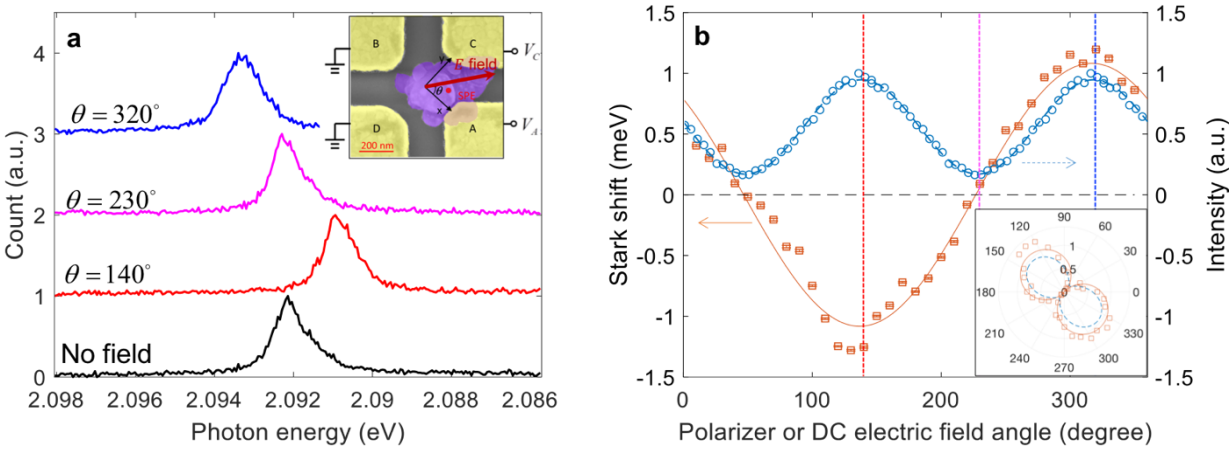

Figure 3.6 | Angle-resolved Stark effect of *h*BN SPE and the discovered symmetry breaking.

The discovered electric permanent dipole moment corresponds to the asymmetric charge distribution at the *h*BN SPE, which will facilitate the future study of the atomic structure and electronic levels of the color center. It can be calculated for the ground and excited states of an SPE as

$$\boldsymbol{\mu}_{\mathbf{g,e}} = \int \psi_{g,e}^{*}\, e\mathbf{r}\, \psi_{g,e} dr^3 \tag{32}$$

where ψ is the wave function of electronic states, and the subscriptions g and e correspond to ground and excited states, respectively. Such dipole moments contribute to Stark shift through $\boldsymbol{\Delta\mu}$ = $\boldsymbol{\mu}_{\mathbf{e}}$-$\boldsymbol{\mu}_{\mathbf{g}}$ (appears in (31)). A non-vanishing $\boldsymbol{\Delta\mu}$ indicates non-zero $\boldsymbol{\mu}_{\mathbf{e}}$ and/or $\boldsymbol{\mu}_{\mathbf{g}}$, which must result from non-inversion symmetric probability densities of electrons $|\psi_e|^2$ and/or $|\psi_g|^2$ as well as atomic structure.

On the contrary, the optical polarization is determined by optical transition dipole moment which emits photons with electric field parallel to the dipole

$$\boldsymbol{\mu}_{e\to g} = \int \psi_{g}^{*}\, e\mathbf{r}\, \psi_{e} dr^3 \tag{33}$$

And those photons propagate along the directions normal to it. After polarizer, the detected optical intensity has a squared-cosine dependence $I(\theta) = I_0\cos^2(\theta)$ on polarization angle θ, which returns itself after $\theta\longrightarrow\theta$+180°. As such measurement is always inversion symmetric, it cannot tell whether inversion symmetry breaks or not at the emitter. We clarify such distinctive difference in Figure

3.6b (blue circles). It should be noted that the direction for maximum Stark shift is coincident with that of the emission polarization (Figure 3.6b inset), which may correspond to the intersection of the mirror symmetry plane of the color center and the *h*BN atomic layer plane.

3.6. Conclusion

We observe room-temperature Stark effect of an SPE with a giant shift more than 30 meV by integrating nanoelectrodes with *h*BN color centers. The tuning range exceeds 4 times of the linewidth of the single photon emission, which is promising for scaling up optical quantum information systems by using wavelength division multiplexing and indistinguishable single photons at room temperature. We further characterize the angle-resolved Stark effect and uncover the intrinsic broken symmetries of color centers in *h*BN. Our results provide fundamental knowledge for the understanding and applications of color centers in vdW materials and open a new route towards scalable solid-state quantum information systems at room temperature.

Chapter 4 Manipulate electromagnetic response of 2D electron gas by magnetic field and electron concentration

4.1. Background

A magnetic field breaks time-reversal-symmetry. In a two-dimensional system, such symmetry breaking can result in nontrivial band topology, which allows the formation of topologically-protected one-way excitations along the physical edges with abrupt change in material properties [111–113]. Furthermore, because a change of magnetization results in an internal topological transition, corresponding to a synthetic edge, even for a system that is uniform except for an inhomogeneous magnetization, another exotic form of edge excitation, the kink modes, have been predicted along the magnetic domain boundaries [56,111–116].

Similar kink modes have been observed in both the low-frequency fermionic (electronic) and high-frequency bosonic (photonic) valley-Hall systems [117,118]. However, in those scenarios, the time-reversal-symmetry is preserved. On the contrary, time-reversal-broken kink modes have only been observed in the fermionic system [119]. Various bosonic (photonic, plasmonic, magnonic, excitonic) counterparts have been predicted [115,120–126], yet are to be demonstrated in experiment.

Two-dimensional electron gas (2DEG) in high-mobility GaAs/AlGaAs heterojunctions is an ideal platform for the such a realization [2,3]. 2DEG host electron-density oscillations which can be modeled as plasmon modes. Without a magnetic field, the dispersion starts from DC to high frequency without a bandgap [56]. A perpendicular magnetic field opens a bandgap for the bulk MPs up to a cyclotron frequency, where magnetoplasmons (MPs) start to form [54]. In GaAs/AlGaAs system, MPs cover a broad spectral range from radio to microwave frequencies, which embody a prototypical band topology of bosonic excitations [56,115]. Moreover, due to the non-trivial topological properties introduced by the magnetic field, topologically-protected edge magnetoplasmons (EMPs) forms to bridge the bulk gap and exhibit unidirectional propagation along system's boundaries [127]. The high electron mobility ~10^7 $cm^2V^{-1}s^{-1}$ of our 2DEG allows an ultra-long relaxation time up to hundreds of picoseconds and ultra-low damping rate down to a few gigahertz, advantageous over most existing 2DEG systems [127–129].

Specifically, the plasmon dispersion can be calculated from the continuity equation and a constitutive equation including the longitudinal Coulomb force and transverse Lorentz force as [56]

$$\begin{aligned} \omega\rho(\mathbf{r},\omega) &= -\mathrm{i}\nabla\cdot\mathbf{j}(\mathbf{r},\omega) \\ \omega\mathbf{j}(\mathbf{r},\omega) &= -\mathrm{i}\frac{e^2}{m_*}n(\mathbf{r})\nabla\Phi(\mathbf{r},\omega) - \mathrm{i}\omega_c(\mathbf{r})\mathbf{j}\times\hat{\mathbf{e}}_z. \end{aligned} \tag{34}$$

Here ρ and **j** are the surface charge and current density. e, m_* and n are the electron charge, effective mass and density. In our system, $m_* = 0.067\ m_e$. The Coulomb interaction is represented by the self-consistent potential

$$\Phi(\mathbf{r},\omega)=\int V(\mathbf{r}-\mathbf{r}')\rho(\mathbf{r}',\omega)\mathrm{d}^2\mathbf{r}' \tag{35}$$

And the magnetic field takes effect through the cyclotron frequency

$$\omega_c(\mathbf{r})=\frac{eB(\mathbf{r})}{cm_*}. \tag{36}$$

Consider a 2D system with rotation symmetry with a hard wall boundary condition at R = 10 mm >> the radius of magnetic boundary, the solution of (34) can be represented by linear expansion of Bessel functions [56]

$$j_s(r,\varphi)=\left[\sum_{n=1}^{N\to\infty}A_{n,s}\mathrm{J}_{m+s}(q_{mn}r)\right]\exp\left(i\left(m+s\right)\varphi\right). \tag{37}$$

Here φ and m are the azimuthal angle and angular wavenumber. n is the order of mode. $J_k(x)$ is the kth order Bessel function. q_{mn} is the radical wavenumber. s = 0, ±1 denotes a spin index corresponding to the "scalar-potential (density-fluctuation)" current and chiral representation of current components

$$\begin{aligned} j_0&=\omega_0\Phi \\ j_{\pm1}&=\frac{1}{\sqrt{2}}\left(j_r\mp\mathrm{i}j_\varphi\right)\exp\left(\mp i\varphi\right). \end{aligned} \tag{38}$$

where j_r and j_φ are current density along the radial and azimuth directions. The effect of electron density n takes effect through the characteristic plasmon frequency

$$\omega_0=\sqrt{\frac{e^2n}{m_*R}}. \tag{39}$$

Using the expansion (37), the eigen value problem can be written as

$$\frac{\omega}{\omega_0}\begin{pmatrix}\mathbf{A}_{+1}\\ \mathbf{A}_0\\ \mathbf{A}_{-1}\end{pmatrix}=\begin{pmatrix}+\mathbf{W} & +\frac{q_{mn}R}{\mathrm{i}\sqrt{2}}\mathbf{I} & 0\\ -\frac{2\pi\beta(q_{mn})}{\mathrm{i}\sqrt{2}}\mathbf{I} & 0 & +\frac{2\pi\beta(q_{mn})}{\mathrm{i}\sqrt{2}}\mathbf{I}\\ 0 & -\frac{q_{mn}R}{\mathrm{i}\sqrt{2}}\mathbf{I} & -\mathbf{W}\end{pmatrix}\begin{pmatrix}\mathbf{A}_{+1}\\ \mathbf{A}_0\\ \mathbf{A}_{-1}\end{pmatrix}. \tag{40}$$

Here $\mathbf{A_s}$ = ($A_{1,s}$, $A_{2,s}$, …, $A_{N,s}$) are the coefficients in (37), where N is a cutoff mode order large enough for the desired spectrum resolution (N = 2000 is used in this work). $\beta(q)$ is the wavenumber dependent screening function. The magnetic field is modeled as

$$B\left(r\right)=B_0+\mathrm{sgn}\left(r-a\right)\Delta B. \tag{41}$$

And the effect of magnetic field is reflected by

$$\mathbf{W} = \frac{e}{\omega_0 m_* c}\left[2\Delta B\mathbf{Y}^{-1}\mathbf{X} + (B_0 - \Delta B)\mathbf{I}\right], \tag{42}$$

where $\mathbf{X}$ and $\mathbf{Y}$ are $N\times N$ matrices determined by the geometry.

By solving the eigen value problem (40), the mode dispersion and profile can be obtained as shown in Figure 4.1. The ungated case where n_0 =1e11 cm^{-2}, B_0 = 0 T, and ΔB = 0.15 T is presented in Figure 4.1a. The spectrum exhibits particle-hole symmetry, i.e. $\omega_{n,\,m} = -\omega_{n,\,m}$, with a zero-frequency band describing static modes. The bulk MPs in each magnetic domain contains a gap from zero frequency to the cyclotron frequency ~ 60 GHz. The band topology of each domain, considered as an extended bulk, is characterized by a topological invariant, the Chern number, equaling $C = -\,\mathrm{sgn}(B(r)) = \mathrm{sgn}(a - r) = \pm 1$ [56]. The associated gap Chern number $\bar{C}$, also equaling ±1 in this case, can be identified, whose difference across the domains, $\Delta\bar{C} = 2$, dictates the existence of two unidirectional edge states localized at $r = a$. From the viewpoint of bulk-edge correspondence, the two different regions of the 2DEG with oppositely biased magnetic field are sharing a bulk band gap while they have different topological phases. It is impossible to continuously transform one part into the other without closing the common gap (the topological properties cannot be changed unless we close the gap and re-open it up again). Therefore, at the transition domain from inside toward outside of the circle (from positive bias toward the negative bias) there is a point that the bulk band should be closed, and this is the point that the unidirectional edge modes (domain-boundary kink modes) appear.

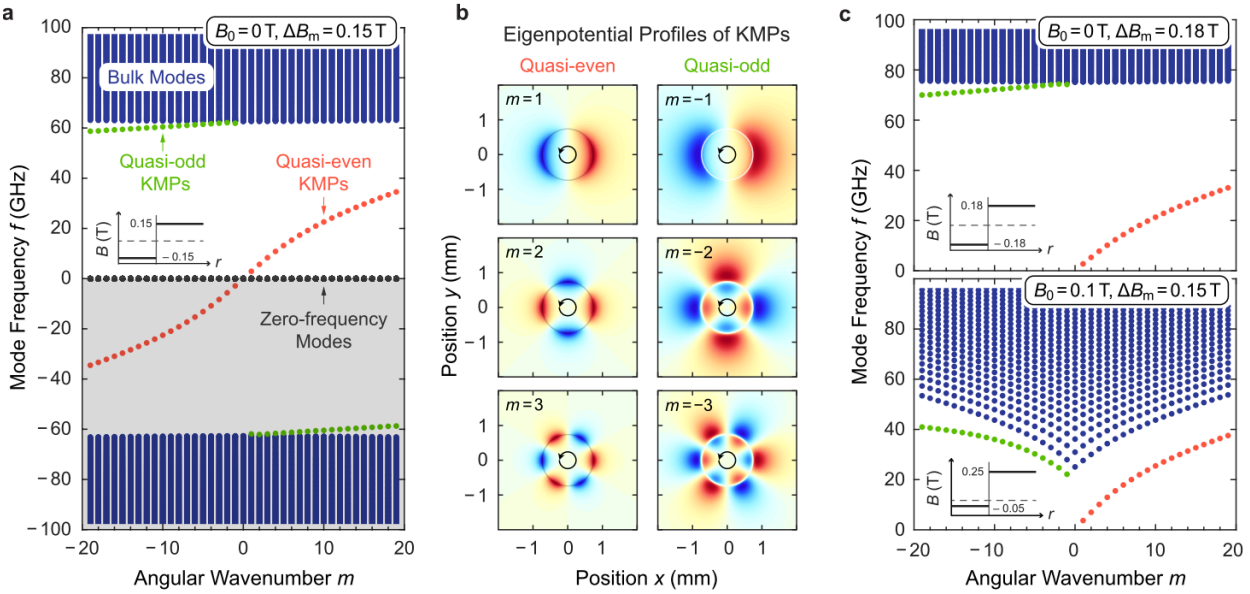

Figure 4.1 | The dispersion and model profile of topological kink magnetoplasmons (KMPs).

These conclusions are manifested in Figure 4.1 a and b from the existence of quasi-even and quasi-odd KMP branches (so named due to their asymptotic association with the even and odd KMPs of a linear domain boundary). Both are unidirectional and exhibit increasing localization with incrementing angular wavenumbers m. They differ from the conventional topologically-protected edge magnetoplasmons (EMPs) even at the microscopic level. For EMPs, the electron-

density waves hit an electrical barrier where the momentum is immediately reversed. But for KMPs, the electron-density waves hit a magnetic barrier where the Lorentz force is reversed. There are classical analogies to the two kinds of KMPs and topologically equivalent to the equatorial Kelvin and Yanai waves of the ocean and atmosphere with a Coriolis parameter replacing $B(r)$ [130].

Figure 4.1c shows the dispersion for increased ΔB (from 0.15 T to 0.18 T) and B_0 (from 0 to 0.1 T). Comparing to Figure 4.1a, increasing ΔB widens the bandgap and decreases the frequencies of the quasi-even KMPs. Conversely, increasing B_0 (but maintaining $B_0 < \Delta B$) reduces the overall gap -- since the cyclotron frequency is lowered in the inner domain -- and increases the excitation frequencies of the quasi-even KMP. This latter behavior further distinguishes our new KMPs from the traditional EMPs which shift in the opposite direction with increasing B_0 [127,131]. The quasi-odd KMP branch in Figure 4.1c appears as though they are not gapless. This puzzle, however, is remedied at larger |m| where the quasi-odd dispersion curve turns downwards towards the zero-frequency modes, same as Figure 4.1a and Figure 4.1c. This reinstates an asymptotically gapless behavior fulfilling the topological requirements of MP systems.

This chapter presents the experimental realization of such KMP. The major results will be reported in an upcoming publication [132].

4.2. Device design

With an innovative device design (Figure 4.2a), we create edge magnetoplasmons (EMPs) using a space-varying magnetic field $\mathbf{B}(\mathbf{r}) = B(\mathbf{r})\mathbf{e}_z$ inside the 2DEG where $n(\mathbf{r})$ is homogenous, which is in contrast with the approach of using a sharp termination of electron density $n(\mathbf{r})$ at sample edges to form EMPs, as has always been done in any 2DEG systems [133–135]. We realize such magnetic field by a holed NdFeB strong permanent magnet, which generates a sign-changing magnetic field about ±0.15 T in two different domains, sufficient to open a bandgap the bulk MPs. The 2DEG resides in a GaAs/AlGaAs heterojunction, which is cladded above and below by a fused-silica spacer and a GaAs substrate, respectively. The permittivity and thickness of fused-silica is ε_A=3.8 and d_A = 100 um, while for the substrate the specification is ε_B=12.8 and d_B = 150 um. This dielectric-2DEG-dielectric structure is enclosed in a metallic cavity along z direction, terminated at the spacer's top and substrate's bottom. The holed NdFeB permanent magnet is installed on the top of the cavity to introduce the desired circular magnetic field $\mathbf{B_m}(\mathbf{r}) = B_m(r)\mathbf{e_z}$ onto the 2DEG. The sign of $B_m(r)$ changes sharply across the projection of the hole's radius, a = 0.75 mm, producing the adjacent oppositely-signed magnetic domains. A tunable uniform magnetic field $\mathbf{B_0} = B_0\mathbf{e_z}$ from a superconducting coil is applied to the system, allowing an overall shift of the field profile.

The schematic for the actual device is shown in Figure 4.2b. We use a heterojunction sample with a 12 mm x 6 mm rectangular footprint. A 9 mm x 3 mm Hall bar is fabricated on it, allowing *in-situ* measurements and control of the 2DEG electron concentration n_0. A 100 nm thick Cr is evaporated on the top of the fused silica spacer, which is used simultaneously as upper cavity wall and gate electrode [136,137]. A gate voltage $V_g \sim \pm 100$ V can be applied to the capacitor structure comprised of the metal-2DEG capacitor to tune the electron concentration. The sample-spacer-magnet assembly is glued by Poly(methyl methacrylate) (PMMA) onto a customized Cu printed

circuit board (PCB) with a 5 um Ni and 200 nm Au surface finish, where a coplanar waveguide (CPW) connecting RF Ports 1 and 2 with mini-SMP connectors are hosted. By design, the CPW has a 50 Ω impedance with the sample-magnet assembly loaded. All the components are designed symmetrical with respect to the hole on the magnet and the CPW signal line, which facilitates aligning the CPW signal line to the projected circle from the hole of magnet tangentially to maximize the microwave-KMP coupling.

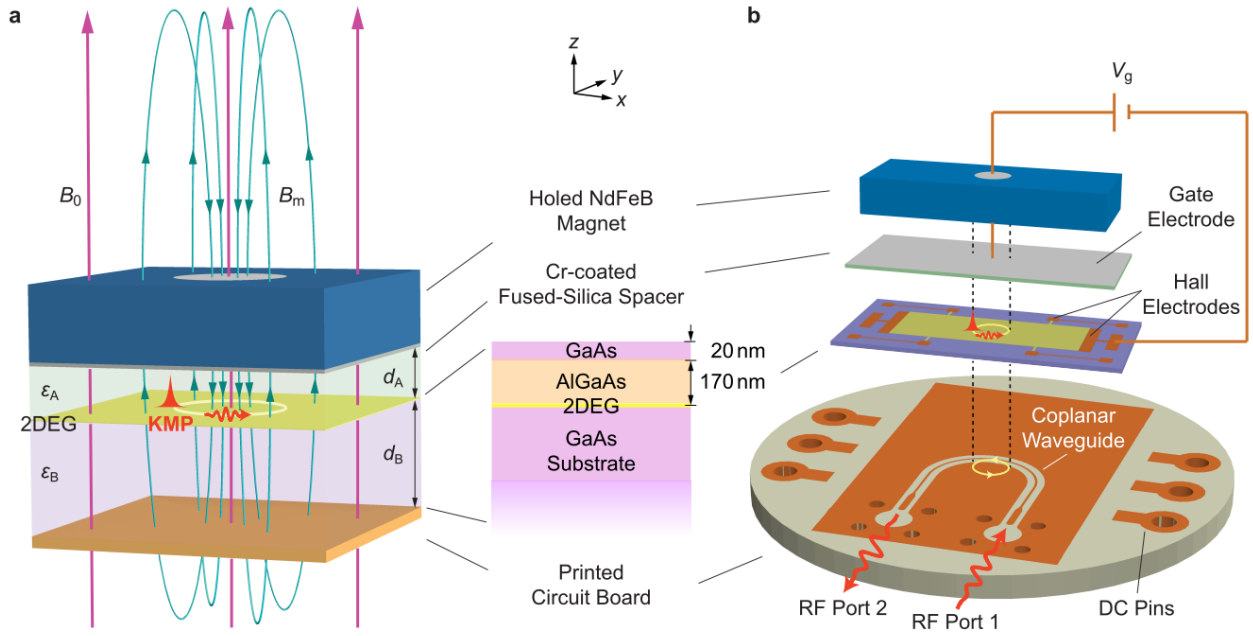

Figure 4.2 | Realizing kink magnetoplasmons using patterned magnetic field.

4.3. Chip design and fabrication

We carefully design the chip layout for measuring and tuning electron density measurement using Hall effect and electrostatic gating, respectively. As shown in Figure 4.3, a rectangular channel is designed at the center of the chip. The 2DEG outside of the channel region is removed by wet etch. Two wide Ohmic contacts are located along the shorter edge as source and drain electrodes. Four small Ohmic contacts are distributed on the shorter edge as voltage probes, which are extended into the channel for proper termination of the 2DEG. We place large metal pads for wire-bonding according to the PCB design. And we route metal strips to connect the Ohmic contacts to those pads. Besides, to ensure the patterns are located at the center of the chip, we add alignment bars at the chip corner, which also tolerate small chip size variance to the limited precising in hand-cutting. The alignment between different layers are achieved through alignment markers that intentionally put far away from the channel to avoid disturbing electric measurement. We intentionally add some patterns beyond designed chip outline to facilitate the locating of the chip edge.

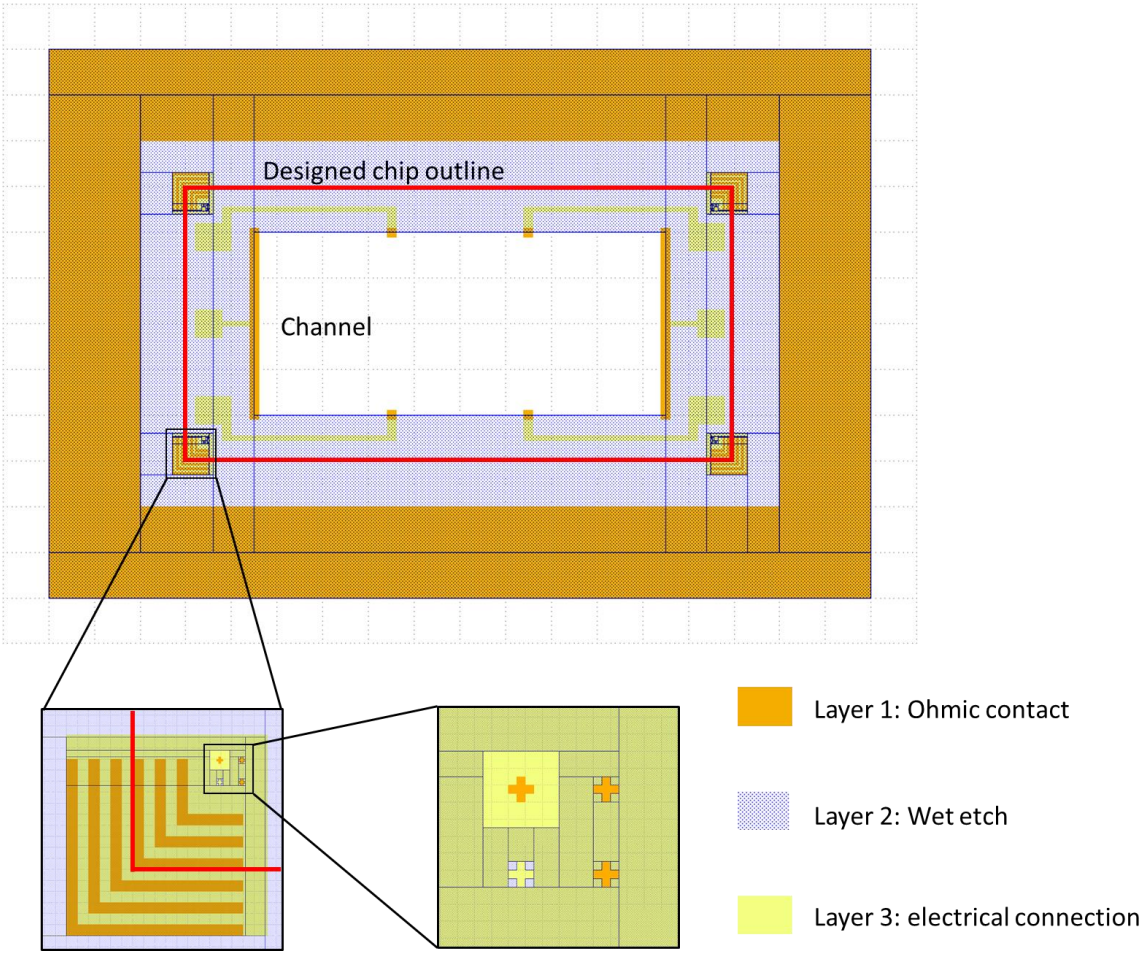

Figure 4.3 | Chip design schematic.

The fabrication starts from a single interface GaAs/$Al_xGa_{1-x}As$ (x = 0.22) heterojunction grown by molecular beam epitaxy (MBE) on a 500 μm thick GaAs wafer. We first make the Ohmic contacts, then realize the channel geometry, and finally place the metallic pads and strips for off-chip electrical connection, so that the signal wiring doesn't affect the 2DEG in the channel. To make the Ohmic contacts, we use UV lithography to define the pattern with positive photoresist. Then a stack of 30 nm Ge/60 nm Au/ 15 nm Ni/ 65 nm Au is deposited using e-beam lithography. After liftoff in acetone, the samples are annealed in a quartz tube while purged with 1000 sccm Ar/180 sccm H_2 at atomsphare pressure at 450 °C for 15 min to achieve Ohmic contact. Next, UV lithography is used to define the pattern to etch the 2DEG to form the channel geometry. The sample is etched in H_2O_2(30%)/H_2SO_4(96%)/H_2O with volume ratio 1:1:8. After removing the photoresist in acetone, another UV lithography is used to define the pattern for off-chip contacts and on-chip connection. 5 nm Ti/100 nm Au is deposited by e-beam lithography and lifted-off in acetone. Finally, the chips are polished from the backside to achieve a thickness ~ 100 μm to enhance the coupling between the 2DEG on top and the CPW on the PCB underneath the chip. The detailed fabrication steps are also shown in Figure 4.4. After fabrication, the typical resistance measured at room temperature between source and a nearby voltage probe and that between source and drain are ~ 3 kΩ and ~ 7 kΩ, respectively, indicating good contacts are formed.

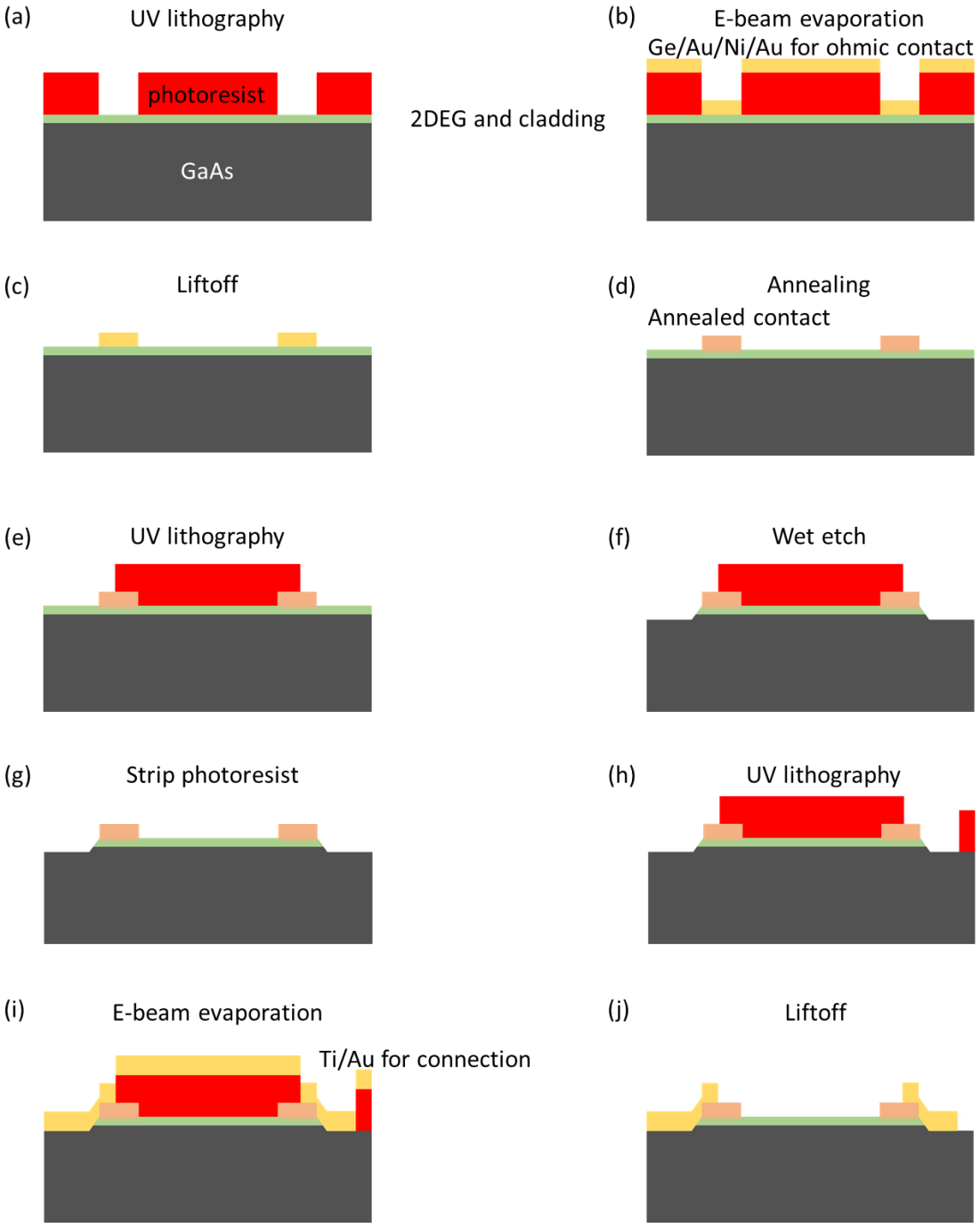

Figure 4.4 | Fabrication steps for the electrical connection to the 2DEG chip.

4.4. Experiment results

We conduct Hall measurement at T = 0.3 K in dark to characterize the electron concentration n_0 and mobility μ. The result is shown in Figure 4.5, corresponding to $n_0 = 0.95\times10^{11}$ cm^{-2} and $\mu = 8.6\times10^{6}$ cm^{2}V^{-1}s^{-1}. During our actual microwave measurement, we insert the device into a He-3

cryostat running at 0.5 K. We also monitor the electron concentration using Hall effect and the typical zero-gate electron concentration is measured to be about 1×10^{11} cm^{-2} and used in our calculation.

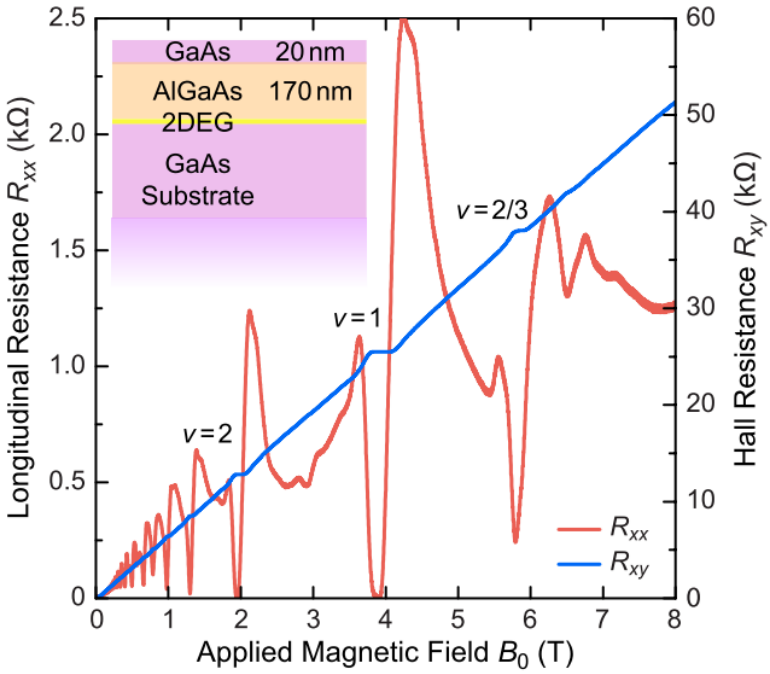

Figure 4.5 | Quantum Hall effect in 2DEG sample.

To seek experimental evidence for the theoretically calculated KMPs, we characterize the microwave transmission and reflection through the CPW coupled to the 2DEG. An Agilent E5071C Network Analyzer (NA) is used to acquire power transmission S_{21} (Port 1 to 2) and S_{12} (Port 2 to 1) in the frequency range 300 kHz to 20 GHz [125,136,137]. We focus our measurement to the frequency range 1-10GHz, beyond which the cables and NA bear high loss and noise, prohibiting acquisition of clear signals. In such a frequency range, according to Figure 4.1 a and c, we expect to observe characteristic absorption associated with the m = 1 and 2 quasi-even KMPs. Although the quasi-odd KMPs also fall into such spectral range, it only happens at extremely large (angular) momenta. As a result, their non-dispersive nature will only produce a broad absorption background in the spectrum with no resolvable resonances.

In the first series of measurements, we keep the gate grounded, V_g = 0 V, and investigate the influence of the applied magnetic field B_0 on the resonant absorption of quasi-even KMPs in S_{21}. Here, we choose B_0 = 0.2 T as baseline, which provides a high enough suppression of unwanted low-frequency bulk modes, yet dose not exert too great a torque on the magnet-sample assembly. After dividing all signals by this baseline, we obtain data as shown in Figure 4.6. For every S_{21}-spectrum, each reflecting a single applied field in the range B_0 = 0 to 0.1 T, we observe two well-defined absorptive resonances, corresponding to the m = 1 and 2 right-circulating quasi-even KMPs, spanning from 3 to 4 GHz and 6 to 8 GHz, respectively. They exhibit linewidths of approximately 1 to 2 GHz, roughly consistent with the Hall-probe inferred DC damping rate $\gamma \sim 2.6$ GHz.

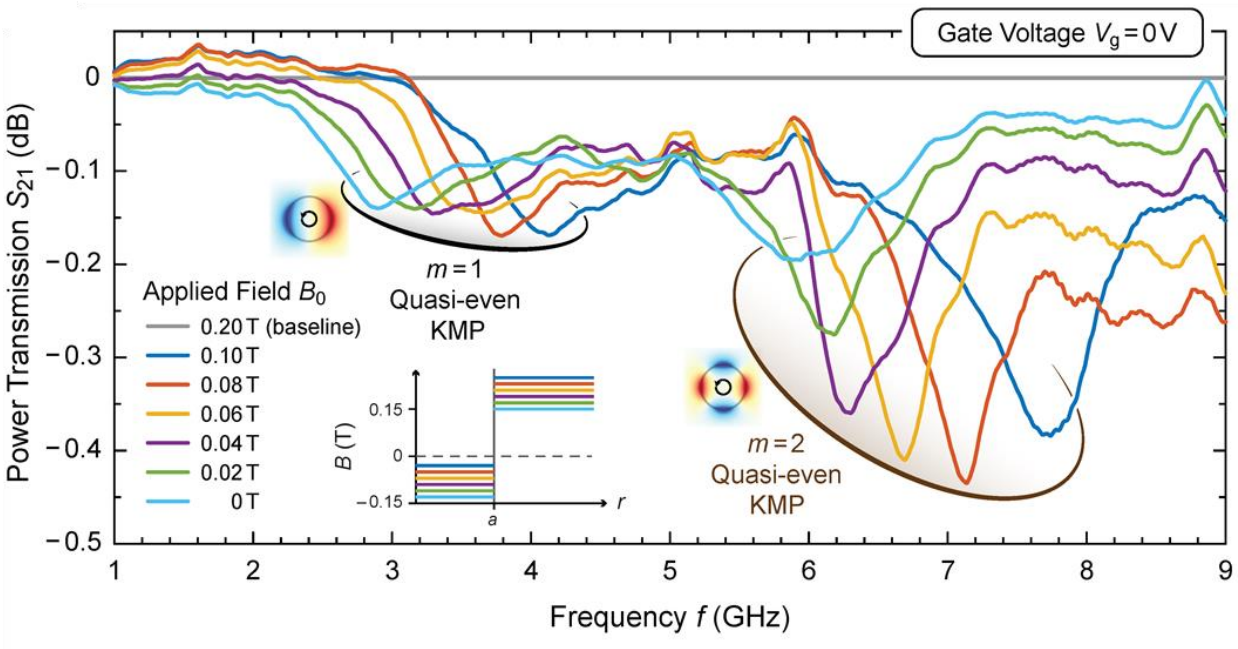

Figure 4.6 | Magnetic-field-dependent microwave transmission spectra.

The measured resonance frequencies are compared with theoretical prediction in Figure 4.7. They exhibit excellent agreement even in the absence of fitting parameters. Moreover, we emphasize the monotonously increasing excitation frequencies with increasing B_0, which unambiguously differentiates our magnetically-defined KMPs from the conventional EMPs.

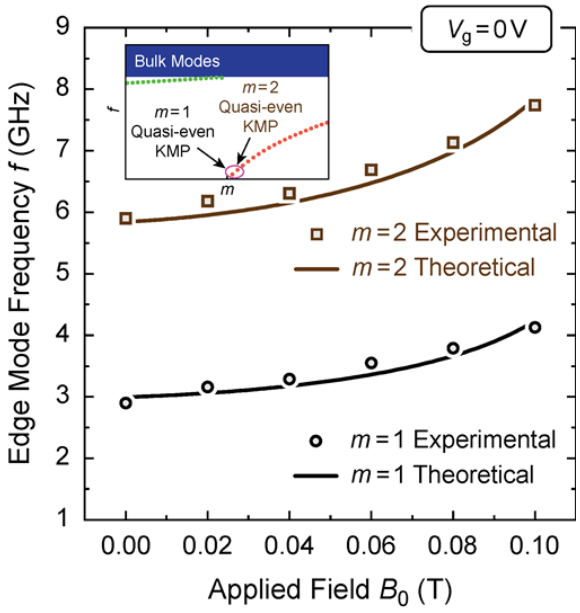

Figure 4.7 | Comparison between the experimental and theoretical magnetic-field-dependent edge mode frequency.

In the second series of measurements, we fix the applied magnetic field B_0 = 0 T and explore the KMPs' dependence on the gate voltage V_g, which reflects its electron-density dependence. The baseline is chosen at V_g = -80 V, which corresponds to an essentially electron-depleted 2DEG supporting no plasmonic modes. Once more, after dividing the signal with that baseline, we obtain data shown in every spectrum in Figure 4.8. Each curve now corresponds to distinct gate voltages in the range V_g = -20 to +20 V and still exhibits two clear absorptive resonances associated with the m = 1 and 2 quasi-even KMPs. Increasing the gate voltage (or, equivalently, the electron concentration n_0) blue shifts the KMP frequency, as expected. Moreover, the extinction depth of each resonance also increases with the V_g.

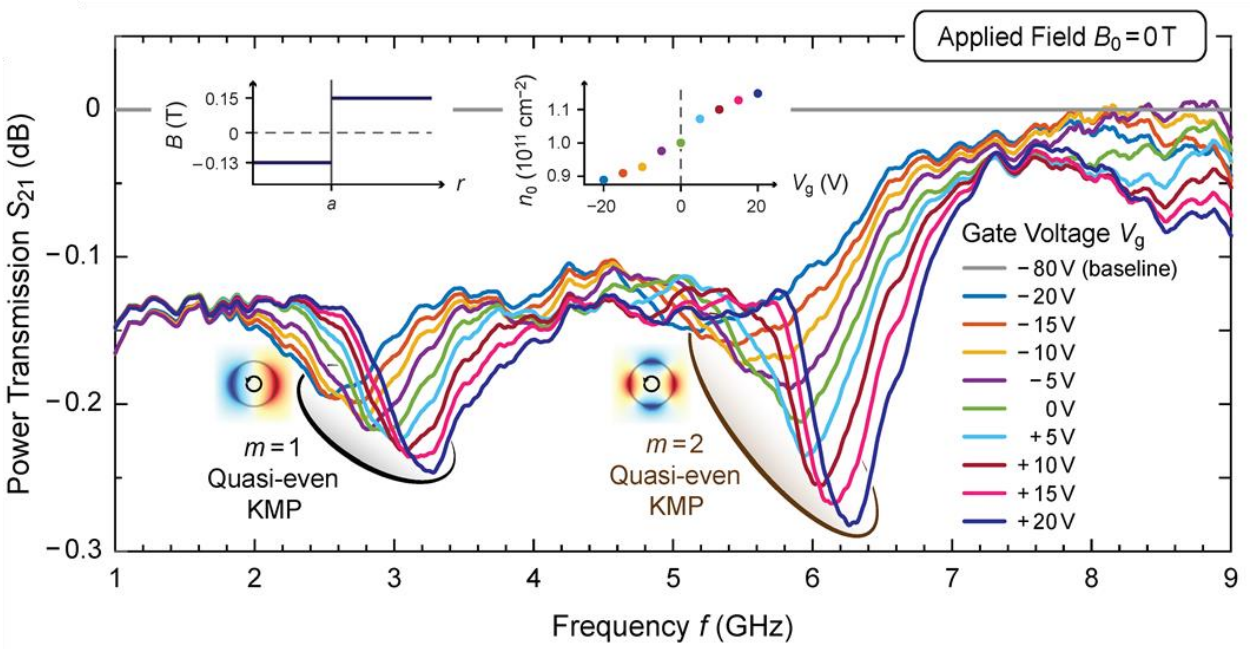

Figure 4.8 | Gate voltage-dependent microwave transmission spectra.

We also compare the extracted edge mode frequency with the theoretical prediction based on the electron concentration for each voltage. According to the f-sum rule [138], a linear increase of integrated extinction with increased n_0 is expected (disregarding the negligible spectral dispersion in the microwave-KMP coupling). As shown in Figure 4.9, we once again find excellent agreement.

Our device also enables explicitly demonstration of the underlying unidirectional character of the KMPs by characterizing its nonreciprocal properties. Since the KMPs are right-circulating in the bandgap, S_{21} and S_{12} correspond to the "easy-coupling" and "hard-coupling" directions, respectively, of our device (Figure 4.2). Using the same sample and magnet, we examine the different response of those two propagation directions with results shown in Figure 4.10, in which each coupling direction is normalized separately with baselines taken at B_0 = 0.2 T. The 2DEG is gated by V_g = 40 V, to obtain a pronounced extinction depth, and the applied magnetic field is turned off (B_0 = 0 T). In this configuration, the m = 1 and 2 quasi-even KMPs exist at 4.2 GHz and 8.0 GHz, respectively. Comparing S_{21} and S_{12}, we observe distinct asymmetry of extinction depth at each resonance, with S_{12} exhibiting shallower extinction. This asymmetry is indicative of the unidirectional character of the KMPs.

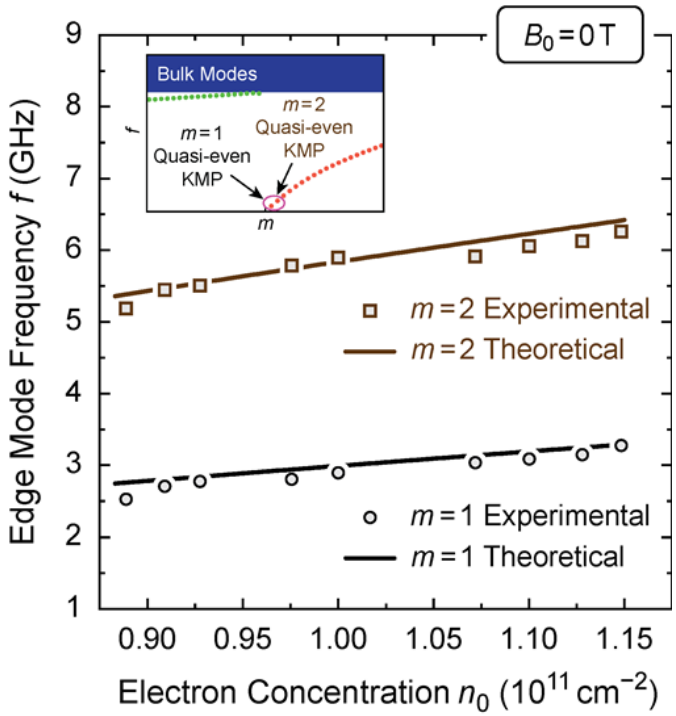

Figure 4.9 | Comparison between the experimental and theoretical electron-concentration-dependent mode frequency.

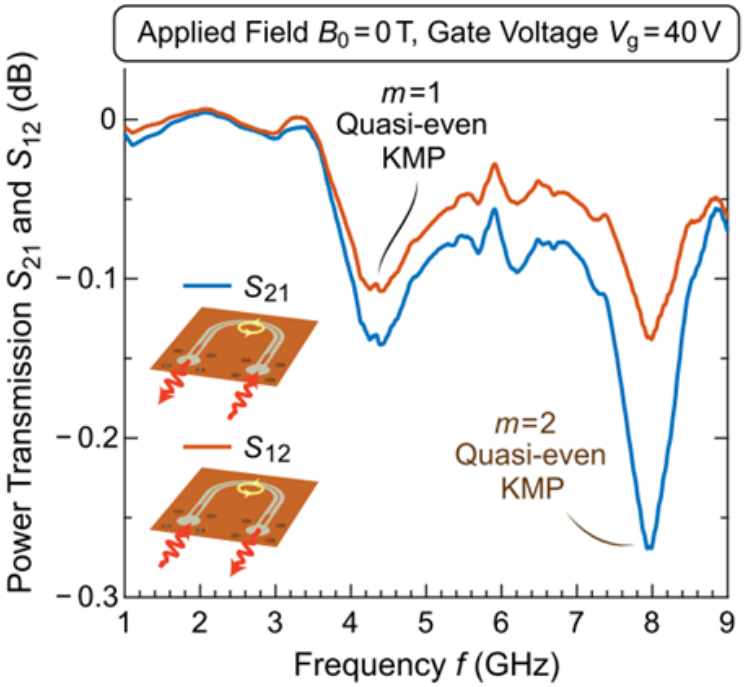

Figure 4.10 | Unidirectional character of the KMPs demonstrated by nonreciprocal microwave coupling.

The isolation ratio $S_{21}/S_{12} = \left(S_{21} - S_{12}\right)_{\mathrm{dB}}$ attained from our current experiment is limited by the evanescent-photon-plasmon coupling technique. It is important to stress that the KMPs themselves are always unidirectional, independent of the properties of the photons used to probe them. However, in order to observe a sharp isolation contrast, one generally has to deliver photons to a probe that is much smaller than the wavelength of the edge (or kink) modes [120,133,135,139]. On the contrary, the probing technique compatible with our device here employs evanescent waveguide-photons leaked through the substrate and is much longer than the KMP wavelength. According to our full-wave simulation for the wavelengths and mode profiles of microwave photons along the CPW, at f = 8 GHz excitation frequency (corresponding to the m = 2 quasi-even mode resonance), the waveguide photon wavelength is about 1 cm, whereas the KMP (angular) wavelength is about 2 mm. As a result, across their circulating diameter, the KMPs only see a slowly varying (quasistatic) background of photon field with weak coupling for both directions. The less-than-$\pi/5$-phase variation cannot exclusively distinguish the left-traveling and right-traveling photons in the waveguides. Nonetheless, despite this wavelength-mismatched weak-coupling limit, the nonreciprocal nature of KMPs is evident.

4.5. Conclusion

A magnetic field opens the bandgap at the plasmon dispersion in 2DEG system. Due to the topological property of the band structure, edge states are created connecting the two bands. While traditionally such edge states are only observed along an actual edge of the 2DEG, where the electron concentration is sharply terminated, in this work, with an innovative design, we experimentally realize similar excitations at the engineered magnetic-domain boundaries within a homogeneous edgeless two-dimensional electron gas (2DEG). Such high-frequency kink magnetoplasmons (KMPs) are topologically and microscopically distinct from the conventional edge magnetoplasmons (EMPs). The dependence of resonant frequency on magnetic field and carrier density obtained from our device is in excellent agreement with the theoretical prediction, indicating the well-described underlying physics. Although a simple circular magnetic domain boundary generated by a macroscopic holed permanent magnet is used in this study, sophisticated boundaries can be generated, by using magnetic thin films and advanced nanofabrication technologies. Our result thus can be useful for developing integrated topological circuits [121,125,126].

Chapter 5 Create and control magnetic domain wall in a few-layer van der Waals ferromagnetic metal

5.1. Background

In ferromagnetic materials, due to the exchange interaction and magnetic anisotropy, the net electron spins can form long range magnetic order, manifested as magnetization. The motion of electrons is strongly coupled to the orientation of magnetization through the spin-based interaction [140]. On one hand, the electronic response, represented by the resistivity tensor, is controlled by the orientation of the magnetization, as discovered in the planar Hall effect [141–145] and giant magnetoresistance (GMR) [146–150]. On the other hand, the magnetization can be rotated upon a spin polarized current, via spin transfer torque [140]. The study on the control and application of the spin degrees of freedom, known as spintronics, have not only reshaped our understanding on the spin-related transport, but also brought vital technology innovations [150]. The technology breakthrough brought by GMR have boosted the areal recording density by more than two orders of magnitudes (from ~1 to ~600 Gbit/in^2 in 2007) [150]. It opens the way to both high volume and portable data storage and further enables the revolutionary development of big data.

The magnetic domain walls (MDWs), separating magnetizations with reversed orientations, is a key component for ferromagnetism and spintronics. It enables, for example, an efficient way for information storage and processing by using electrically controlled MDWs in Permalloy ($Ni_{80}Fe_{20}$) thin films [151–153]. Furthermore, chiral edge states can be created in topological insulator, such as chromium-doped $(Bi,Sb)_2Te_3$, when it is coupled with a MDW coupling domain [112]. Due to the topological protection, those states are promising dissipationless channels for data interconnection [112,154,155].

Recently, new opportunities in spintronics is enabled by the discovery of ferromagnetic vdW 2D ferromagnetic materials [38–42]. They show promising properties such as sensitive magnetic field control of the ferromagnetic transition temperature [38], antiferromagnetic interlayer coupling [39] and facile integration in vdW heterostructures [156,157]. For spin-based electronic devices, a hard-ferromagnetic metal is highly desired, which is fulfilled by Fe_3GeTe_3 (FGT). Its sizeable magnetic remanence and coercivity along with excellent electronic conductivity enables the observation of nearly rectangle signal in anomalous Hall measurement [40]. Furthermore, while other vdW ferromagnets only work bellow liquid nitrogen temperature, with electrostatic gating, room temperature ferromagnetism has been achieved [42], which promises its strong potential in practical spintronics.

This portion of thesis is concerned with the formation and control of MDW on FGT nanoflake. The major results will be reported in a subsequent publication.

5.2. Probing the orientation of magnetization by anomalous Hall effect

We utilize thickness-dependence of vdW ferromagnets to realize the magnetic domain wall [38,39,42] and probe it with magnetotransport method, which is more relevant to practical

applications comparing with optical characterization methods. Due to the anomalous Hall effect (AHE) [158] in ferromagnetic materials, the transverse resistivity ρ_{xy} is predominately determined by the macroscopic magnetizations M_z. Specifically, the Hall resistivity can be calculated as

$$\rho_{xy} = R_0 H_z + R_s M_z \tag{43}$$

where R_0 and R_s characterize the contributions from ordinary Hall effect (OHE) and AHE, and H_z is the applied magnetic field. As the AHE term is often dominating, the obtained $\rho_{xy}(H_z)$ can be used to infer the trend of $M_z(H_z)$ as well as magnetic coercivity and remanence. While ρ_{xy} is usually antisymmetric in the applied magnetic field, the longitudinal resistivity ρ_{xx}, on the contrary, is generally symmetric. When the current density is uniform in the channel, the measured transverse and longitudinal voltages are directly proportional to the resistivities. In such a scenario, the revisal of transverse voltage corresponds to the flip of the orientation of magnetization.

If an MDW forms between two pairs of voltage probes, as shown in Figure 5.1, they will obtain opposite voltage drops. Consequently, the longitudinal voltage will also be affected by such reversal [159–161]. Moreover, such perturbation disrupts the homogeneous current distribution and corresponds to a circulating current around the DW, which makes opposite contributions to the longitudinal voltages across the DW on two sides of the sample. (Figure 5.1).

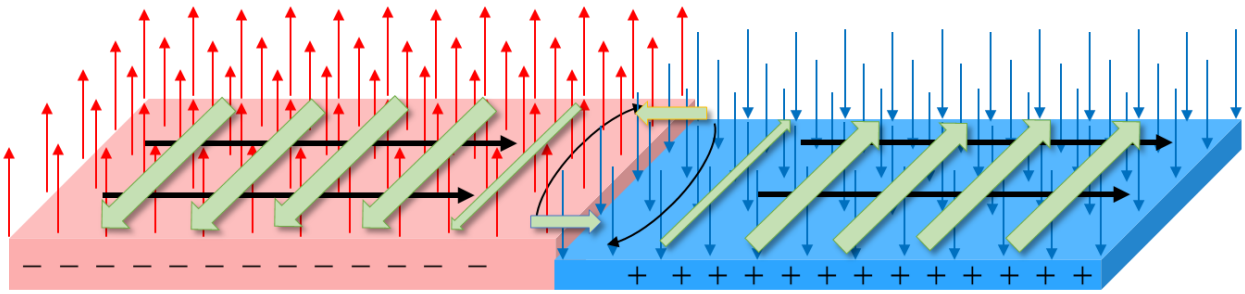

Figure 5.1 | Thickness-step-induced magnetic domain wall formation and its effect on transport properties. The pink and light blue blocks represent two regions of different thickness on a naturally cleaved FGT flake. The vertical arrows manifest the orientation of magnetizations created by ramping the magnetic field between the magnetic coercivities of the two portions. The thick black arrows indicate the driving current. The plus and minus signs denote the sign of charge accumulated on the edge of the flake due to Hall effect. The green arrows represent the induced electric field. The thin green arrows and thin black arrows near the thickness step demonstrate the perturbation of electric field and current due to the magnetic domain wall.

5.3. Device fabrication

To avoid the damage to sample during the lithography and metal deposition process, we fabricate the contact to the nanoflake and pads for wirebonding on SiO_2/Si substrate, before the FGT flakes are transferred onto them [40,162]. First, UV lithography is used to define the patterns (Layer 1) of bonding pads on the substrate, which is followed by depositing 5 nm Ti/100 nm Au by e-beam evaporation and liftoff. Using the alignment markers on L1, we define the pattern for contact electrode (Layer 2) using e-beam lithography to for higher resolution. 5 nm Pt is sputtered

and liftoff afterwards. The predefined electrode can be fabricated in wafer scale and hand cut to small pieces for high throughput.

Our samples are exfoliated from bulk FGT crystals grown by chemical vapor transport method. Nanoflakes with a single thickness step are dry transferred to the premade Hall electrodes by polymer-based method [163]. We carefully align the thickness step into the gap between two pairs of Hall voltage probes. Subsequently, we cover the transferred FGT flake with another layer of hexagonal boron nitride of thickness 10 - 50 nm. The exfoliation and transfer are done in a glovebox with an oxygen level below 0.1 ppm. Before taking out of the glovebox, a thin layer of PMMA is spin-coated on the sample to further protect it from oxidation during wire bonding and sample loading [40]. The full fabrication process is shown in Figure 5.2.

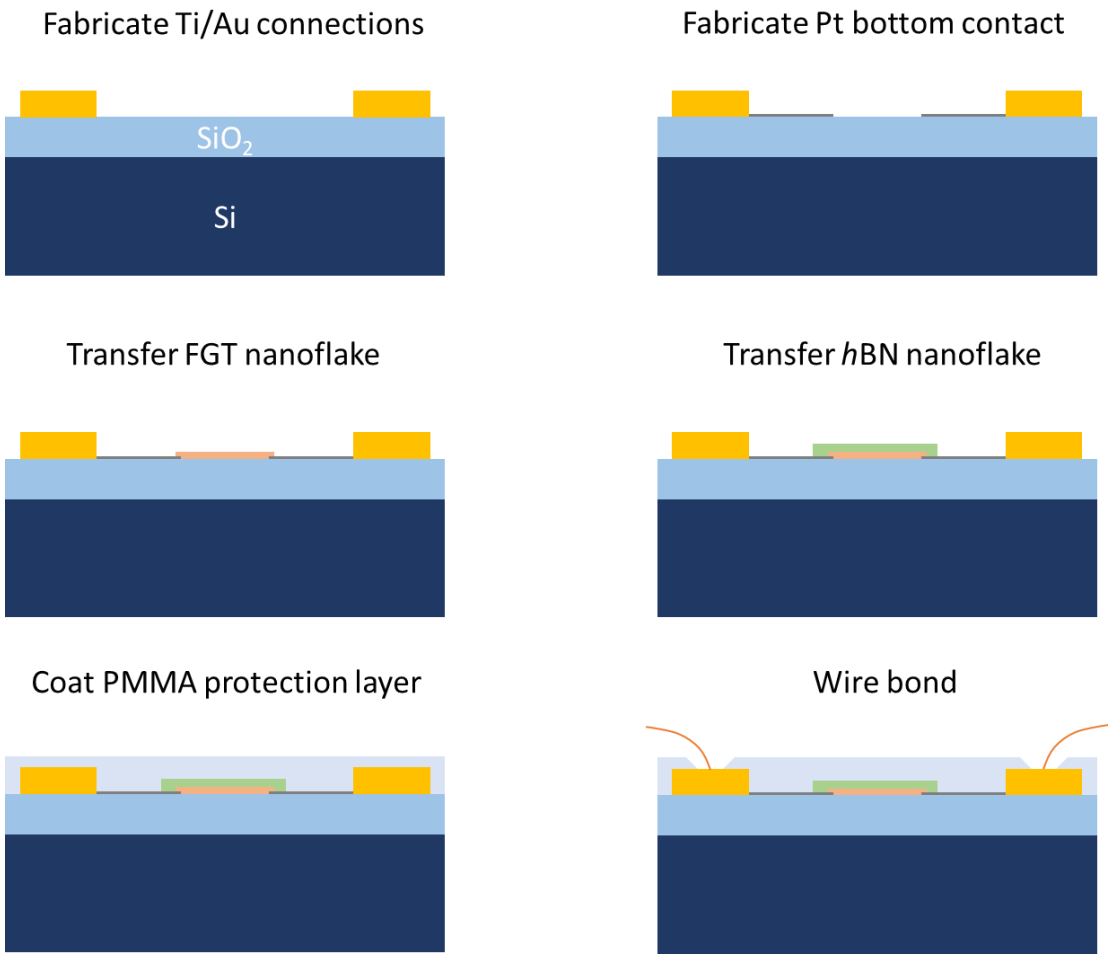

Figure 5.2 | Fabrication procedure for bottom-contact FGT device for Hall effect measurement.

The sample thickness is characterized by atomic force microscope (AFM) after the transport measurement and the removal of the PMMA protection layer. A typical device is shown in Figure 5.3 with a thickness of about 9 (13) nm on the thin (thick) side.

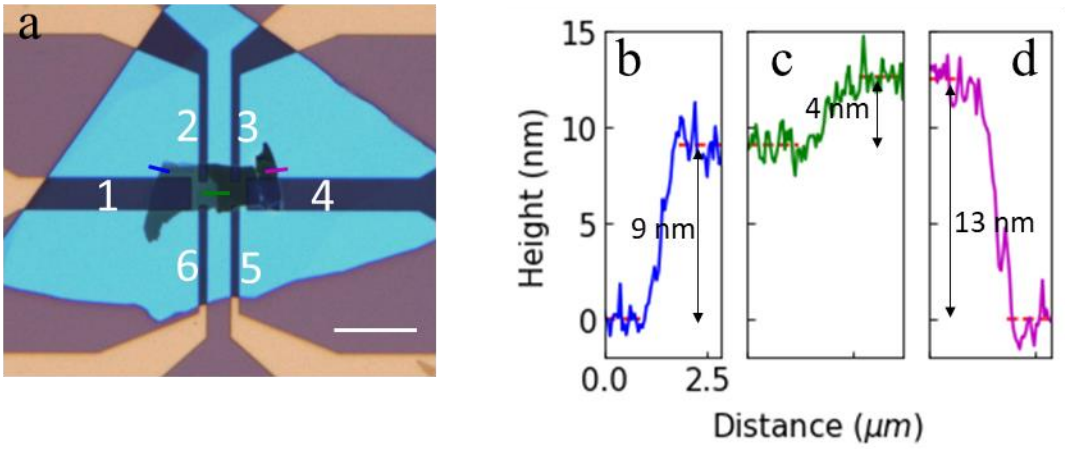

Figure 5.3 | Device for domain wall manipulation

5.4. Magneto transport measurement and results

The samples are measured in a cryostat with a base temperature of 1.8 K. The measurement is done at the base temperature if not explicitly stated. The channel is excited with an AC current of 6.3 Hz. Three lock-in amplifiers are connected between voltage probes 2-3, 6-5, and 2-6 to measure the longitudinal resistances on both edges and transverse resistance simultaneously (Figure 5.4).

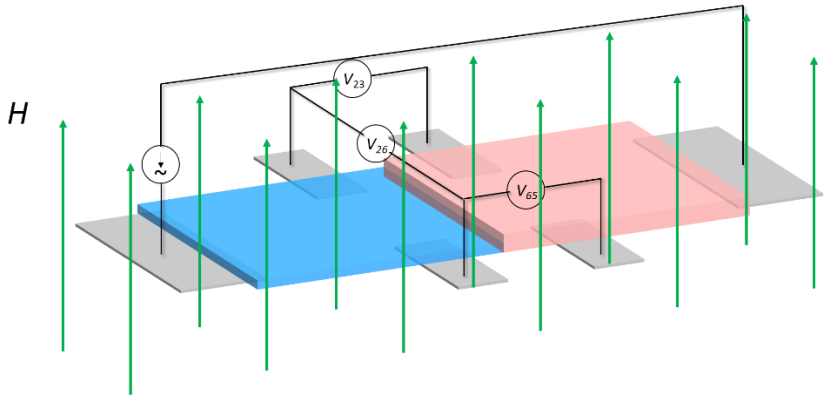

Figure 5.4 | Magnetotransport measurement configuration.

On the contrary to the conventional MRs symmetric in magnetic fields measured on uniform samples, we achieve asymmetric behaviors using our device with the aligned thickness step. During forward sweeping of the magnetic field at 0.4 T, a dip in the MR between probe 2 and 3 can be clearly identified, while a peak appears on backward sweeping of the field at -0.4 T (Figure 5.5 a). Meanwhile, on the other side of the sample, the MR shows the similar features but exactly reversed, i.e. a peak on the forward field and a dip on the backward field (Figure 5.5 b). Clear correspondence is also observed on the Hall resistances (HRs) (Figure 5.5 c). The HRs flip the sign near ±0.4 T, indicating the reversal of magnetization. However, instead of a typical single-step transition, we find two consecutive sharp jumps connected by a plateau unveiling an intermediate magnetization state. Comparing the signals measured at two pairs of Hall electrodes,

the hysteresis loops exhibit a similar trend but with different resistance values at the plateaus. The exact cooccurrence of the anomalies in MR and HR implies their closely-related underline mechanisms.

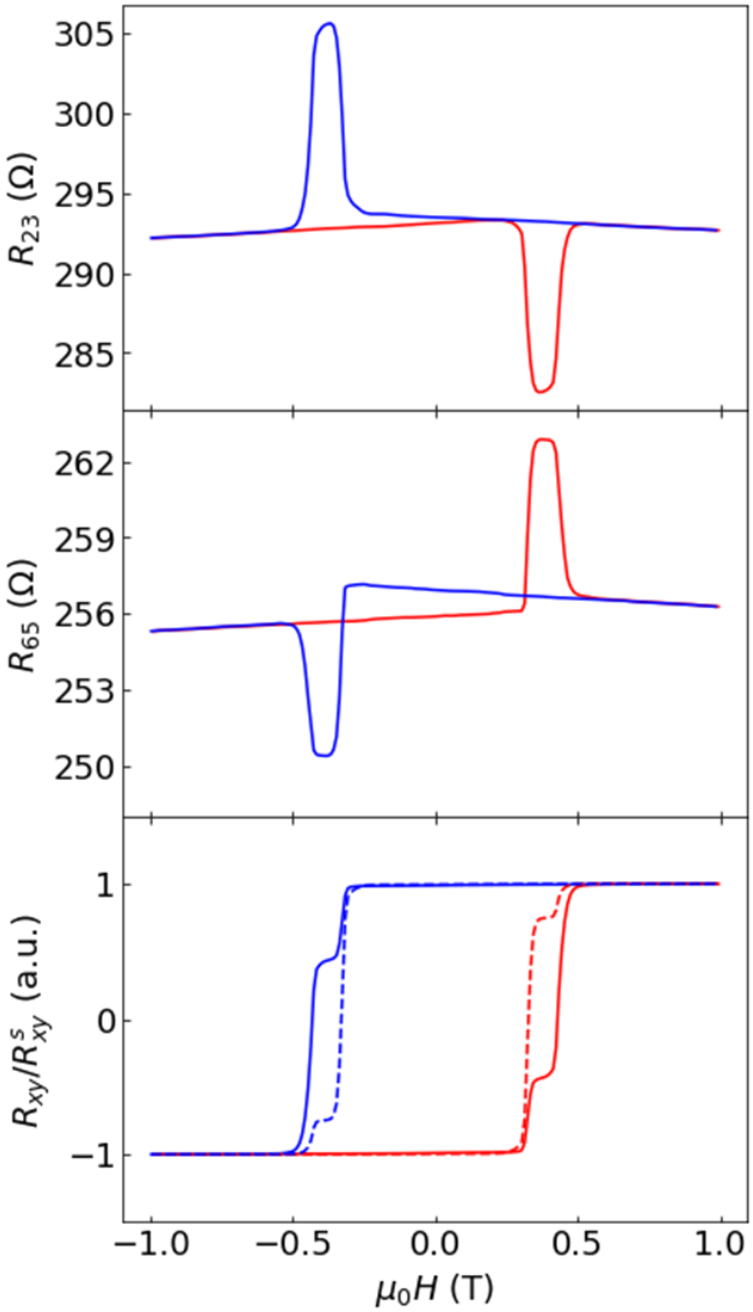

Figure 5.5 | Magneto-transport measurement result. The peaks and dips are due to the formation of MDW at specific range of magnetic field.

To gain more insight into the observed anomaly, we carry out magneto-transport measurements on another two homogenous samples of thickness 8 nm and extract the MRs and HR (Figure 5.6).

The obtained MR follow typical symmetric magnetic field dependence. And the HR features a single sharp step at the coercive fields of 0.56 T.

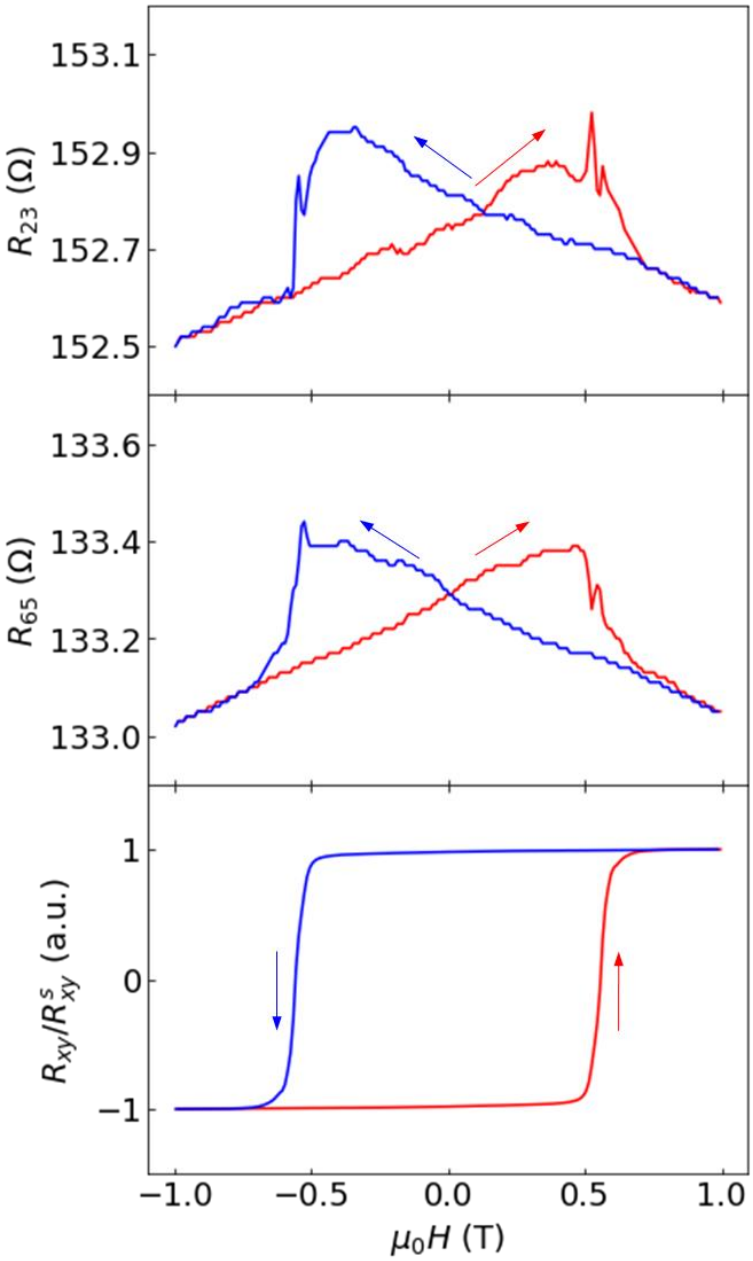

Figure 5.6 | Magneto-transport measurement on a uniform sample with thickness of 8 nm.

Another uniform sample with thickness of 15 nm is also characterized through similar procedure. The asymmetry in the MRs can be explained by the imperfect alignment of the electrode. The obtained coercivity is ~ 0.31 T, smaller than that on the thin uniform sample.

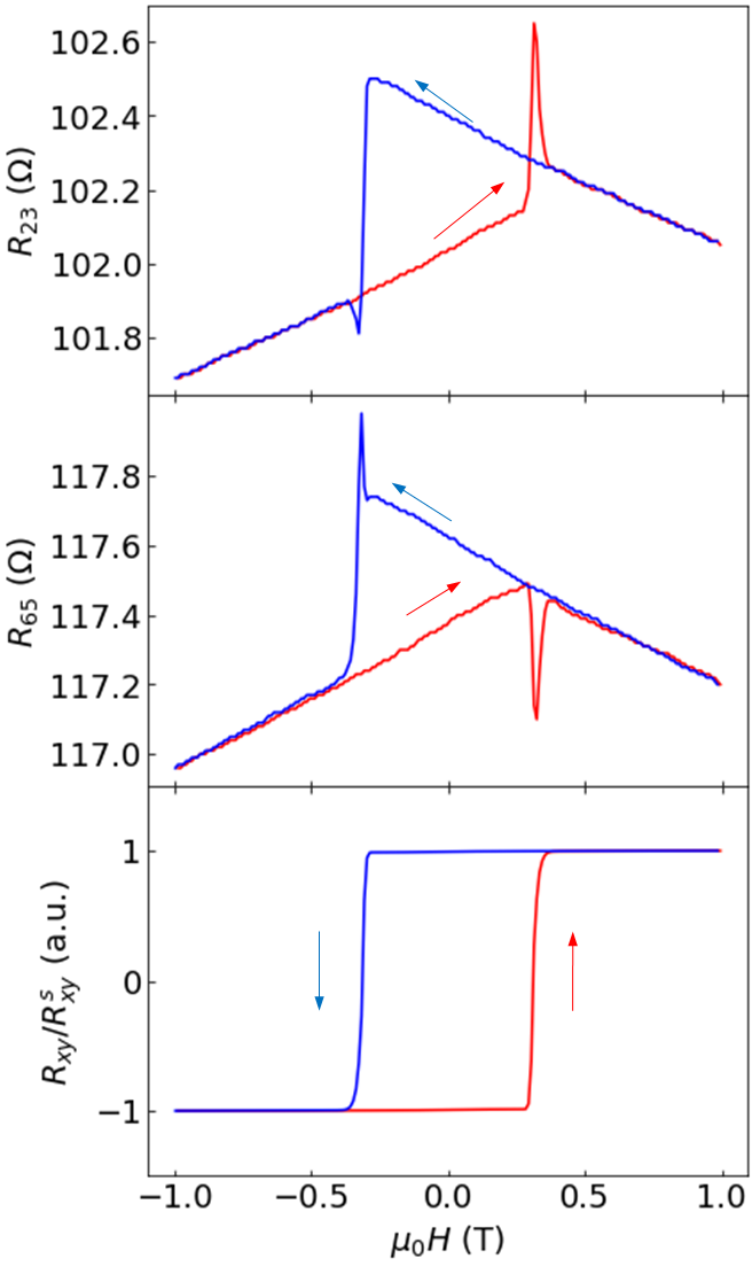

Figure 5.7 | Magneto-transport measurement on a uniform sample with thickness of 15 nm.

5.5. Simulation using measurement results from uniform samples

Comparing the hysteresis loops of the HRs obtained from the uniform samples with different thicknesses, it is expected that opposite magnetizations may appear on those two samples when the external magnetic field is tuned between their magnetic coercivities. Notably, such a range closely matches the anomalous features in Figure 5.5. Using a computational model based on the resistivity data we measured from the homogenous samples, we demonstrate that the transport anomaly results from the thickness-dependent coercivity [159,161]. A channel is assumed to be infinitely long in the x-direction and locate in [0, w] along the y-direction. The resistivities of the

thick and thin homogenous samples are assigned for the regions of x < 0 and x > 0 as functions of the external magnetic field. The voltage distribution $V(x, y)$ can be calculated by solving its Laplace's equation with appropriate boundary conditions. To the first order of the Hall resistivity difference, we have [159]

$$V(x,y) = -Jx\rho_{xxi} + V_T(x,y) \quad i = 1 \text{ for } x \le 0 \text{ otherwise } 2 \tag{44}$$

where the transverse voltage V_T is introduced to emphasize the effect of a DW and can be calculated by

$$V_T(x,y) = \begin{cases} \Delta V + Jy\rho_{xy1} - \dfrac{4\gamma\rho_{xx1}wJ}{\pi^2}\sum\limits_{m\ \text{odd}}\dfrac{1}{m^2}\exp\left(\dfrac{m\pi x}{w}\right)\left(\cos\dfrac{m\pi y}{w} + \beta_1\sin\dfrac{m\pi y}{w}\right) & x \le 0 \\ -\Delta V + Jy\rho_{xy2} + \dfrac{4\gamma\rho_{xx2}wJ}{\pi^2}\sum\limits_{m\ \text{odd}}\dfrac{1}{m^2}\exp\left(-\dfrac{m\pi x}{w}\right)\left(\cos\dfrac{m\pi y}{w} - \beta_2\sin\dfrac{m\pi y}{w}\right) & x > 0 \end{cases}$$

$$\Delta V = \frac{wJ}{4}\gamma\left(\rho_{xx1} + \rho_{xx2}\right) \tag{45}$$

and

$$\beta_i = -\frac{\rho_{xyi}}{\rho_{xxi}}, \gamma = \frac{\rho_{xy2} - \rho_{xy1}}{\rho_{xx1} + \rho_{xy2}} \tag{46}$$

At $\mu_0 H$ = 0.4 T during forwarding sweeping of magnetic field, the magnetization is reversed only on the left half (Figure 5.8). V_T is significantly modified around the DW.

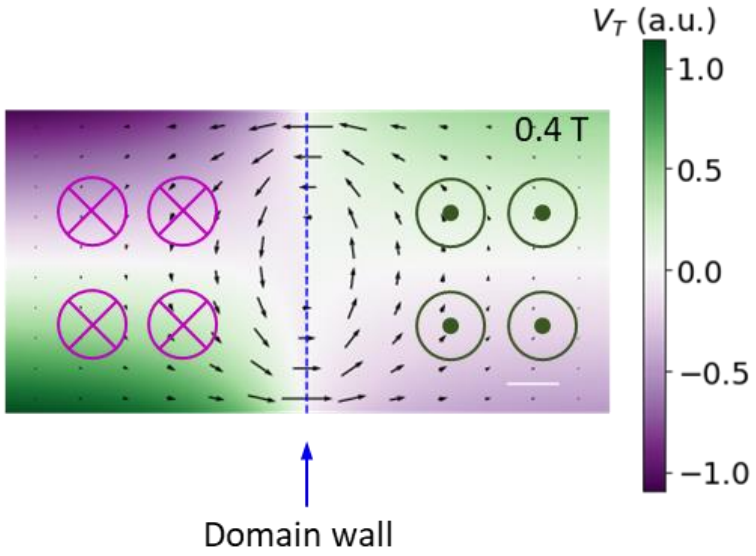

Figure 5.8 | Calculated transverse voltage, magnetization orientation and perturbation current.

We further calculate the MRs and HRs (Figure 5.9) by evaluating V(x, y) at the positions of voltage probes on our sample. The calculation result qualitatively reproduces our experimental

data measured on the stepped sample, which justifies that the anomalous magneto-transport corresponds to an MDW along the thickness step. The discrepancy in exact values may come from the differences in resistivities (due to unmatched thicknesses) and geometry.

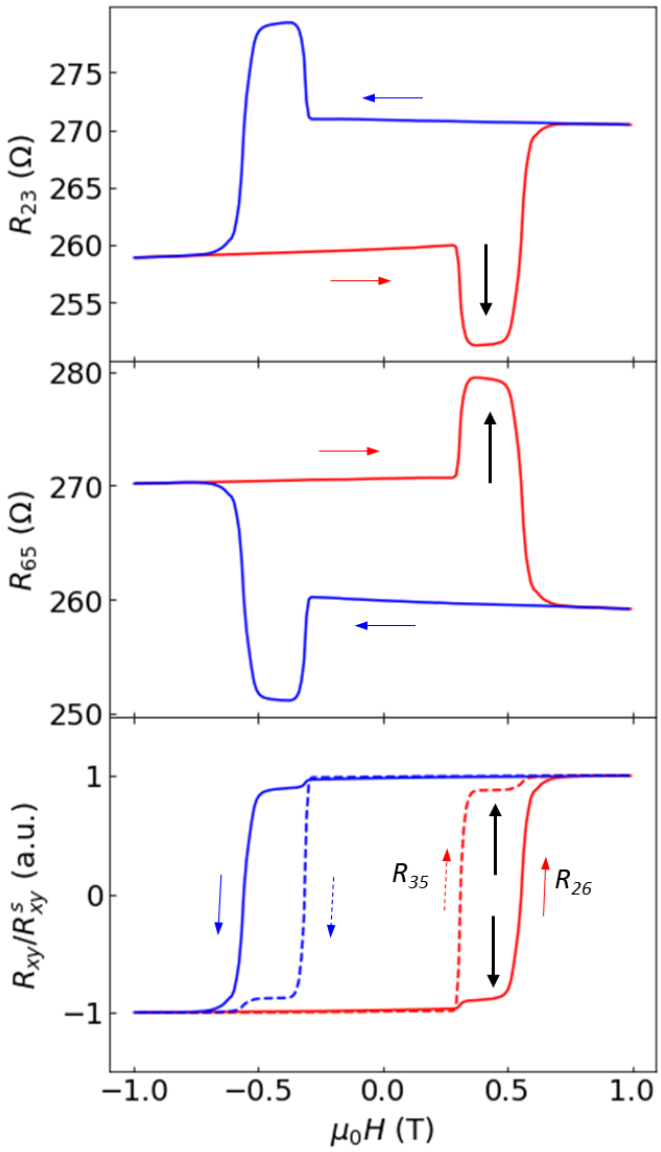

Figure 5.9 | Hall resistance and magneto resistance calculated from experimentally measured resistivities of uniform samples with similar thickness. The black arrows denote the data point on the curves corresponding to the domain wall regime shown in Figure 5.8.

The perturbation current distribution can be further calculated as

$$j_x = J\sum_{m\ \mathrm{odd}} \frac{4\gamma}{n\pi}\exp\left(-\frac{n\pi|x|}{w}\right)\cos\left(\frac{n\pi y}{w}\right)$$
$$j_y = -J\sum_{m\ \mathrm{odd}} \frac{4\gamma}{n\pi}\exp\left(-\frac{n\pi|x|}{w}\right)\sin\left(\frac{n\pi y}{w}\right) \quad (47)$$

which corresponds to a circulating current around the domain wall (arrows in Figure 5.8). The reversal of V_T is mediated by a longitudinal perturbation current across the MDW near the side edges of the channel. The reduced transverse electric field allows a transverse current, which completes a closed circulation. As a result, the sign of transport anomaly reflects the direction of the circulating current.

Interestingly, on increasing the temperature, we observe the reversal of the anomalous features. As shown in Figure 5.10, two temperature regimes can be identified. Below 30 K, The MR anomaly is monotonically weakened on temperature increase, and finally vanishes around 30 K. On further increasing the temperature, the anomaly revives but with opposite signs, corresponding to revert of the circulating current.

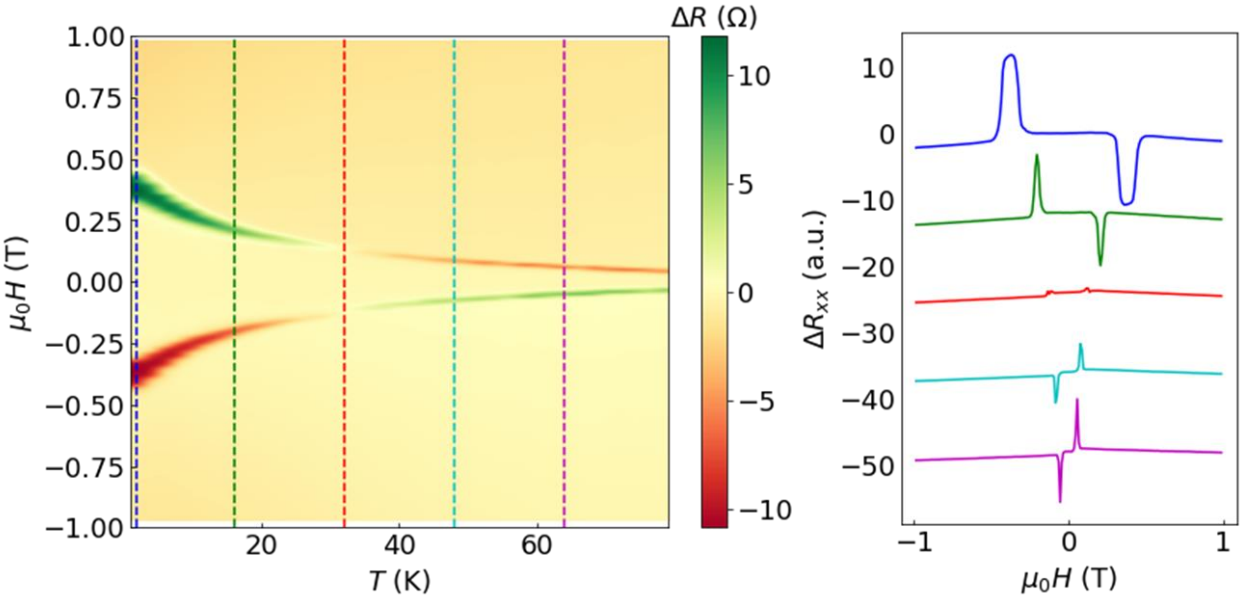

Figure 5.10 | Temperature dependence of the magneto resistance change.

Such a sign flip reveals a crossover of magnetic coercivities of different crystal as the temperature rises, which we also verified on uniform samples (Figure 5.11 error bars). The temperature dependence of coercivity we exploit here provides insight into the sharp contrast in magnetic properties of the few-layer and bulk FGT crystals. We analyze our data with a model commonly used for thin film coercivity [164]. Considering the domain wall pinned at magnetic impurities, it predicts temperature-dependent coercivities $H_c^{1/2} = H_{c0}^{1/2}\left(1-\left(T/T_0\right)^{2/3}\right)$ where H_{c0} and T_0 are the zero-temperature coercivity and the characteristic temperature. Such a model fits

our data reasonably well at low temperature, with different values for H_{c0} and T_0 for the thick and thin samples (Figure 5.11 solid curves). We note that H_{c0} is proportional to the bulk impurity density, which inversely scales with thickness if the surface impurities dominate. Meanwhile, it has been reported that thinner vdW samples suffer more from thermal fluctuation and show lower characteristic temperature [38], consistent with the lower T_0 of the thinner sample in our experiments. The similar thickness and temperature dependences of coercivity have been reported on Fe film [165] and particles [166], which also attribute the importance of surface layers. As the thickness decrease, such pinning effect from surface layer prevails, which may cause the harden of ferromagnetism in FGT crystal from the thick to few-layer flakes.

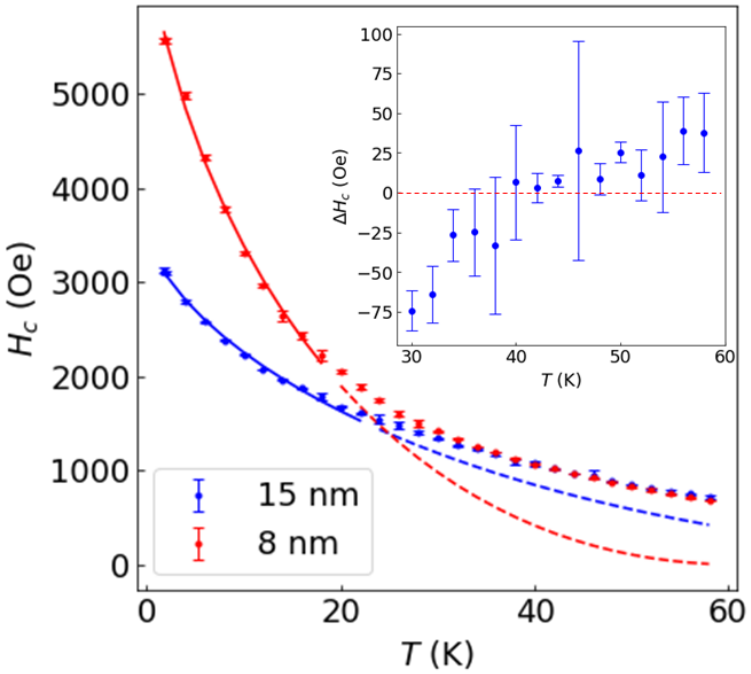

Figure 5.11 | Temperature dependence of coercivities on the 8 nm and 15 nm uniform flakes. The coercivity difference is plotted in inset to show clear cross over. The data in main panel is fitted with Gaunt model up to 18 K (solid lines), with $H_{c0,\,\mathrm{thick}}$ = 3545 ± 17 Oe, $T_{0,\,\mathrm{thick}}$ = 109 ± 2 K for the thick flake and $H_{c0,\,\mathrm{thin}}$ = 6901 ± 47 Oe, $T_{0,\,\mathrm{thin}}$ = 61 ± 1 K for the thin flake. The measurement at higher temperature deviates from the model fitting results, which is also previously reported in similar material system [165].

5.6. Conclusion

In conclusion, we discovered anomalous MR and HR arising from circulating current around domain wall in a few-layer vdW magnet. Such behavior can be further modified by temperature. Our finding provides a unique method to control the ferromagnetism in vdW material. It also paves the way to topological physics in vdW heterostructures and their applications in MDW-based spintronics.

Chapter 6 Control ion transport through sub-nanometer 2D channels

6.1. Background

The fluidics in nanoscale is fundamental to many disciplines, such as physiology, membrane science, bioengineering and surface science [167]. Thanks to the advances in nanofabrication and material synthesis, various nanofluidic channels, especially nanopores [168–170] and nanotubes [171–175], have been created for understanding the fluid transport in nanoscale environment, which is relevant to many natural materials and processes that is crucial to human life [167,176–178]. Specifically, unconventional transport phenomena have been observed from water and ions under such confined structures [167,179].

The layered vdW materials are weakly bonded in the out-of-plane direction. The weak interlayer bond allows the isolation of individual atomic planes by mechanical exfoliation and chemical intercalation, which leads to the discovery of the exciting phenomena that is specific to 2D confined systems [180–183]. Furthermore, the void between the crystal planes also features an atomic-scale thickness, promising to be used for exerting confinement to other systems, such as molecules and ions. Under such tight confinement, the reorganized water molecules exhibit reduced dielectric permittivity [184,185] and may form a room-temperature ice phase [186]. The transport of water and ions are also modified by the direct interactions to the channel walls [187], which can be further modulated by manipulating the property of wall materials [188].

The reduced graphene oxide (rGO) nanoflake is attractive for several appealing advantages. Its layer spacing is tunable to angstrom-level precision by controlling the annealing temperature and time [189], which allows tunable permeation of molecules [189] and ions [190]. In contrast to graphene oxide (GO), which is an insulator, rGO shows orders-of-magnitude improved electric conductivity [191], which is important for electrical control. With careful material preparation, individual flakes with size > 100 μm can be obtained, which facilitating further fabrication and characterization. Thus, it is a promising platform for study the electrically tunable ion transport in ion-size scale 2D confined channels. In this chapter, I present our study on the voltage-controlled ion transport through such channels, which will appear in a subsequent publication.

6.2. Modulation principle

In aqueous solution, the interaction between water molecules and ions results in the formation of hydration shell around the ions. Inside the bulk solution, the increased radius lowers the mobility of ions [192]. Moreover, when the size of the fluidic channel is comparable to the hydration radius, strong interaction arises between the ions and the wall of the channel. Usually, that leads to steric impedance for the ions to enter such tightly confined channels [193]. However, the hydration shell may be squeezed or removed if additional energy is supplied. In biological ion channels, the dehydration energy is compensated by the electronic interaction between the ions and the charged atoms on the channel wall, which plays an essential role for the ion selectivity [194,195]. Furthermore, the tight confinement allows strong interaction between the individual ions. In biological ion channels, the repulsion between the ions lead to a fast and concerted motion: each

in-coming ion knocks at the ion chain inside the channel, push them move forward coherently, which explains the observed diffusion-limited high-efficiency ion conductance [196].

We use the rGO flakes to study the ion transport through the sub-nanometer channels. The interlayer spacing of rGO is comparable to the hydration shell diameter for common metallic ions (~ 0.6 nm for K^+), which may impede the hydrated ions to enter the interlayer spacing. By applying electric gate voltage with respect to the ionic solution, the potential barrier from dehydration energy may be reduced by the electrostatic potential, as happened in the biological ion channels. Furthermore, with a large gate voltage, the charge density on the atomic layers can be increased, so as the ion density inside the 2D channels. Consequently, we expect higher ion conductance as the gate voltage increases.

6.3. Device structure and fabrication

Our nanofluidic channels are realized using a single rGO flake to prevent the flow through the large gaps between individual flakes. The rGO flake is placed on a suspended low stress nitride (LSN) membrane. A hole is opened through the LSN film and the GO flake as the entrance for ions and molecules into the interlayer channels. On top of GO, the hole is sealed by 5 nm Ti/80 nm Au/10 nm Ti/ 80 nm SiO_x. The metal layer is used to provide electric contact to the rGO flake. And the SiO_x layer block the top surface of the metal from the water solution to reduce the electric current between them. A schematic for the device structure is shown in Figure 6.1.

To realize such device, we first fabricate the suspended LSN films with a hole. The LSN is deposited on double polished (100) silicon substrate using low pressure chemical vapor deposition. We pattern the membrane region and the hole on each side of the LSN film with UV lithography and reactive ion etch (RIE). Backside alignment is used to align the hole pattern on one side to the etch window for the membrane region on the other side. When we etch the pattern on one side, the other side is protected by a silicon wafer bonded with cool grease to avoid undesired damage. After removing photoresist by acetone/IPA/DI water, the wafer is dipped into 24% (weight/volume) KOH solution at 80 °C for anisotropic etch with a etch rate ~ 1.36 μm/min (100 direction). When the silicon layer is etched through, it is rinsed in DI water and dry. Finally, it is cleaved into square chips of size 15 mm × 15 mm, ready for the rGO flake transfer.

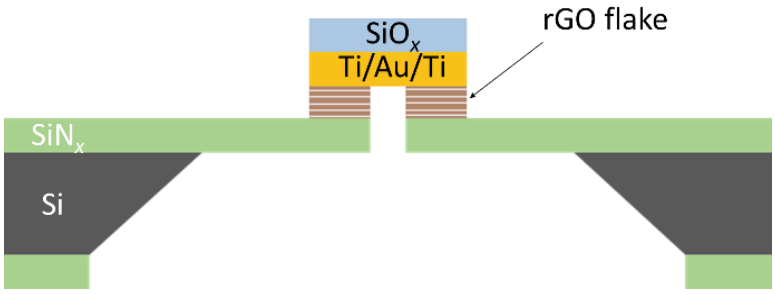

Figure 6.1 | Schematic of the electrically tunable nanoscale 2D ion channel in reduced graphene oxide.

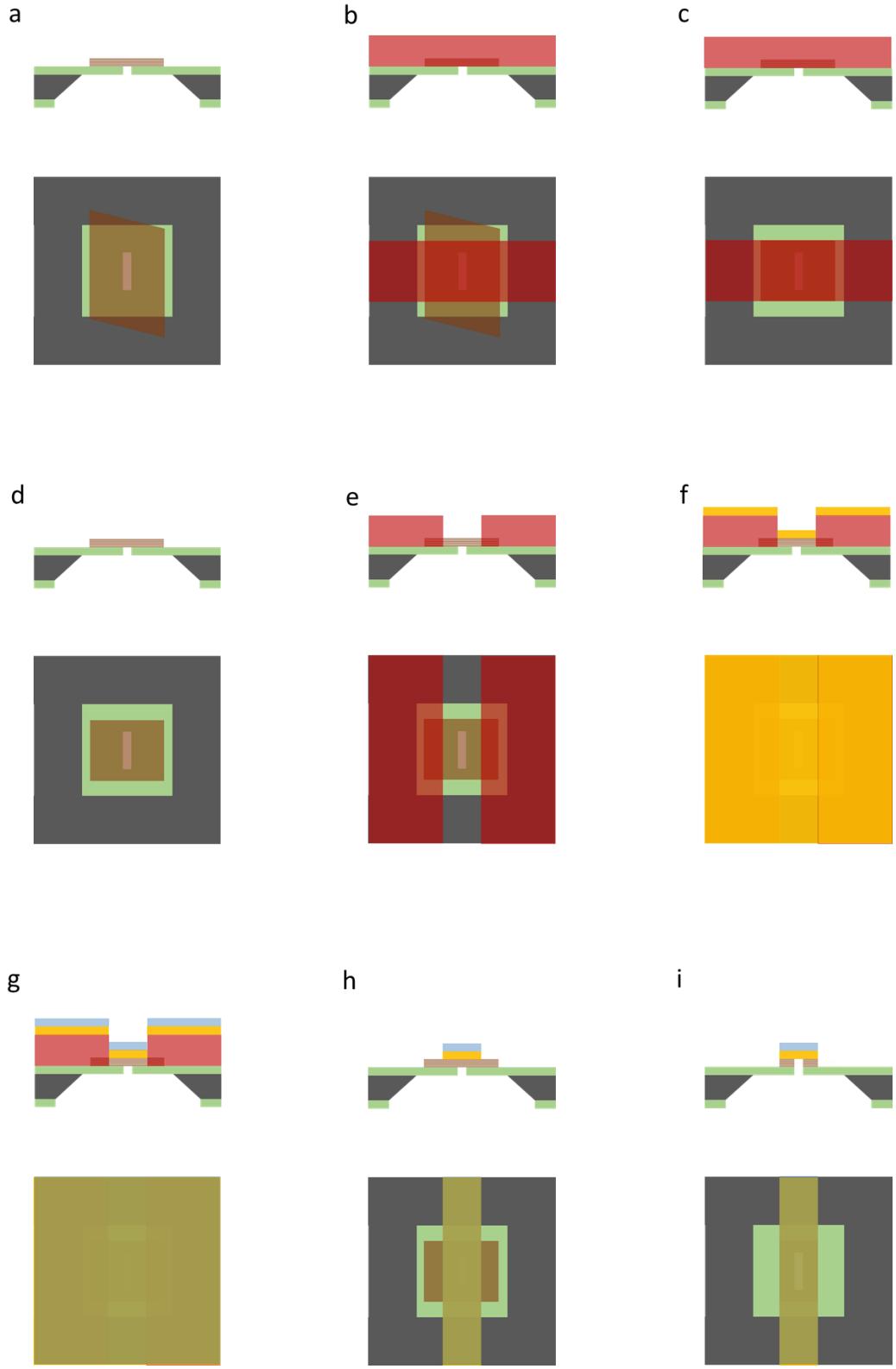

Figure 6.2 | Fabrication procedure of the tunable ion channel device.

To obtain individual rGO flakes, we first prepare GO flakes following the modified Hummer method [197]. The resulted GO suspension is drop-casted on silicon chips and dry. We reduce the GO flakes by heating them in N_2 atmosphere. Afterwards, the desired flakes are transferred to the hole on the suspended LSN film.

The as-transferred rGO flake is usually in an irregular shape. To obtain a regular shape and facilitate modeling, we first cut the extra portion of the rGO flake along the hole direction as shown in Figure 6.2b. We define a strip across the chip using UV lithography. Then the chip is etched with O_2 plasma (Figure 6.2c), which not only removes the excessive region of the flake, but also clean other flakes and residues generated during the transfer process, facilitating the following fabrication steps.

After the photoresist is removed by acetone/IPA/DI water (Figure 6.2d), another UV lithography is used to define the pattern for the electrode/insulator stack (Figure 6.2e). The metal layers and the SiO_x are deposited by e-beam evaporation (Figure 6.2f) and RF sputtering (Figure 6.2g), respectively. Subsequently the film is lifted off in acetone at room temperature and rinsed in IPA and DI water (Figure 6.2h).

Finally, O_2 plasma is applied to the top and bottom sides of the chip (Figure 6.2i) to remove the rGO region extended out of the electrode and in the hole. In this way, the pattern on the rGO flake is automatically aligned with the boundaries of the electrode and hole. The microscope images of a fabricated device from the top and bottom sides are shown in Figure 6.3.

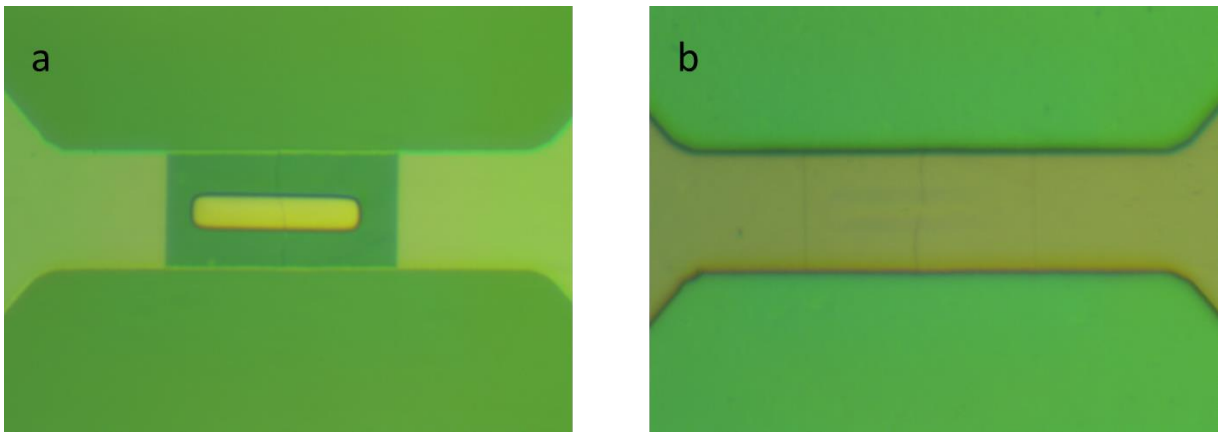

Figure 6.3 | Microscope images of a fabricated device. a Top view. b Bottom view.

6.4. Ion transport measurement and results

The ion transport is measured with a diffusion cell shown in Figure 6.4. The chip is clamped between two reservoirs. Reservoir A is filled with water solutions in which the ions to be detected have high concentration. The solution in Reservoir B, on the contrary, doesn't contain those ions initially. Thus, the transport of the ions through the rGO ion channel can be detected by measuring the ion concentration change inside Reservoir B. Using ICP-MS, the ion concentration can be measured with high sensitivity, critical for resolve the small ion flow limited by the nanometer

scale ion channels. The electric gate voltage is applied between the rGO as work electrode and a platinum counter electrode. The electrical potential between the rGO flake and the solution is monitored by a Ag/AgCl reference electrode. 3 M NH_4Cl is added to both sides to obtain high electric conductivity of the solution, which is important for potential measurement. To measure a pure diffusing-driven flow, we ensure the electric potential is equal between the two reservoirs by using a salt bridge (not draw on the schematic).

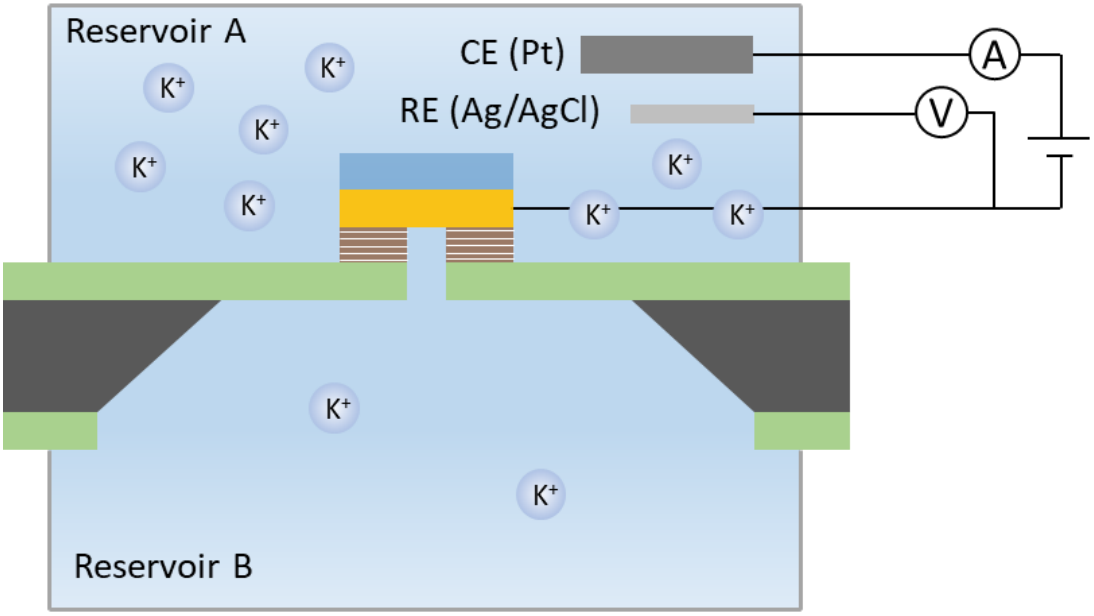

Figure 6.4 | Schematic of the ion transport measurement setup.

The ion transport in our device shows clear voltage dependence. Figure 6.5 plot the K^+ ion concentration in reservoir B measured at a sequential of time while various voltages are applied to the rGO flake. The vertical axis is normalized with the cross-section area of the channel. Small concentration change is observed without voltage applied, which may due to conventional diffusion and is used as background subtracted from all data. For voltages smaller than -0.8 V, no voltage-dependent transport is observed. However, as the voltage is increased beyond -1.0 V voltage dependent, the concentration change becomes faster, indicating a large permeation flux.

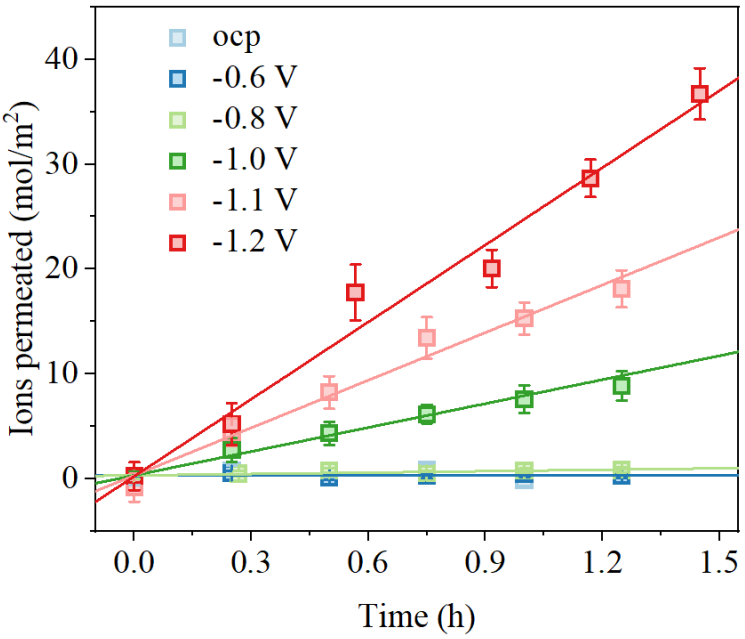

Figure 6.5 | Ion permeation at various gate voltages.

To better illustrate the threshold behavior, we extract the permeation rate at different voltage from the slope of the temporal ion concentration evolution. Starting at -1.0 V, the permeation rate approximately follows a linear relation with the applied voltage (Figure 6.6). Strikingly, at -1.2 V, the effective diffusion constant is calculated to be ~ 2×10^{-7} m^2/s, which is about 2 order higher than the value in bulk water. For the voltages less than -0.8 V, the permeation rate remines virtually constant. Yet it doesn't show voltage dependence before -0.8 V.

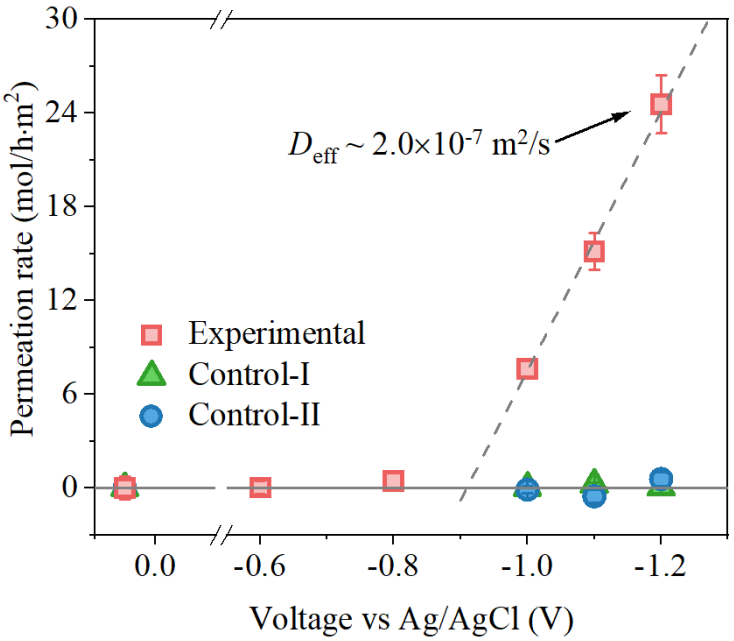

Figure 6.6 | Voltage dependent permeation rate.

We also measured two control devices to verify the voltage-controlled ion transport is resulted from our unique device structure (Figure 6.6). In one device (Control-I) we use a graphite nanoflake whose interlayer spacing is even smaller than the rGO. In the other device (Control-II) we keep the rGO inside the hole unetched, thus the channels are not open to the solution. No significant permeation is observed with both devices, which proves the unique channel structure of our device is critical for the voltage-controlled ion transport.

The voltage-controlled ion channel is stable over voltage cycling. The fast ion transport can be turned off when the applied voltage is withdrawn, as shown in Figure 6.7. Once the voltage is re-applied, fast ion transport is resumed to the original permeation rate. The repeatability proves that the increased ion permeation rate at high gate voltage is not caused by leaking due to structure damage. Instead, a reversible process is responsible for the observed phenomenon.

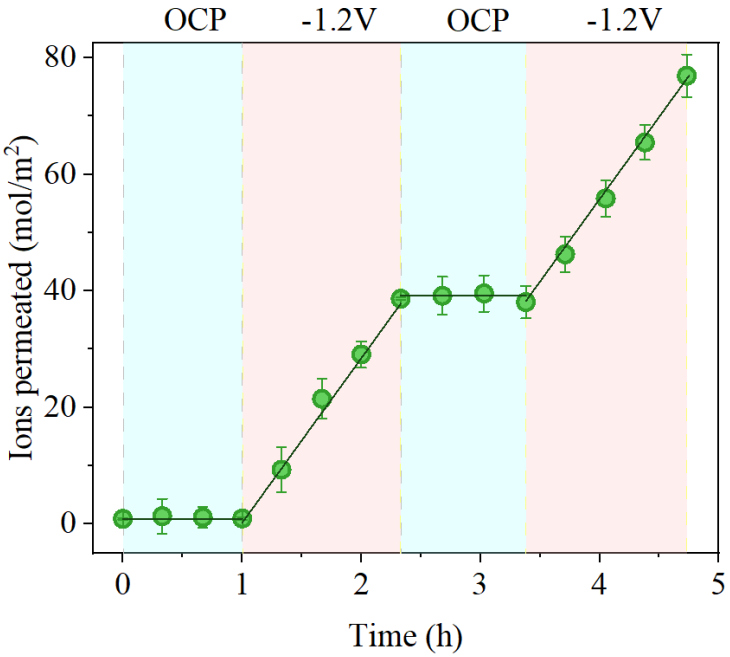

Figure 6.7 | Repeatable voltage control of ion transport.

To demonstrate the potential of using rGO channel for ion separation, we further measure the permeation rates of multiple ions, including Li^+, K^+ and Cs^+ (Figure 6.8). All the ions are filled into Reservoir A and their concentrations in Reservoir B are measured simultaneously. We find the permeation rates are ordered as $K^+ > Cs^{2+} > Li^+$ for all the three gate voltages. On one hand, hydration radii are ordered as $Li^+ > K^+ > Cs^+$, which leads to smaller flux for Li^+ ion. On the other hand, the bare ion radii are ordered as $Cs^+ > K^+ > Li^+$, which results in slower transport of Cs^+. The combined effect favors the transport of K^+ ion, which is similar to the selective permeation in biological ion channels. A large selectivity ~ 9:1 is observed at -1.0 V, which is promising for ion-sieving applications.

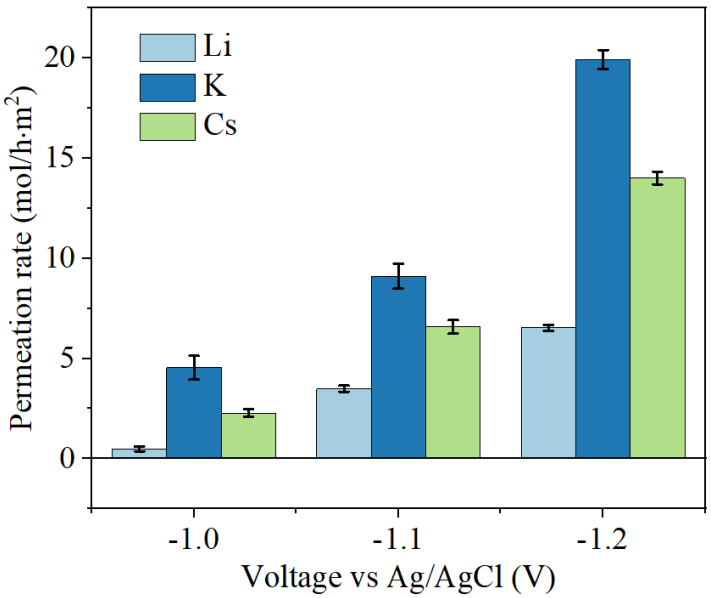

Figure 6.8 | Comparison of permeation rates of different ions at various voltages.

6.5. Conclusion

The sub-nanometer 2D fluid channel in rGO exerts tight confinement on the motion of hydrated ions. Strong interaction is generated between the carbon atomic sheets and the ions, and between the individual ions. Modulation of the electric potential between the rGO flake and the solution results in manipulation of the dehydration process and the ion density inside the tightly confined channels, which is manifested as a voltage-controlled ion transport. Furthermore, when a large negative voltage is applied to the rGO flake, fast ion transport is observed, with effective diffusion constant even two order higher than in the bulk water, possibly due to the combined effect from strong dehydration and coherent motion of ions, which mimics the biological ion channel but in a 2D fashion. The voltage-controlled fast transport of ions in the sub-nanometer scale 2D channels opens new possibilities for material isolation and artificial ion channel. It also provides a platform to explore new material phase and chemical reaction in a tightly confined space.

Chapter 7 Summary and outlook

Two dimensional materials and systems bring exotic properties and unprecedented advantages. Intrinsically, the reduced dimension results in unique density of states in their electronic structure and anisotropic response to external electric and magnetic fields. Extrinsically, the planar structure facilitates a wide range of tuning mechanisms, which is critical to tailor the material properties for specific applications. Substantiate progress has been achieved on 2D materials and systems, especially in the last 15 years due to the rise of graphene and other vdW layered materials. The development of high-quality and large-scale synthesis, considerable improvement on fabrication and innovation on material and device characterization lead to numerous breakthroughs in fundamental research and practical applications.

In this dissertation, I show that tuning the optical, electrical as well as mechanical properties of various 2D material systems, by manipulating the carrier density and applying electric and magnetic field, which results in outstanding performance for several important topics.

With innovative optic and electric design, we experimentally demonstrated high performance optical modulators using the wideband absorption in graphene tunable by carrier density. By placing the graphene sheets into a planner structure, we achieved better quality and yield of fabrication, as well as mechanical and thermal stability of the device. Besides, the demonstration with amorphous silicon waveguide indicates the modulator to be fabricated on any dielectric surface, which significantly increases the flexibility for integration with other optical and electronic devices. With a graphene-loaded structure, we achieved an operation speed of 35 GHz. We also demonstrated temperature insensitive modulation properties. To further improve the device performance, we designed and experimentally demonstrated a graphene-centered modulator structure. From numerical simulation, we obtained a large absorption coefficient ~ 0.4 dB/μm for the waveguide mode. With novel fabrication techniques, we realized such device experimentally, and obtained a modulation depth of ~ 5 dB, which is more than twice increases comparing with the previous designs. Our results may bring new possibilities for the realization of compact ultrafast wide-band optical modulators that is stable upon temperature drift and extreme conditions.

Besides carrier density, electric field can also be a turning knob for controlling light matter interaction. Towards this direction, we demonstrate a giant Stark shift of single photon energy at room temperature using the color centers in *h*BN, a vdW layered wide bandgap insulator. Thanks to the advanced nanofabrication technologies, we successfully realized well-shaped nanoscale electrode precisely aligned to the color centers. Such devices allow the application of unprecedented electric field, on the order of 0.1 V/nm, to the single photon emitter, resulted in the observed giant shift. Furthermore, we characterized the angle-resolved Stark effect, which explicitly proves the broken inversion symmetry in the color center emitter. The giant room temperature Stark shift and the crucial information on the structural symmetry of the color center may bring new opportunity to realize room temperature quantum communication and computation system based on vdW materials and their heterostructures.

Comparing to electric field, a magnetic field not only shifts and splits electronic levels, but also adds topological properties to the electronic system, enabling the formation of edge states. Based on this, we experimentally achieved a high-frequency kink magnetoplasmons (KMPs) at a topological edge in a 2DEG system hosted at an AlGaAs/GaAs heterojunction. Such an edge arises from the change in band structure topology, which is induced by a magnetic field of opposite orientations. Compared to traditional method of generating topological states along the physical edge of the 2DEG system, our approach brings the magnetic field distribution as a new designing degree of freedom, which can be useful for developing reconfigurable integrated topological circuits.

A magnetic domain wall can be used to generate the magnetic field required for the formation of the aforementioned topological edge. By utilizing the thickness-dependent magnetic coercivity, we have demonstrated the creation and manipulation of domain wall in a few layer vdW ferromagnetic metal Fe_2GeTe_3. From magneto-transport measurement, we discovered an asymmetric magnetoresistance and multi-value Hall resistance due to the formation of magnetic domain wall. Based on theoretical calculation, we also unveil a circulating current that mediates the electric potential perturbation around it. Furthermore, we achieved temperature control of the chirality of the circulating current, based on the cross-over of temperature-dependent magnetic coercivity on samples of different thicknesses. Our findings demonstrate an effective method to control the ferromagnetism in vdW materials and their heterostructures. It also paves the way to explore topological physics and developing spintronics devices using vdW using vdW material platform.

Beyond the electric and magnetic properties, 2D materials are also promising for novel tunable mechanics. Specifically, sub-nanometer fluid channels can be realized using the interlayer spacing of the vdW layered materials, where the fluid-solid interaction is strengthened due to the tight confinement. We experimentally studied ion transport through the interlayer spacing in individual reduced graphene oxide nanoflakes, controlled by the gate voltage applied between the solution and the rGO flake. The turnability can be explained by a voltage-dependent dehydration process and modulation of ion concentration inside the channel due to charging effect. Strikingly, at large gate voltage, an ultrafast ion transport is achieved, with an effective diffusion coefficient even orders higher than the value in bulk water. We demonstrated the interlayer spacing in rGO as an appealing tool for study the solid-ion and ion-ion interaction in 2D confined channels. It also provides a platform to explore new material phase and chemical reaction in a tightly confined space.

A logical next step will be further exploration in the hybridized turnabilities. On one hand, multiple tuning knobs can be combined to enrich the functionality. For example, as has been shown in this dissertation, the kink magnetoplasmons can be tuned by both the magnetic field and electron concentration. While the magnetic field is patterned, the electron concentration is homogenously controlled. It will be interesting to see the how the boundary in magnetic field and that of the electron density interact, especially in a reconfigurable way. Similar situation also exists in bilayer and trilayer graphene, whose band structure can be modified by an electric field perpendicular to the atomic planes, and band filling is controlled by the carrier density. On the other hand, the tunability in heterostructures of 2D systems brings new possibilities. The tunable Fermi level of graphene may affect the charging state of near-by system, which can be used to tune the single photon emitters hosted by 2D materials. Also, the hard-ferromagnetic domains in FGT controllable

by external magnetic field and temperature can be a critical component to introduce topological effect to other 2D systems.

In a more practical perspective, the scalability plays essential role for real-life applications. Although wafer-scale production of, for example, single crystal graphene, has been reported, how they change the performance and yield of practical electronic and optoelectronic devices still deserves further investigation. The traditional scalable transfer lithography and etching process introduce defects and impurities, significantly impact the tunability of the devices. The state-of-the-art method to prevent those degradation is using exfoliated *h*BN as protection layer, which is difficult to scale up. Thus, innovations in clean yet scalable fabrication technologies will speed up those real-life applications of tunable 2D materials and systems.

The past decade has seen exciting and rapid progress in 2D materials, including the discovery of new material systems, breakthrough in material synthesis, characterization and fabrication as well as innovation in the application of individual materials and their heterostructures. Compared with traditional 3D bulk material, the great tunability enabled by the planar structure is a major advantage of the 2D materials and systems, which may bring unprecedented opportunities to solve the grand challenges in information science, energy, health and environment. It's a great honor for me to contribute in some of the most encouraging discoveries. Yet there are more puzzles and challenges to solve and overcome, which may change the way we think and live!

Bibliography

1. S. L. Chuang, *Physics of Photonic Devices* (John Wiley & Sons, 2012).
2. T. Ando, A. B. Fowler, and F. Stern, "Electronic properties of two-dimensional systems," Rev. Mod. Phys. **54**, 437–672 (1982).
3. M. S. Kushwaha, "Plasmons and magnetoplasmons in semiconductor heterostructures," Surface Science Reports **41**, 1–416 (2001).
4. E. Yablonovitch and E. Kane, "Reduction of lasing threshold current density by the lowering of valence band effective mass," Journal of Lightwave Technology **4**, 504–506 (1986).
5. L. D. Nguyen, L. E. Larson, and U. K. Mishra, "Ultra-high speed modulation-doped field-effect transistors: a tutorial review," Proceedings of the IEEE **80**, 494–518 (1992).
6. K. S. Novoselov, A. K. Geim, S. V. Morozov, D. Jiang, Y. Zhang, S. V. Dubonos, I. V. Grigorieva, and A. A. Firsov, "Electric Field Effect in Atomically Thin Carbon Films," Science **306**, 666–669 (2004).
7. K. S. Novoselov, D. Jiang, F. Schedin, T. J. Booth, V. V. Khotkevich, S. V. Morozov, and A. K. Geim, "Two-dimensional atomic crystals," PNAS **102**, 10451–10453 (2005).
8. K. S. Novoselov, A. K. Geim, S. V. Morozov, D. Jiang, M. I. Katsnelson, I. V. Grigorieva, S. V. Dubonos, and A. A. Firsov, "Two-dimensional gas of massless Dirac fermions in graphene," Nature **438**, 197 (2005).
9. C. R. Dean, A. F. Young, I. Meric, C. Lee, L. Wang, S. Sorgenfrei, K. Watanabe, T. Taniguchi, P. Kim, K. L. Shepard, and J. Hone, "Boron nitride substrates for high-quality graphene electronics," Nat Nano **5**, 722–726 (2010).
10. K. I. Bolotin, K. J. Sikes, Z. Jiang, M. Klima, G. Fudenberg, J. Hone, P. Kim, and H. L. Stormer, "Ultrahigh electron mobility in suspended graphene," Solid State Communications **146**, 351–355 (2008).
11. L. Wang, I. Meric, P. Y. Huang, Q. Gao, Y. Gao, H. Tran, T. Taniguchi, K. Watanabe, L. M. Campos, D. A. Muller, J. Guo, P. Kim, J. Hone, K. L. Shepard, and C. R. Dean, "One-Dimensional Electrical Contact to a Two-Dimensional Material," Science **342**, 614–617 (2013).
12. L. Banszerus, M. Schmitz, S. Engels, J. Dauber, M. Oellers, F. Haupt, K. Watanabe, T. Taniguchi, B. Beschoten, and C. Stampfer, "Ultrahigh-mobility graphene devices from chemical vapor deposition on reusable copper," Science Advances **1**, e1500222 (2015).
13. C. Lee, X. Wei, J. W. Kysar, and J. Hone, "Measurement of the Elastic Properties and Intrinsic Strength of Monolayer Graphene," Science **321**, 385–388 (2008).
14. J. S. Bunch, A. M. van der Zande, S. S. Verbridge, I. W. Frank, D. M. Tanenbaum, J. M. Parpia, H. G. Craighead, and P. L. McEuen, "Electromechanical Resonators from Graphene Sheets," Science **315**, 490–493 (2007).
15. X. Wang, L. Zhi, and K. Müllen, "Transparent, Conductive Graphene Electrodes for Dye-Sensitized Solar Cells," Nano Lett. **8**, 323–327 (2008).
16. X. Li, Y. Zhu, W. Cai, M. Borysiak, B. Han, D. Chen, R. D. Piner, L. Colombo, and R. S. Ruoff, "Transfer of Large-Area Graphene Films for High-Performance Transparent Conductive Electrodes," Nano Lett. **9**, 4359–4363 (2009).
17. K. S. Kim, Y. Zhao, H. Jang, S. Y. Lee, J. M. Kim, K. S. Kim, J.-H. Ahn, P. Kim, J.-Y. Choi, and B. H. Hong, "Large-scale pattern growth of graphene films for stretchable transparent electrodes," Nature **457**, 706–710 (2009).

18. S. Bae, H. Kim, Y. Lee, X. Xu, J.-S. Park, Y. Zheng, J. Balakrishnan, T. Lei, H. Ri Kim, Y. I. Song, Y.-J. Kim, K. S. Kim, B. Özyilmaz, J.-H. Ahn, B. H. Hong, and S. Iijima, "Roll-to-roll production of 30-inch graphene films for transparent electrodes," Nat Nano **5**, 574–578 (2010).
19. Y.-M. Lin, A. Valdes-Garcia, S.-J. Han, D. B. Farmer, I. Meric, Y. Sun, Y. Wu, C. Dimitrakopoulos, A. Grill, P. Avouris, and K. A. Jenkins, "Wafer-Scale Graphene Integrated Circuit," Science **332**, 1294–1297 (2011).
20. S.-J. Han, K. A. Jenkins, A. Valdes Garcia, A. D. Franklin, A. A. Bol, and W. Haensch, "High-Frequency Graphene Voltage Amplifier," Nano Lett. **11**, 3690–3693 (2011).
21. S.-J. Han, A. V. Garcia, S. Oida, K. A. Jenkins, and W. Haensch, "Graphene radio frequency receiver integrated circuit," Nature Communications **5**, 3086 (2014).
22. M. Liu, X. Yin, E. Ulin-Avila, B. Geng, T. Zentgraf, L. Ju, F. Wang, and X. Zhang, "A graphene-based broadband optical modulator," Nature **474**, 64–67 (2011).
23. M. Liu, X. Yin, and X. Zhang, "Double-Layer Graphene Optical Modulator," Nano Lett. **12**, 1482–1485 (2012).
24. Y. T. Hu, M. Pantouvaki, S. Brems, I. Asselberghs, C. Huyghebaert, M. Geisler, C. Alessandri, R. Baets, P. Absil, D. V. Thourhout, and J. V. Campenhout, "Broadband 10Gb/s graphene electro-absorption modulator on silicon for chip-level optical interconnects," in *Electron Devices Meeting (IEDM), 2014 IEEE International* (2014), pp. 5.6.1-5.6.4.
25. C. T. Phare, Y.-H. Daniel Lee, J. Cardenas, and M. Lipson, "Graphene electro-optic modulator with 30 GHz bandwidth," Nat Photon **9**, 511–514 (2015).
26. F. Xia, T. Mueller, Y. Lin, A. Valdes-Garcia, and P. Avouris, "Ultrafast graphene photodetector," Nat Nano **4**, 839–843 (2009).
27. A. Pospischil, M. Humer, M. M. Furchi, D. Bachmann, R. Guider, T. Fromherz, and T. Mueller, "CMOS-compatible graphene photodetector covering all optical communication bands," Nature Photonics **7**, nphoton.2013.240 (2013).
28. X. Gan, R.-J. Shiue, Y. Gao, I. Meric, T. F. Heinz, K. Shepard, J. Hone, S. Assefa, and D. Englund, "Chip-integrated ultrafast graphene photodetector with high responsivity," Nature Photonics **7**, 883–887 (2013).
29. X. Wang, Z. Cheng, K. Xu, H. K. Tsang, and J.-B. Xu, "High-responsivity graphene/silicon-heterostructure waveguide photodetectors," Nature Photonics **7**, 888–891 (2013).
30. F. Schedin, A. K. Geim, S. V. Morozov, E. W. Hill, P. Blake, M. I. Katsnelson, and K. S. Novoselov, "Detection of individual gas molecules adsorbed on graphene," Nature Materials **6**, 652–655 (2007).
31. J.-H. Lee, E. K. Lee, W.-J. Joo, Y. Jang, B.-S. Kim, J. Y. Lim, S.-H. Choi, S. J. Ahn, J. R. Ahn, M.-H. Park, C.-W. Yang, B. L. Choi, S.-W. Hwang, and D. Whang, "Wafer-Scale Growth of Single-Crystal Monolayer Graphene on Reusable Hydrogen-Terminated Germanium," Science **344**, 286–289 (2014).
32. B. Radisavljevic, A. Radenovic, J. Brivio, V. Giacometti, and A. Kis, "Single-layer MoS_2 transistors," Nature Nanotechnology **6**, 147–150 (2011).
33. Q. H. Wang, K. Kalantar-Zadeh, A. Kis, J. N. Coleman, and M. S. Strano, "Electronics and optoelectronics of two-dimensional transition metal dichalcogenides," Nature Nanotechnology **7**, 699–712 (2012).
34. L. Li, Y. Yu, G. J. Ye, Q. Ge, X. Ou, H. Wu, D. Feng, X. H. Chen, and Y. Zhang, "Black phosphorus field-effect transistors," Nature Nanotechnology **9**, 372–377 (2014).

35. N. Youngblood, C. Chen, S. J. Koester, and M. Li, "Waveguide-integrated black phosphorus photodetector with high responsivity and low dark current," Nat Photon **9**, 247–252 (2015).
36. K. F. Mak, C. Lee, J. Hone, J. Shan, and T. F. Heinz, "Atomically Thin ${\mathrm{MoS}}_{2}$: A New Direct-Gap Semiconductor," Phys. Rev. Lett. **105**, 136805 (2010).
37. V. Tran, R. Soklaski, Y. Liang, and L. Yang, "Layer-controlled band gap and anisotropic excitons in few-layer black phosphorus," Phys. Rev. B **89**, 235319 (2014).
38. C. Gong, L. Li, Z. Li, H. Ji, A. Stern, Y. Xia, T. Cao, W. Bao, C. Wang, Y. Wang, Z. Q. Qiu, R. J. Cava, S. G. Louie, J. Xia, and X. Zhang, "Discovery of intrinsic ferromagnetism in two-dimensional van der Waals crystals," Nature **546**, 265–269 (2017).
39. B. Huang, G. Clark, E. Navarro-Moratalla, D. R. Klein, R. Cheng, K. L. Seyler, D. Zhong, E. Schmidgall, M. A. McGuire, D. H. Cobden, W. Yao, D. Xiao, P. Jarillo-Herrero, and X. Xu, "Layer-dependent ferromagnetism in a van der Waals crystal down to the monolayer limit," Nature **546**, 270–273 (2017).
40. C. Tan, J. Lee, S.-G. Jung, T. Park, S. Albarakati, J. Partridge, M. R. Field, D. G. McCulloch, L. Wang, and C. Lee, "Hard magnetic properties in nanoflake van der Waals Fe 3 GeTe 2," Nature Communications **9**, 1554 (2018).
41. Z. Fei, B. Huang, P. Malinowski, W. Wang, T. Song, J. Sanchez, W. Yao, D. Xiao, X. Zhu, A. F. May, W. Wu, D. H. Cobden, J.-H. Chu, and X. Xu, "Two-dimensional itinerant ferromagnetism in atomically thin Fe 3 GeTe 2," Nature Materials **17**, 778 (2018).
42. Y. Deng, Y. Yu, Y. Song, J. Zhang, N. Z. Wang, Z. Sun, Y. Yi, Y. Z. Wu, S. Wu, J. Zhu, J. Wang, X. H. Chen, and Y. Zhang, "Gate-tunable room-temperature ferromagnetism in two-dimensional Fe 3 GeTe 2," Nature **563**, 94 (2018).
43. N. W. Ashcroft and N. D. Mermin, *Solid State Physics.* (New York, Holt, Rinehart and Winston [c1976], 1976).
44. A. C. Ferrari and J. Robertson, "Raman spectroscopy of amorphous, nanostructured, diamond–like carbon, and nanodiamond," Philosophical Transactions of the Royal Society of London A: Mathematical, Physical and Engineering Sciences **362**, 2477–2512 (2004).
45. A. C. Ferrari, J. C. Meyer, V. Scardaci, C. Casiraghi, M. Lazzeri, F. Mauri, S. Piscanec, D. Jiang, K. S. Novoselov, S. Roth, and A. K. Geim, "Raman Spectrum of Graphene and Graphene Layers," Phys. Rev. Lett. **97**, 187401 (2006).
46. A. C. Ferrari, "Raman spectroscopy of graphene and graphite: Disorder, electron–phonon coupling, doping and nonadiabatic effects," Solid State Communications **143**, 47–57 (2007).
47. A. C. Ferrari and D. M. Basko, "Raman spectroscopy as a versatile tool for studying the properties of graphene," Nat Nano **8**, 235–246 (2013).
48. H. Suderow, V. G. Tissen, J. P. Brison, J. L. Martínez, and S. Vieira, "Pressure Induced Effects on the Fermi Surface of Superconducting 2 H − NbSe 2," Phys. Rev. Lett. **95**, 117006 (2005).
49. X. Xi, L. Zhao, Z. Wang, H. Berger, L. Forró, J. Shan, and K. F. Mak, "Strongly enhanced charge-density-wave order in monolayer NbSe2," Nature Nanotech **10**, 765–769 (2015).
50. J. T. Ye, Y. J. Zhang, R. Akashi, M. S. Bahramy, R. Arita, and Y. Iwasa, "Superconducting Dome in a Gate-Tuned Band Insulator," Science **338**, 1193–1196 (2012).
51. Y. Wang, J. Xiao, H. Zhu, Y. Li, Y. Alsaid, K. Y. Fong, Y. Zhou, S. Wang, W. Shi, Y. Wang, A. Zettl, E. J. Reed, and X. Zhang, "Structural phase transition in monolayer MoTe2 driven by electrostatic doping," Nature (2017).

52. J. T. Ye, S. Inoue, K. Kobayashi, Y. Kasahara, H. T. Yuan, H. Shimotani, and Y. Iwasa, "Liquid-gated interface superconductivity on an atomically flat film," Nature Mater **9**, 125–128 (2010).
53. H. Lee, K. Paeng, and I. S. Kim, "A review of doping modulation in graphene," Synthetic Metals **244**, 36–47 (2018).
54. C. R. Ryder, J. D. Wood, S. A. Wells, and M. C. Hersam, "Chemically Tailoring Semiconducting Two-Dimensional Transition Metal Dichalcogenides and Black Phosphorus," ACS Nano **10**, 3900–3917 (2016).
55. J. J. Sakurai, *Modern Quantum Mechanics*, Revised edition (Addison-Wesley Publishing, Co, 1994).
56. D. Jin, L. Lu, Z. Wang, C. Fang, J. D. Joannopoulos, M. Soljačić, L. Fu, and N. X. Fang, "Topological magnetoplasmon," Nature Communications **7**, 13486 (2016).
57. R. H. J. Vervuurt, W. M. M. (Erwin) Kessels, and A. A. Bol, "Atomic Layer Deposition for Graphene Device Integration," Advanced Materials Interfaces **4**, 1700232 (2017).
58. T. Wu, X. Zhang, Q. Yuan, J. Xue, G. Lu, Z. Liu, H. Wang, H. Wang, F. Ding, Q. Yu, X. Xie, and M. Jiang, "Fast growth of inch-sized single-crystalline graphene from a controlled single nucleus on Cu-Ni alloys," Nat Mater **15**, 43–47 (2016).
59. R. Soref and B. Bennett, "Electrooptical effects in silicon," IEEE J. Quantum Electron. **23**, 123–129 (1987).
60. Q. Xu, B. Schmidt, S. Pradhan, and M. Lipson, "Micrometre-scale silicon electro-optic modulator," Nature **435**, 325–327 (2005).
61. G. T. Reed, G. Mashanovich, F. Y. Gardes, and D. J. Thomson, "Silicon optical modulators," Nat Photon **4**, 518–526 (2010).
62. G. T. Reed, G. Z. Mashanovich, F. Y. Gardes, M. Nedeljkovic, Y. Hu, D. J. Thomson, K. Li, P. R. Wilson, S.-W. Chen, and S. S. Hsu, "Recent breakthroughs in carrier depletion based silicon optical modulators," Nanophotonics **3**, 229–245 (2013).
63. Y. Tang, J. D. Peters, and J. E. Bowers, "Over 67 GHz bandwidth hybrid silicon electroabsorption modulator with asymmetric segmented electrode for 13 μm transmission," Optics Express **20**, 11529 (2012).
64. D. Feng, S. Liao, H. Liang, J. Fong, B. Bijlani, R. Shafiiha, B. J. Luff, Y. Luo, J. Cunningham, A. V. Krishnamoorthy, and M. Asghari, "High speed GeSi electro-absorption modulator at 1550 nm wavelength on SOI waveguide," Optics Express **20**, 22224 (2012).
65. S. Gupta, S. A. Srinivasan, M. Pantouvaki, H. Chen, P. Verheyen, G. Lepage, D. V. Thourhout, G. Roelkens, K. Saraswat, P. Absil, and J. V. Campenhout, "50GHz Ge waveguide electro-absorption modulator integrated in a 220nm SOI photonics platform," in *2015 Optical Fiber Communications Conference and Exhibition (OFC)* (2015), pp. 1–3.
66. P. R. Wallace, "The Band Theory of Graphite," Phys. Rev. **71**, 622–634 (1947).
67. A. H. Castro Neto, F. Guinea, N. M. R. Peres, K. S. Novoselov, and A. K. Geim, "The electronic properties of graphene," Rev. Mod. Phys. **81**, 109–162 (2009).
68. F. Wang, Y. Zhang, C. Tian, C. Girit, A. Zettl, M. Crommie, and Y. R. Shen, "Gate-Variable Optical Transitions in Graphene," Science **320**, 206–209 (2008).
69. J. M. Dawlaty, S. Shivaraman, J. Strait, P. George, M. Chandrashekhar, F. Rana, M. G. Spencer, D. Veksler, and Y. Chen, "Measurement of the optical absorption spectra of epitaxial graphene from terahertz to visible," Applied Physics Letters **93**, 131905 (2008).

70. J. Kim, H. Son, D. J. Cho, B. Geng, W. Regan, S. Shi, K. Kim, A. Zettl, Y.-R. Shen, and F. Wang, "Electrical Control of Optical Plasmon Resonance with Graphene," Nano Lett. **12**, 5598–5602 (2012).
71. J. Horng, C.-F. Chen, B. Geng, C. Girit, Y. Zhang, Z. Hao, H. A. Bechtel, M. Martin, A. Zettl, M. F. Crommie, Y. R. Shen, and F. Wang, "Drude conductivity of Dirac fermions in graphene," Phys. Rev. B **83**, 165113 (2011).
72. W. Gao, J. Shu, C. Qiu, and Q. Xu, "Excitation of Plasmonic Waves in Graphene by Guided-Mode Resonances," ACS Nano **6**, 7806–7813 (2012).
73. L. A. Falkovsky, "Optical properties of graphene," Journal of Physics: Conference Series **129**, 012004 (2008).
74. G. W. Hanson, "Dyadic Green's functions and guided surface waves for a surface conductivity model of graphene," Journal of Applied Physics **103**, 064302 (2008).
75. T. Stauber, N. M. R. Peres, and A. K. Geim, "Optical conductivity of graphene in the visible region of the spectrum," Phys. Rev. B **78**, 085432 (2008).
76. H. Dalir, Y. Xia, Y. Wang, and X. Zhang, "Athermal Broadband Graphene Optical Modulator with 35 GHz Speed," ACS Photonics **3**, 1564–1568 (2016).
77. A. Harke, M. Krause, and J. Mueller, "Low-loss singlemode amorphous silicon waveguides," Electronics Letters **41**, 1377–1379 (2005).
78. S. Zhu, G. Q. Lo, and D. L. Kwong, "Low-loss amorphous silicon wire waveguide for integrated photonics: effect of fabrication process and the thermal stability," Opt. Express, OE **18**, 25283–25291 (2010).
79. J. W. Suk, A. Kitt, C. W. Magnuson, Y. Hao, S. Ahmed, J. An, A. K. Swan, B. B. Goldberg, and R. S. Ruoff, "Transfer of CVD-Grown Monolayer Graphene onto Arbitrary Substrates," ACS Nano **5**, 6916–6924 (2011).
80. H. Alles, J. Aarik, J. Kozlova, A. Niilisk, R. Rammula, and V. Sammelselg, "Atomic Layer Deposition of High-k Oxides on Graphene," in *Graphene - Synthesis, Characterization, Properties and Applications*, J. Gong, ed. (InTech, 2011).
81. W. S. Leong, H. Gong, and J. T. L. Thong, "Low-Contact-Resistance Graphene Devices with Nickel-Etched-Graphene Contacts," ACS Nano **8**, 994–1001 (2014).
82. M. D. Groner, J. W. Elam, F. H. Fabreguette, and S. M. George, "Electrical characterization of thin Al2O3 films grown by atomic layer deposition on silicon and various metal substrates," Thin Solid Films **413**, 186–197 (2002).
83. J. T. Gaskins, P. E. Hopkins, D. R. Merrill, S. R. Bauers, E. Hadland, D. C. Johnson, D. Koh, J. H. Yum, S. Banerjee, B. J. Nordell, M. M. Paquette, A. N. Caruso, W. A. Lanford, P. Henry, L. Ross, H. Li, L. Li, M. French, A. M. Rudolph, and S. W. King, "Review—Investigation and Review of the Thermal, Mechanical, Electrical, Optical, and Structural Properties of Atomic Layer Deposited High- *k* Dielectrics: Beryllium Oxide, Aluminum Oxide, Hafnium Oxide, and Aluminum Nitride," ECS J. Solid State Sci. Technol. **6**, N189–N208 (2017).
84. M. Nakahara and T. Ohmi, *Quantum Computing: From Linear Algebra to Physical Realizations* (CRC press, 2008).
85. A. Ekert and R. Jozsa, "Quantum computation and Shor's factoring algorithm," Rev. Mod. Phys. **68**, 733–753 (1996).
86. N. Gisin and R. Thew, "Quantum communication," Nature Photonics **1**, 165–171 (2007).
87. J. L. O'Brien, A. Furusawa, and J. Vučković, "Photonic quantum technologies," Nature Photonics **3**, 687–695 (2009).

88. Charles Santori, David Fattal, and Yoshihisa Yamamoto, *Single-Photon Devices and Applications* (Wiley-VCH, 2010).
89. I. Aharonovich, D. Englund, and M. Toth, "Solid-state single-photon emitters," Nat Photon **10**, 631–641 (2016).
90. J. P. Reithmaier, G. Sęk, A. Löffler, C. Hofmann, S. Kuhn, S. Reitzenstein, L. V. Keldysh, V. D. Kulakovskii, T. L. Reinecke, and A. Forchel, "Strong coupling in a single quantum dot–semiconductor microcavity system," Nature **432**, 197 (2004).
91. E. Flagg, A. Muller, S. Polyakov, A. Ling, A. Migdall, and G. Solomon, "Interference of Single Photons from Two Separate Semiconductor Quantum Dots," Physical Review Letters **104**, (2010).
92. N. Q. Dots, "Quantum-Confined Stark Effect in Single CdSe," Science **278**, 2114–2114 (1997).
93. C. Santori, D. Fattal, J. Vučković, G. S. Solomon, and Y. Yamamoto, "Indistinguishable photons from a single-photon device," Nature **419**, 594 (2002).
94. C. Chakraborty, K. M. Goodfellow, S. Dhara, A. Yoshimura, V. Meunier, and A. N. Vamivakas, "Quantum-Confined Stark Effect of Individual Defects in a van der Waals Heterostructure," Nano Lett. **17**, 2253–2258 (2017).
95. Ph. Tamarat, T. Gaebel, J. R. Rabeau, M. Khan, A. D. Greentree, H. Wilson, L. C. L. Hollenberg, S. Prawer, P. Hemmer, F. Jelezko, and J. Wrachtrup, "Stark Shift Control of Single Optical Centers in Diamond," Phys. Rev. Lett. **97**, 083002 (2006).
96. L. C. Bassett, F. J. Heremans, C. G. Yale, B. B. Buckley, and D. D. Awschalom, "Electrical Tuning of Single Nitrogen-Vacancy Center Optical Transitions Enhanced by Photoinduced Fields," Phys. Rev. Lett. **107**, 266403 (2011).
97. H. Bernien, L. Childress, L. Robledo, M. Markham, D. Twitchen, and R. Hanson, "Two-Photon Quantum Interference from Separate Nitrogen Vacancy Centers in Diamond," Physical Review Letters **108**, (2012).
98. R. Lettow, Y. L. A. Rezus, A. Renn, G. Zumofen, E. Ikonen, S. Götzinger, and V. Sandoghdar, "Quantum Interference of Tunably Indistinguishable Photons from Remote Organic Molecules," Phys. Rev. Lett. **104**, 123605 (2010).
99. A. Sipahigil, M. L. Goldman, E. Togan, Y. Chu, M. Markham, D. J. Twitchen, A. S. Zibrov, A. Kubanek, and M. D. Lukin, "Quantum Interference of Single Photons from Remote Nitrogen-Vacancy Centers in Diamond," Physical Review Letters **108**, (2012).
100. T. T. Tran, K. Bray, M. J. Ford, M. Toth, and I. Aharonovich, "Quantum emission from hexagonal boron nitride monolayers," Nat Nano **11**, 37–41 (2016).
101. T. T. Tran, C. Elbadawi, D. Totonjian, C. J. Lobo, G. Grosso, H. Moon, D. R. Englund, M. J. Ford, I. Aharonovich, and M. Toth, "Robust Multicolor Single Photon Emission from Point Defects in Hexagonal Boron Nitride," ACS Nano **10**, 7331–7338 (2016).
102. Z. Shotan, H. Jayakumar, C. R. Considine, M. Mackoit, H. Fedder, J. Wrachtrup, A. Alkauskas, M. W. Doherty, V. M. Menon, and C. A. Meriles, "Photoinduced Modification of Single-Photon Emitters in Hexagonal Boron Nitride," ACS Photonics **3**, 2490–2496 (2016).
103. G. Grosso, H. Moon, B. Lienhard, S. Ali, D. K. Efetov, M. M. Furchi, P. Jarillo-Herrero, M. J. Ford, I. Aharonovich, and D. Englund, "Tunable and high-purity room temperature single-photon emission from atomic defects in hexagonal boron nitride," Nature Communications **8**, 705 (2017).

104. T. T. Tran, C. Zachreson, A. M. Berhane, K. Bray, R. G. Sandstrom, L. H. Li, T. Taniguchi, K. Watanabe, I. Aharonovich, and M. Toth, "Quantum Emission from Defects in Single-Crystalline Hexagonal Boron Nitride," Phys. Rev. Applied **5**, 034005 (2016).
105. S. Choi, T. T. Tran, C. Elbadawi, C. Lobo, X. Wang, S. Juodkazis, G. Seniutinas, M. Toth, and I. Aharonovich, "Engineering and Localization of Quantum Emitters in Large Hexagonal Boron Nitride Layers," ACS Appl. Mater. Interfaces **8**, 29642–29648 (2016).
106. A. L. Exarhos, D. A. Hopper, R. R. Grote, A. Alkauskas, and L. C. Bassett, "Optical Signatures of Quantum Emitters in Suspended Hexagonal Boron Nitride," ACS Nano **11**, 3328–3336 (2017).
107. N. Chejanovsky, M. Rezai, F. Paolucci, Y. Kim, T. Rendler, W. Rouabeh, F. Fávaro de Oliveira, P. Herlinger, A. Denisenko, S. Yang, I. Gerhardt, A. Finkler, J. H. Smet, and J. Wrachtrup, "Structural Attributes and Photodynamics of Visible Spectrum Quantum Emitters in Hexagonal Boron Nitride," Nano Lett. **16**, 7037–7045 (2016).
108. Y. Xia, Q. Li, J. Kim, W. Bao, C. Gong, S. Yang, Y. Wang, and X. Zhang, "Room-temperature giant Stark effect of single photon emitter in van der Waals material," arXiv:1902.07340 [cond-mat, physics:quant-ph] (2019).
109. R. Geick, C. H. Perry, and G. Rupprecht, "Normal Modes in Hexagonal Boron Nitride," Phys. Rev. **146**, 543–547 (1966).
110. T. Müller, I. Aharonovich, L. Lombez, Y. Alaverdyan, A. N. Vamivakas, S. Castelletto, F. Jelezko, J. Wrachtrup, S Prawer, and M. Atatüre, "Wide-range electrical tunability of single-photon emission from chromium-based colour centres in diamond," New J. Phys. **13**, 075001 (2011).
111. B. A. Bernevig, *Topological Insulators and Topological Superconductors* (Princeton University Press, 2013).
112. X.-L. Qi and S.-C. Zhang, "Topological insulators and superconductors," Rev. Mod. Phys. **83**, 1057–1110 (2011).
113. L. Lu, J. D. Joannopoulos, and M. Soljačić, "Topological photonics," Nature Photonics **8**, 821–829 (2014).
114. S. Raghu and F. D. M. Haldane, "Analogs of quantum-Hall-effect edge states in photonic crystals," Phys. Rev. A **78**, 033834 (2008).
115. D. Jin, T. Christensen, M. Soljačić, N. X. Fang, L. Lu, and X. Zhang, "Infrared Topological Plasmons in Graphene," Phys. Rev. Lett. **118**, 245301 (2017).
116. S. A. Hassani Gangaraj and F. Monticone, "Topological Waveguiding near an Exceptional Point: Defect-Immune, Slow-Light, and Loss-Immune Propagation," Phys. Rev. Lett. **121**, 093901 (2018).
117. L. Ju, Z. Shi, N. Nair, Y. Lv, C. Jin, J. Velasco Jr, C. Ojeda-Aristizabal, H. A. Bechtel, M. C. Martin, A. Zettl, J. Analytis, and F. Wang, "Topological valley transport at bilayer graphene domain walls," Nature **520**, 650–655 (2015).
118. F. Gao, H. Xue, Z. Yang, K. Lai, Y. Yu, X. Lin, Y. Chong, G. Shvets, and B. Zhang, "Topologically protected refraction of robust kink states in valley photonic crystals," Nature Physics **14**, 140–144 (2018).
119. K. Yasuda, M. Mogi, R. Yoshimi, A. Tsukazaki, K. S. Takahashi, M. Kawasaki, F. Kagawa, and Y. Tokura, "Quantized chiral edge conduction on domain walls of a magnetic topological insulator," Science **358**, 1311–1314 (2017).
120. Z. Wang, Y. Chong, J. D. Joannopoulos, and M. Soljačić, "Observation of unidirectional backscattering-immune topological electromagnetic states," Nature **461**, 772–775 (2009).

121. K. Fang, Z. Yu, and S. Fan, "Realizing effective magnetic field for photons by controlling the phase of dynamic modulation," Nature Photonics **6**, 782–787 (2012).
122. R. Shindou, R. Matsumoto, S. Murakami, and J. Ohe, "Topological chiral magnonic edge mode in a magnonic crystal," Phys. Rev. B **87**, 174427 (2013).
123. J. Yuen-Zhou, \relax S.K Saikin, \relax N.Y Yao, and A. Aspuru-Guzik, "Topologically protected excitons in porphyrin thin films," Nat. Mater. **13**, 1026–1032 (2014).
124. T. Karzig, \relax C.-E Bardyn, \relax N.H Lindner, and G. Refael, "Topological Polaritons," Phys. Rev. X **5**, 031001 (2015).
125. A. C. Mahoney, J. I. Colless, S. J. Pauka, J. M. Hornibrook, J. D. Watson, G. C. Gardner, M. J. Manfra, A. C. Doherty, and D. J. Reilly, "On-Chip Microwave Quantum Hall Circulator," Phys. Rev. X **7**, 011007 (2017).
126. B. Bahari, A. Ndao, F. Vallini, A. E. Amili, Y. Fainman, and B. Kanté, "Nonreciprocal lasing in topological cavities of arbitrary geometries," Science **358**, 636–640 (2017).
127. D. B. Mast, A. J. Dahm, and A. L. Fetter, "Observation of Bulk and Edge Magnetoplasmons in a Two-Dimensional Electron Fluid," Phys. Rev. Lett. **54**, 1706 (1985).
128. A. Ohtomo and H. Hwang, "A high-mobility electron gas at the LaAlO3/SrTiO3 heterointerface," Nature **427**, 423–426 (2004).
129. K. Bolotin, K. Sikes, J. Hone, H. Stormer, and P. Kim, "Temperature-dependent transport in suspended graphene," Phys. Rev. Lett. **101**, 096802 (2008).
130. P. Delplace, J. B. Marston, and A. Venaille, "Topological origin of equatorial waves," Science **358**, 1075–1077 (2017).
131. A. L. Fetter, "Magnetoplasmons in a two-dimensional electron fluid: disk geometry," Phys. Rev. B **33**, 5221 (1986).
132. D. Jin, Y. Xia, T. Christensen, S. Wang, K. Y. Fong, M. Freeman, G. C. Gardner, S. Fallahi, Q. Hu, Y. Wang, L. Engel, M. J. Manfra, N. X. Fang, and X. Zhang, "Magnetically-defined topological edge plasmons in edgeless electron gas," arXiv:1803.02913 [cond-mat, physics:physics, physics:quant-ph] (2018).
133. R. C. Ashoori, H. L. Stormer, L. N. Pfeiffer, K. W. Baldwin, and K. West, "Edge magnetoplasmons in the time domain," Phys. Rev. B **45**, 3894–3897 (1992).
134. O. Balev and P. Vasilopoulos, "Edge magnetoplasmons for very low temperatures and sharp density profiles," Phys. Rev. B **56**, 13252 (1997).
135. N. Kumada, P. Roulleau, B. Roche, M. Hashisaka, H. Hibino, I. Petković, and D. C. Glattli, "Resonant Edge Magnetoplasmons and Their Decay in Graphene," Phys. Rev. Lett. **113**, 266601 (2014).
136. A. T. Hatke, Y. Liu, L. W. Engel, M. Shayegan, L. N. Pfeiffer, K. W. West, and K. W. Baldwin, "Microwave spectroscopy of the low-filling-factor bilayer electron solid in a wide quantum well," Nature Communications **6**, 7071 (2015).
137. J. Mi, H. Liu, J. Shi, L. N. Pfeiffer, K. W. West, K. W. Baldwin, and C. Zhang, "Low-Frequency Microwave Induced Quantum Oscillations in A Two-Dimensional Electron System," arXiv:1708.08498 [cond-mat] (2017).
138. Z.-J. Yang, T. J. Antosiewicz, R. Verre, F. J. García de Abajo, S. P. Apell, and M. Käll, "Ultimate Limit of Light Extinction by Nanophotonic Structures," Nano Lett. **15**, 7633–7638 (2015).
139. Z. Fei, G. O. Andreev, W. Bao, L. M. Zhang, A. S. McLeod, C. Wang, M. K. Stewart, Z. Zhao, G. Dominguez, M. Thiemens, M. M. Fogler, M. J. Tauber, A. H. Castro-Neto, C. N.

Lau, F. Keilmann, and D. N. Basov, "Infrared Nanoscopy of Dirac Plasmons at the Graphene–SiO2 Interface," Nano Lett. **11**, 4701–4705 (2011).
140. D. C. Ralph and M. D. Stiles, "Spin transfer torques," Journal of Magnetism and Magnetic Materials **320**, 1190–1216 (2008).
141. T. McGuire and R. Potter, "Anisotropic magnetoresistance in ferromagnetic 3d alloys," IEEE Transactions on Magnetics **11**, 1018–1038 (1975).
142. A. Schuhl, F. N. Van Dau, and J. R. Childress, "Low-field magnetic sensors based on the planar Hall effect," Appl. Phys. Lett. **66**, 2751–2753 (1995).
143. H. X. Tang, R. K. Kawakami, D. D. Awschalom, and M. L. Roukes, "Giant Planar Hall Effect in Epitaxial (Ga,Mn)As Devices," Physical Review Letters **90**, (2003).
144. A. A. Taskin, H. F. Legg, F. Yang, S. Sasaki, Y. Kanai, K. Matsumoto, A. Rosch, and Y. Ando, "Planar Hall effect from the surface of topological insulators," Nature Communications **8**, 1340 (2017).
145. P. N. Granell, G. Wang, G. S. C. Bermudez, T. Kosub, F. Golmar, L. Steren, J. Fassbender, and D. Makarov, "Highly compliant planar Hall effect sensor with sub 200 nT sensitivity," npj Flexible Electronics **3**, 3 (2019).
146. M. N. Baibich, J. M. Broto, A. Fert, F. N. Van Dau, F. Petroff, P. Etienne, G. Creuzet, A. Friederich, and J. Chazelas, "Giant Magnetoresistance of (001)Fe/(001)Cr Magnetic Superlattices," Phys. Rev. Lett. **61**, 2472–2475 (1988).
147. J. Q. Xiao, J. S. Jiang, and C. L. Chien, "Giant magnetoresistance in nonmultilayer magnetic systems," Phys. Rev. Lett. **68**, 3749–3752 (1992).
148. A. E. Berkowitz, J. R. Mitchell, M. J. Carey, A. P. Young, S. Zhang, F. E. Spada, F. T. Parker, A. Hutten, and G. Thomas, "Giant magnetoresistance in heterogeneous Cu-Co alloys," Phys. Rev. Lett. **68**, 3745–3748 (1992).
149. A. Fert, "Nobel Lecture: Origin, development, and future of spintronics," Rev. Mod. Phys. **80**, 1517–1530 (2008).
150. I. Žutić, J. Fabian, and S. Das Sarma, "Spintronics: Fundamentals and applications," Rev. Mod. Phys. **76**, 323–410 (2004).
151. D. A. Allwood, G. Xiong, M. D. Cooke, C. C. Faulkner, D. Atkinson, N. Vernier, and R. P. Cowburn, "Submicrometer Ferromagnetic NOT Gate and Shift Register," Science **296**, 2003–2006 (2002).
152. S. S. P. Parkin, M. Hayashi, and L. Thomas, "Magnetic Domain-Wall Racetrack Memory," Science **320**, 190–194 (2008).
153. D. A. Allwood, G. Xiong, C. C. Faulkner, D. Atkinson, D. Petit, and R. P. Cowburn, "Magnetic Domain-Wall Logic," Science **309**, 1688–1692 (2005).
154. C.-Z. Chang, J. Zhang, X. Feng, J. Shen, Z. Zhang, M. Guo, K. Li, Y. Ou, P. Wei, L.-L. Wang, Z.-Q. Ji, Y. Feng, S. Ji, X. Chen, J. Jia, X. Dai, Z. Fang, S.-C. Zhang, K. He, Y. Wang, L. Lu, X.-C. Ma, and Q.-K. Xue, "Experimental Observation of the Quantum Anomalous Hall Effect in a Magnetic Topological Insulator," Science **340**, 167–170 (2013).
155. K. L. Wang, M. Lang, and X. Kou, "Spintronics of Topological Insulators," in *Handbook of Spintronics*, Y. Xu, D. D. Awschalom, and J. Nitta, eds. (Springer Netherlands, 2016), pp. 431–462.
156. Z. Wang, D. Sapkota, T. Taniguchi, K. Watanabe, D. Mandrus, and A. F. Morpurgo, "Tunneling Spin Valves Based on Fe3GeTe2/hBN/Fe3GeTe2 van der Waals Heterostructures," Nano Lett. (2018).

157. A. K. Geim and I. V. Grigorieva, "Van der Waals heterostructures," Nature **499**, 419–425 (2013).
158. N. Nagaosa, J. Sinova, S. Onoda, A. H. MacDonald, and N. P. Ong, "Anomalous Hall effect," Rev. Mod. Phys. **82**, 1539–1592 (2010).
159. R. T. Bate, J. C. Bell, and A. C. Beer, "Influence of Magnetoconductivity Discontinuities on Galvanomagnetic Effects in Indium Antimonide," Journal of Applied Physics **32**, 806–814 (1961).
160. M. Yamanouchi, D. Chiba, F. Matsukura, and H. Ohno, "Current-induced domain-wall switching in a ferromagnetic semiconductor structure," Nature **428**, 539–542 (2004).
161. X. M. Cheng, S. Urazhdin, O. Tchernyshyov, C. L. Chien, V. I. Nikitenko, A. J. Shapiro, and R. D. Shull, "Antisymmetric Magnetoresistance in Magnetic Multilayers with Perpendicular Anisotropy," Physical Review Letters **94**, (2005).
162. Z. Fei, T. Palomaki, S. Wu, W. Zhao, X. Cai, B. Sun, P. Nguyen, J. Finney, X. Xu, and D. H. Cobden, "Edge conduction in monolayer WTe_2," Nature Physics **13**, 677–682 (2017).
163. P. J. Zomer, M. H. D. Guimarães, J. C. Brant, N. Tombros, and B. J. van Wees, "Fast pick up technique for high quality heterostructures of bilayer graphene and hexagonal boron nitride," Appl. Phys. Lett. **105**, 013101 (2014).
164. P. Gaunt, "Ferromagnetic domain wall pinning by a random array of inhomogeneities," Philosophical Magazine B **48**, 261–276 (1983).
165. A. Butera, J. L. Weston, and J. A. Barnard, "Temperature dependence of the coercivity of Fe films sputtered on nanochannel alumina," IEEE Transactions on Magnetics **34**, 1024–1026 (1998).
166. S. Gangopadhyay, G. C. Hadjipanayis, B. Dale, C. M. Sorensen, K. J. Klabunde, V. Papaefthymiou, and A. Kostikas, "Magnetic properties of ultrafine iron particles," Physical Review B **45**, 9778–9787 (1992).
167. J. C. T. Eijkel and A. van den Berg, "Nanofluidics: what is it and what can we expect from it?," Microfluid Nanofluid **1**, 249–267 (2005).
168. T. Jain, B. C. Rasera, R. J. S. Guerrero, M. S. H. Boutilier, S. C. O'Hern, J.-C. Idrobo, and R. Karnik, "Heterogeneous sub-continuum ionic transport in statistically isolated graphene nanopores," Nature Nanotechnology **10**, 1053–1057 (2015).
169. J. Feng, M. Graf, K. Liu, D. Ovchinnikov, D. Dumcenco, M. Heiranian, V. Nandigana, N. R. Aluru, A. Kis, and A. Radenovic, "Single-layer MoS2 nanopores as nanopower generators," Nature **advance online publication**, (2016).
170. C. Dekker, "Solid-state nanopores," Nature Nanotechnology **2**, 209–215 (2007).
171. F. Fornasiero, H. G. Park, J. K. Holt, M. Stadermann, C. P. Grigoropoulos, A. Noy, and O. Bakajin, "Ion exclusion by sub-2-nm carbon nanotube pores," PNAS **105**, 17250–17255 (2008).
172. A. Siria, P. Poncharal, A.-L. Biance, R. Fulcrand, X. Blase, S. T. Purcell, and L. Bocquet, "Giant osmotic energy conversion measured in a single transmembrane boron nitride nanotube," Nature **494**, 455–458 (2013).
173. E. Secchi, A. Niguès, L. Jubin, A. Siria, and L. Bocquet, "Scaling Behavior for Ionic Transport and its Fluctuations in Individual Carbon Nanotubes," Phys. Rev. Lett. **116**, 154501 (2016).
174. E. Secchi, S. Marbach, A. Niguès, D. Stein, A. Siria, and L. Bocquet, "Massive radius-dependent flow slippage in carbon nanotubes," Nature **537**, 210–213 (2016).

175. R. H. Tunuguntla, R. Y. Henley, Y.-C. Yao, T. A. Pham, M. Wanunu, and A. Noy, "Enhanced water permeability and tunable ion selectivity in subnanometer carbon nanotube porins," Science **357**, 792–796 (2017).
176. C. Miller, *Ionic Channels of Excitable Membranes.: By Bertil Hille. Sunderland, Massachusetts: Sinauer.(1991). 607 Pp. $46.95* (Cell Press, 1992).
177. L. Bocquet and E. Charlaix, "Nanofluidics, from bulk to interfaces," Chem. Soc. Rev. **39**, 1073–1095 (2010).
178. C. Duan, W. Wang, and Q. Xie, "Review article: Fabrication of nanofluidic devices," Biomicrofluidics **7**, 026501 (2013).
179. R. B. Schoch, J. Han, and P. Renaud, "Transport phenomena in nanofluidics," Rev. Mod. Phys. **80**, 839–883 (2008).
180. A. K. Geim and K. S. Novoselov, "The rise of graphene," Nat Mater **6**, 183–191 (2007).
181. K. S. Novoselov, Z. Jiang, Y. Zhang, S. V. Morozov, H. L. Stormer, U. Zeitler, J. C. Maan, G. S. Boebinger, P. Kim, and A. K. Geim, "Room-Temperature Quantum Hall Effect in Graphene," Science **315**, 1379–1379 (2007).
182. Y. Cao, V. Fatemi, S. Fang, K. Watanabe, T. Taniguchi, E. Kaxiras, and P. Jarillo-Herrero, "Unconventional superconductivity in magic-angle graphene superlattices," Nature **556**, 43–50 (2018).
183. Z. Ye, T. Cao, K. O'Brien, H. Zhu, X. Yin, Y. Wang, S. G. Louie, and X. Zhang, "Probing excitonic dark states in single-layer tungsten disulphide," Nature **513**, 214–218 (2014).
184. A. Schlaich, E. W. Knapp, and R. R. Netz, "Water Dielectric Effects in Planar Confinement," Phys. Rev. Lett. **117**, 048001 (2016).
185. L. Fumagalli, A. Esfandiar, R. Fabregas, S. Hu, P. Ares, A. Janardanan, Q. Yang, B. Radha, T. Taniguchi, K. Watanabe, G. Gomila, K. S. Novoselov, and A. K. Geim, "Anomalously low dielectric constant of confined water," Science **360**, 1339–1342 (2018).
186. G. Algara-Siller, O. Lehtinen, F. C. Wang, R. R. Nair, U. Kaiser, H. A. Wu, A. K. Geim, and I. V. Grigorieva, "Square ice in graphene nanocapillaries," Nature **519**, 443–445 (2015).
187. G. Tocci, L. Joly, and A. Michaelides, "Friction of Water on Graphene and Hexagonal Boron Nitride from Ab Initio Methods: Very Different Slippage Despite Very Similar Interface Structures," Nano Lett. **14**, 6872–6877 (2014).
188. T. Mouterde, A. Keerthi, A. R. Poggioli, S. A. Dar, A. Siria, A. K. Geim, L. Bocquet, and B. Radha, "Molecular streaming and its voltage control in ångström-scale channels," Nature **567**, 87–90 (2019).
189. L. Huang, Y. Li, Q. Zhou, W. Yuan, and G. Shi, "Graphene Oxide Membranes with Tunable Semipermeability in Organic Solvents," Advanced Materials **27**, 3797–3802 (2015).
190. J. Abraham, K. S. Vasu, C. D. Williams, K. Gopinadhan, Y. Su, C. T. Cherian, J. Dix, E. Prestat, S. J. Haigh, I. V. Grigorieva, P. Carbone, A. K. Geim, and R. R. Nair, "Tunable sieving of ions using graphene oxide membranes," Nature Nanotechnology **12**, 546–550 (2017).
191. C. Gómez-Navarro, R. T. Weitz, A. M. Bittner, M. Scolari, A. Mews, M. Burghard, and K. Kern, "Electronic Transport Properties of Individual Chemically Reduced Graphene Oxide Sheets," Nano Lett. **7**, 3499–3503 (2007).
192. R. W. Impey, P. A. Madden, and I. R. McDonald, "Hydration and mobility of ions in solution," J. Phys. Chem. **87**, 5071–5083 (1983).

193. K. Gopinadhan, S. Hu, A. Esfandiar, M. Lozada-Hidalgo, F. C. Wang, Q. Yang, A. V. Tyurnina, A. Keerthi, B. Radha, and A. K. Geim, "Complete steric exclusion of ions and proton transport through confined monolayer water," Science **363**, 145–148 (2019).
194. B. Dietrich, "Coordination chemistry of alkali and alkaline-earth cations with macrocyclic ligands," J. Chem. Educ. **62**, 954 (1985).
195. E. Gouaux and R. MacKinnon, "Principles of Selective Ion Transport in Channels and Pumps," Science **310**, 1461–1465 (2005).
196. D. A. Köpfer, C. Song, T. Gruene, G. M. Sheldrick, U. Zachariae, and B. L. de Groot, "Ion permeation in K+ channels occurs by direct Coulomb knock-on," Science **346**, 352–355 (2014).
197. J. Chen, B. Yao, C. Li, and G. Shi, "An improved Hummers method for eco-friendly synthesis of graphene oxide," Carbon **64**, 225–229 (2013).